AD-A087 671 NATIONAL BUREAU OF STANDARDS WASHINGTON D C ELECTRO--ETC F/G 9/5
JOSEPHSON A/D CONVERTER DEVELOPMENT.(U)
SEP 79 C A HAMILTON, R E HARRIS, R L KAUTZ N00014-79-F-0005
UNCLASSIFIED SR-724-15-80 NL

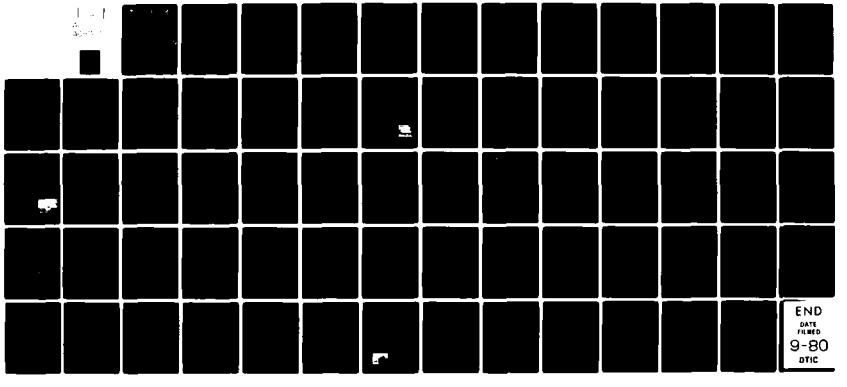

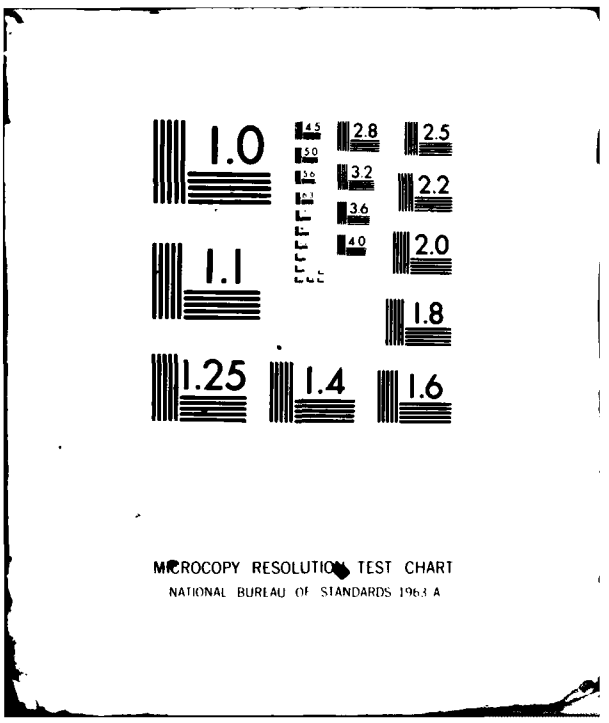
1.0
1.1
1.25
1.4
1.6
1.8
2.0
2.2
2.5
2.8
3.2
3.6
4.0
4.5
5.0
5.6
MICROCOPY RESOLUTION TEST CHART
NATIONAL BUREAU OF STANDARDS 1963 A

(6) JOSEPHSON A/D CONVERTER DEVELOPMENT.

(9) ANNUAL TECHNICAL REPORT. 1 May 78–30 Apr 79,

to

Office of Naval Research, Code 427
Arlington, VA 22217

May 1, 1978 to April 30, 1979
Contract Number N00014-79-F-0005
Contract Authority NR 383-040

(15)

by

(10) C. A. Hamilton, R. E. Harris, R. L. Kautz,
F. L. Lloyd and R. L. Peterson
(Report prepared by R. E. Harris)

Submitted by:

Electromagnetic Technology Division
Center for Electronics and Electrical Engineering
National Engineering Laboratory
National Bureau of Standards
Boulder, CO 80303

Cost Center No. 7240480

(14) ~~Report No.~~ SR-724-15-80

(11) 1 Sept 1979

Reviewed and Approved by:

(12) 66

R. Kamper

R. A. Kamper, Chief
Electromagnetic Technology Division

SECURITY CLASSIFICATION OF THIS PAGE (When Data Entered)

REPORT DOCUMENTATION PAGE	READ INSTRUCTIONS BEFORE COMPLETING FORM
1. REPORT NUMBER	2. GOVT ACCESSION NO. AD-A087671	3. RECIPIENT'S CATALOG NUMBER
4. TITLE (and Subtitle) JOSEPHSON A/D CONVERTER DEVELOPMENT	5. TYPE OF REPORT & PERIOD COVERED Annual Technical for Period May 1, 1979 to April 30, 1980
	6. PERFORMING ORG. REPORT NUMBER SR-724-8-18 15-80
7. AUTHOR(s) C. A. Hamilton, R. E. Harris, R. L. Kautz, F. L. Lloyd, and R. L. Peterson	8. CONTRACT OR GRANT NUMBER(s) N00014-79-F-0005
9. PERFORMING ORGANIZATION NAME AND ADDRESS Cryoelectronic Metrology Section Electromagnetic Technology Division National Bureau of Standards Boulder, CO 80303	10. PROGRAM ELEMENT, PROJECT, TASK AREA & WORK UNIT NUMBERS PE 62762N RF 62-582-001 NR 383-040
11. CONTROLLING OFFICE NAME AND ADDRESS Office of Naval Research, Code 427 Arlington, VA 22217	12. REPORT DATE Sept. 1, 1979
	13. NUMBER OF PAGES 71
14. MONITORING AGENCY NAME & ADDRESS(if different from Controlling Office) Same	15. SECURITY CLASS. (of this report) Unclassified
	15a. DECLASSIFICATION/DOWNGRADING SCHEDULE

16. DISTRIBUTION STATEMENT (of this Report)
Approved for public release; distribution unlimited.

17. DISTRIBUTION STATEMENT (of the abstract entered in Block 20, if different from Report)

18. SUPPLEMENTARY NOTES
ONR Scientific Officer
Telephone (202) 696-4218

19. KEY WORDS (Continue on reverse side if necessary and identify by block number)
A/D converter; high speed superconducting electronics; Josephson junctions

20. ABSTRACT (Continue on reverse side if necessary and identify by block number)
This report describes the second year of an effort to demonstrate an ultra-high-speed analog-to-digital converter using superconducting electronics. A converter was fabricated and tested, producing 200 to 700 megasamples per second. Experimental and theoretical support work is also presented.

DD FORM 1 JAN 73 1473 EDITION OF 1 NOV 65 IS OBSOLETE S/N 0102-014-6601

Unclassified
SECURITY CLASSIFICATION OF THIS PAGE (When Data Entered)

JOSEPHSON A/D CONVERTER DEVELOPMENT

ANNUAL TECHNICAL REPORT

September 1, 1979

Permission for Distribution Received April 4, 1980

JOSEPHSON A/D CONVERTER DEVELOPMENT

TABLE OF CONTENTS

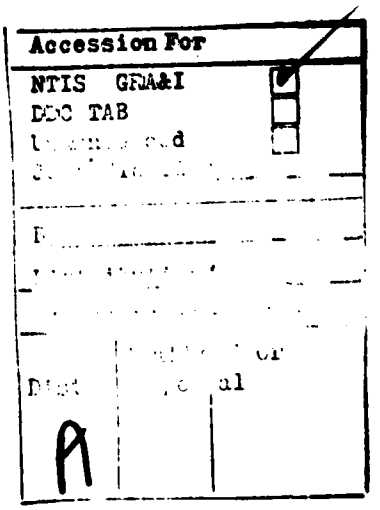

OFFICE OF NAVAL RESEARCH

A/D Converter

Second Annual Report

1.0 INTRODUCTION

This report describes the second year of work on contract number N00014-79-F-0005. The work has the following general goals:

> Demonstration of a superconducting 300 megasample per second A/D converter within the first three years.
>
> Demonstration of a superconducting A/D converter operating well into the gigasample per second region within five years.

During this second year the goal for the third year was essentially accomplished and described in a publication in Applied Physics Letters on an A/D converter operating between 200 and 700 megasamples per second. This remarkable success, in a totally new technology, was the result of advances in three areas:

> Early in the reporting period, the catalog of processes necessary for fabricating superconducting integrated circuits was completed, and the first circuits were successfully demonstrated. This work had been the primary subject of the first year's contract.
>
> Simulations of the threshold curves of two- and three-junction interferometers enabled understanding of experimental measurements of the first circuits.
>
> A simple A/D converter design was invented. The design greatly reduced the complexity of the expected chip layout and testing, making possible an early demonstration of a 4-bit A/D converter.

In Section 2 we summarize the main portion of the work. Details are presented as reprints in the Appendix. The work described is the demonstration of a very high speed superconducting A/D converter, the calculation of threshold curves of interferometers, theoretical analysis of an alternate design of an A/D converter, and experimental and theoretical work on striplines.

In Section 3 we describe other work, supported by ONR, but under a different contract. Much of this work is closely related to the A/D converter work. We discuss the demonstration of a 9 ps risetime sampler and a demonstration of the quietest known microwave mixer at 36 GHz.

Section 4 contains a discussion of those few elements of the project which have not been submitted for publication. These are a complete description of the present fabrication process, the details of the process for fabrication of resistors, the fabrication of several test circuits, and a few comments on factors limiting yield.

2.0 CONTRACT WORK PUBLISHED IN THE LITERATURE

The work which directly resulted from the ONR contract on high speed A/D conversion will result in five publications. These papers are included in the Appendix and are described briefly below:

2.1 Multiple-Quantum Interference Superconducting A/D Converter
R. E. Harris, C. A. Hamilton, and F. L. Lloyd
Appl. Phys. Letters, July 15, 1979.

This paper describes the essential work under the contract. A novel design was invented for a very simple, fully parallel A/D converter. The design makes possible an N-bit converter using only N gates. The Gray code output of the converter results naturally from the design. Sampling rates for the two bits tested were 2×10^8 per second. Conventional sampling measurements on one bit suggested the entire device will operate at 7×10^8 per second. The major limitation appears to be cross-talk between the leads to the chip. It is expected that future versions of the devices will operate at speeds well into the 10^9 samples per second region.

2.2 Analysis of Threshold Curves for Superconducting Interferometers
R. L. Peterson and C. A. Hamilton
J. Appl. Physics, 50, 8135 (1979).

Theoretical work in support of the experimental demonstration of a very high speed A/D converter was concentrated on the analysis of threshold curves of superconducting interferometers. These devices are the gates used in the A/D converter. The details of their interference patterns provide the basis for the operation of the A/D converter.

In the absence of perfect fabrication and testing in a zero-field, zero-transient environment, superconducting three-junction interferometers do not behave in the ideal manner described previously in the literature. This theoretical work provides a description of non-ideal behavior due to asymmetries in junction critical currents and loop inductances, and due to trapped flux. The work provides the basis for understanding how nearly identical critical currents and loop inductances must be in order to achieve interferometers having the required characteristics. It further provides motivation for using two-junction interferometers in the future, rather than three-junction ones as in the past.

2.3 Analog-to-Digital Conversion with a SQUID: Conditions for a Countable Pulse Train
R. L. Peterson
J. Appl. Phys. 50, 4231 (1979).

This work provides a theoretical analysis of a different type of superconducting A/D converter than the one demonstrated under the contract. This one is based on a Josephson junction in a superconducting loop (single junction SQUID). The device generates pulses as the magnetic flux through the loop is raised and lowered by an applied field. Counting the pulses provides a measure of the analog value of the magnetic flux. The work determines conditions on circuit parameters required for well-resolved pulses. The capacitance is shown to be especially critical.

2.4 Attenuation in Superconducting Striplines
R. L. Kautz
IEEE Trans. Mag. MAG-15, 566 (1979).

Superconducting striplines provide an important part of the advantage of superconducting electronic technology. They are essentially lossless and dispersionless, providing the capability of transmitting signals with frequency components in the THz (10^{12}) region over relatively long distances. This work provides an experimental measure of the losses in such lines. At 4 K the attenuation between 50 and 500 MHz is proportional to frequency and probably results from dielectric losses. Extrapolation of the dielectric losses to 10 GHz yields an attenuation of 10 dB/m, leading to losses acceptable for most microcircuit applications where stripline lengths are 1 cm or less.

2.5 Miniaturization of Normal-state and Superconducting Striplines
R. L. Kautz
J. Res. Nat'l. Bur. Stds. 84, 247 (1979).

Theoretical work has been performed to quantitatively determine the advantages offered by superconducting striplines, as compared with normal ones. The work employs all of the relevant theory to characterize both superconducting and normal striplines. For normal conductors, the Reuter-Sondheimer theory is applied in order to account for the effects of finite film thickness and mean free path. For superconductors the Mattis-Bardeen theory is used in order to include effects due to the energy gap. Comparisons are made for three example conductors: copper at 295 K and 4.2 K and niobium at 4.2 K. Simulations of pulse transmission on lines having 0.2 micron dielectric thickness indicate limitations of the copper lines for transmitting 50 ps pulses (half-width at half-maximum) more than 0.1 cm for 295 K and 1.0 cm for 4.2 K. On the other hand, superconducting lines will carry 1 ps pulses 10 cm with little distortion.

3.0 RELATED PUBLISHED WORK SUPPORTED UNDER OTHER ONR CONTRACTS

Additional work has been supported by the Office of Naval Research under contract number N00014-79-F-0020 and, of course, by the National Bureau of Standards. Much of this work is closely related to the ONR A/D converter work for two reasons. First it demonstrates the technical capability which the Cryoelectronics Group can bring to bear on the A/D converter problem, and second, it provides tools which can be used in future A/D converter work. Two relevant papers are discussed below and also included in the Appendix.

3.1 A Superconducting Sampler for Josephson Logic Circuits

C. A. Hamilton, F. L. Lloyd, R. L. Peterson, and J. R. Andrews
Appl. Phys. Letters, Nov. 1, 1979

A superconducting on-chip sampler has been developed which measures risetimes as short as 9 ps. The sampler uses a single biased Josephson junction on the chip containing the signal to be measured. The junction converts a given signal level to a time delay which is measured outside the cryogenic region by a conventional sampling oscilloscope. Such samplers will be used in the future to fully characterize the speed of A/D converters.

3.2 Quasiparticle Heterodyne Mixing in SIS Tunnel Junctions

P. L. Richards, T. M. Shen, R. E. Harris, and F. L. Lloyd
Appl. Phys. Letters, 34, 345 (1979).

The fabrication technology which has been developed was used to fabricate microwave mixers which were evaluated at 36 GHz and found to be the quietest mixers yet developed for that frequency. The work was done in collaboration with the University of California at Berkeley where the testing was done. Although the mixers were superconductor-insulator-superconductor junctions which exhibited the Josephson effect, it was the energy gap structure which provided the basis for the mixing. The project is continuing in the direction of multiple junction series arrays and higher frequencies.

4.0 UNPUBLISHED RESULTS

This Section describes some unpublished results which may be useful to others in the field. All of the work was either on a procedure necessary to accomplish other goals, or was on a device built and tested in order to learn the technology.

4.1 Special Equipment

A variety of special pieces of equipment are now in use and are described below. Many of these items were specially designed and constructed for this work and have played a vital role in the accomplishments to date. Of particular interest, several items of test equipment were required for the characterization of our superconducting A/D converters.

3.0 RELATED PUBLISHED WORK SUPPORTED UNDER OTHER ONR CONTRACTS

Additional work has been supported by the Office of Naval Research under contract number N00014-79-F-0020 and, of course, by the National Bureau of Standards. Much of this work is closely related to the ONR A/D converter work for two reasons. First it demonstrates the technical capability which the Cryoelectronics Group can bring to bear on the A/D converter problem, and second, it provides tools which can be used in future A/D converter work. Two relevant papers are discussed below and also included in the Appendix.

3.1 A Superconducting Sampler for Josephson Logic Circuits

C. A. Hamilton, F. L. Lloyd, R. L. Peterson, and J. R. Andrews
Appl. Phys. Letters, Nov. 1, 1979

A superconducting on-chip sampler has been developed which measures risetimes as short as 9 ps. The sampler uses a single biased Josephson junction on the chip containing the signal to be measured. The junction converts a given signal level to a time delay which is measured outside the cryogenic region by a conventional sampling oscilloscope. Such samplers will be used in the future to fully characterize the speed of A/D converters.

3.2 Quasiparticle Heterodyne Mixing in SIS Tunnel Junctions

P. L. Richards, T. M. Shen, R. E. Harris, and F. L. Lloyd
Appl. Phys. Letters, 34, 345 (1979).

The fabrication technology which has been developed was used to fabricate microwave mixers which were evaluated at 36 GHz and found to be the quietest mixers yet developed for that frequency. The work was done in collaboration with the University of California at Berkeley where the testing was done. Although the mixers were superconductor-insulator-superconductor junctions which exhibited the Josephson effect, it was the energy gap structure which provided the basis for the mixing. The project is continuing in the direction of multiple junction series arrays and higher frequencies.

4.0 UNPUBLISHED RESULTS

This Section describes some unpublished results which may be useful to others in the field. All of the work was either on a procedure necessary to accomplish other goals, or was on a device built and tested in order to learn the technology.

4.1 Special Equipment

A variety of special pieces of equipment are now in use and are described below. Many of these items were specially designed and constructed for this work and have played a vital role in the accomplishments to date. Of particular interest, several items of test equipment were required for the characterization of our superconducting A/D converters.

4.1.1 High Speed Probe - The most crucial item has been a probe for mounting the sample integrated circuit chips and delivering to and from them high speed signals over a large number of lines. The basic design of this device was reported last year. Since then five more probes have been built with numerous changes designed to improve the three most important requirements: contact reliability, large bandwidth, and absence of crosstalk between lines. Contact reliability has been improved by developing a special printed circuit board on which the contact fingers are formed from beryllium copper and thus have individual compliance with every chip pad. Bandwidth has been improved by better matching the contact finger striplines to the 50 ohm coaxial cables which carry signals to room temperature. Crosstalk between power supply and output signals has been identified as a major problem in high speed testing. The crosstalk in our probe is largely a result of excess inductance in making a common ground contact to the ground plane on the chip. Crosstalk has been reduced by about a factor of four by a modification which reduces this inductance. Further reduction is required and will be accomplished by a new probe design in which each signal line has its own individual ground line to the coaxial shield.

4.1.2 A/D Converter Test Electronics - Another item of test equipment designed and fabricated this year is an electronics box for interpreting A/D converter output. This box allows a direct plot of the input-output characteristics as shown in Fig. 2 of Appendix A. It consists of (1) four low-level voltage comparators to convert Josephson logic levels to CMOS levels, (2) a Gray code to binary code converter, and (3) a D/A converter. This device has proved to be invaluable in setting the drive conditions for accurate A/D converter operation.

4.1.3 Deposition System Automation - The vacuum system in which lead alloy films are deposited and in which oxidation is done, has been significantly automated. The automation eliminates many possibilities for human error and speeds the process. The greater speed of the film thickness monitor now in use also increases the degree of control over film thicknesses. The system performs the following functions: the proper source is moved directly under the substrate, the source is heated and the evaporation rate is controlled, the shutter is automatically opened and closed, and the process is repeated for up to a total of four layers.

4.1.4 Move into Clean Room - All of the fabrication equipment has been moved from an ordinary laboratory into a Class 300 clean room. The move not only eliminates dust, but also centralizes the optical mask making, fabrication, and soon-to-be-installed electron beam fabricator. The move has required significant time during this contract year, but overall it should prove to be extremely beneficial.

4.2. Present Fabrication Process

The present fabrication process is slightly different from that described in the last Annual Report. Although it is much like one in the literature (1), the films are about 20% thinner. The process is described here in its entirety and summarized in Table I.

4.2.1 Substrates - The substrates are silicon wafers which are insulated with SiO(2). These wafers have a 2 inch diameter and 0.010 inch thickness. They are purchased from an outside vendor with the SiO(2) already formed.

4.2.2 Layer 1: Niobium Ground Plane - Niobium is deposited onto the wafer by e-beam evaporation in an ultra-high vacuum system. The films are nominally 4000 Angstroms thick. They are subsequently patterned by selective etching. The parts which are not to be etched are protected by a patterned layer of Shipley AZ-1350J or AZ-1370 photoresist. The etchant is a mixture of 1 part hydrofluoric acid, 9 parts nitric acid, and 20 parts water, all measured by volume. The etching is done at room temperature.

4.2.3 Layer 2: Nb(2)O(5) Ground Plane Insulator - The Nb(2)O(5) insulation is formed by anodizing the Nb ground plane. Some areas of the ground plane must remain uninsulated, however, to permit electrical contact. One might think of using Shipley 1350 Series resist to protect these regions from anodization. However, the anodizing solution is a solvent for this resist. Therefore, the areas of niobium which are to remain uninsulated are coated with 1000 Angstroms of aluminum patterned using the lift-off process. The anodization is carried out in a solution (2) of 18 g or ammonium pentaborate in 200 ml of ethylene glycol at 70 C. The thickness of the Nb(2)O(5) is approximately proportional to the anodization voltage, the ratio being in the range 22 to 24 Angstroms/volt. Layers of 700 to 2000 Angstrom thickness have been made. The protective aluminum layer is removed in 50% H(3)PO(4) at 60 C.

It is our impression that the present IBM process employs photoresist to prevent regions from being anodized. Such a process might be faster than the one discussed here.

4.2.4 Layers 3, 6, 9, and 11: SiO - Silicon monoxide is evaporated in a high vacuum system, with a pressure during evaporation of about 1×10^{-6} mm Hg. The material used is a powder which is evaporated from a baffled source designed especially for SiO. Both powder and source are commercially available. The SiO is evaporated at a rate of about 20 Angstroms/s. The thicknesses used are layer 3, 2500; layer 6, 3660; layer 9, 7200; and layer 11 (rarely used), about 10000 Angstroms.

4.2.5 Layer 4: AuIn(2) Resistors - The material used for resistors is AuIn(2), an intermetallic which is present in the base electrode of the junction. Resistors consist of 46 wt. percent Au and 54 wt. percent In. With total film thickness of 437 Angstroms, the resistivity is 1 ohm per square within a few percent. The layers are deposited with the following thicknesses: In, 165; Au, 107; In, 165 Angstroms. No difficulties have been experienced with these resistors. They have shown negligible resistance change with up to 20 thermal cycles and room temperature storage for one month.

TABLE I

Layer	Material	Thickness (Angstroms)	Function
1	Niobium	4000	Ground plane. Defines magnetic field configuration near junctions and forms striplines from conductors above it.
2	Nb(2)0(5)	700	Insulator above ground plane.
3	SiO	2500	Additional insulator above ground plane. Low dielectric constant and readily variable thickness permit good control of stripline impedance.
4	AuIn(2)	437	Resistors for terminating striplines, voltage dividers, damping interferometers, etc.
5	Pb alloy Pb (88%) In (8%) Au (4%)	3280	Junction base electrode and stripline conductor.
6	SiO	3660	Forms window through which barrier is formed. Minimizes anomalous effects at junction edges.
7	Pb(x)0(y)	20-50	Insulating tunneling barrier formed by oxidizing base electrode.
8	Pb alloy Pb (98%) Au (2%)	4040	Junction upper electrode.
9	SiO	7200	Insulator between junctions and control leads.
10	Pb alloy	8002	Control leads for junctions and additional stripline conductors.
11	SiO	10000	Protective layer for entire circuit.

4.2.6 Layer 5: Pb-In-Au Base Electrode - The base electrode is formed by a sequential evaporation of In, Au, and Pb having thickness 400, 80, and 2800 Angstroms respectively. During the baking of photoresist for the next layers, these films intermix to form a homogeneous alloy. The heat treatment is at 70 C for 25 minutes.

4.2.7 Layer 7: Tunneling Barrier - The tunneling barrier is formed by oxidizing the base electrode through openings in the photoresist pattern for layer 8 and, usually, the SiO of layer 6. The oxidation process is described in three publications (3-5) and other references therein. It involves using rf sputtering in oxygen to remove the surface of layer 5. Since the surface continually reoxidizes, an equilibrium between the rate of removal of material and the rate of reoxidation occurs. The equilibrium takes place at a specific oxide thickness essentially independent of the time taken (beyond a few minutes). The oxygen pressure and the cathode self-bias voltage are carefully controlled to produce the desired thickness.

4.2.8 Layer 8: Upper Electrode - The upper junction electrode is formed through a sequential deposition of Pb, Au, and Pb, having thickness 2400, 40, and 1600 Angstroms respectively. This deposition immediately follows the formation of the oxide tunneling barrier (without opening the vacuum system). Homogenization of the alloy is promoted through baking of the photoresist in subsequent steps.

4.2.9 Layer 10: Pb-In-Au Control Lines - This layer is formed from the same alloy as the base electrode. However, it is thicker to provide good edge coverage over the intervening layers. The presence of indium in this electrode promotes its connection to other lead layers. If indium were not present, connections to other layers would be Josephson junctions, rather than the superconducting shorts which are desired. The thicknesses used are In, 976, Au, 196, and Pb, 6830 Angstroms respectively.

4.2.10 Design Rules Usually Used - Detailed design rules have not been worked out. However, several practices seem plausible and are usually followed.

4.2.10.1 Step Coverage - It has been found that step coverage is adequate if every layer is at least 400 Angstroms thicker than steps it must cover. This procedure provides adequate yield for the circuits we have fabricated to date.

4.2.10.2 Metal Layer Interconnections - It is thought that interconnections between metal layers are superconducting only if there is indium in the upper layer. The indium combines with any residual oxide at the interface, producing a short. Even with careful sputter cleaning of the interface prior to deposition of the upper layer, shorts are not formed without the upper layer indium. Thus there can be no interconnections (except Josephson junctions) between the counterelectrode and the base electrode. Connections between the counterelectrode and resistors are similarly avoided. Thus connections may be formed between resistor and base or control electrode, and they may be formed between counterelectrode and control electrode. Connections to the ground plane are from the base electrode, and infrequently from the control layer. No other interconnections are permitted.

4.3. Process for Fabricating Resistors at One Ohm/Square

It is useful to be able to deposit resistors of sufficiently high resistivity so that the length-to-width ratio of most resistors can be fairly low. Since the usual range of resistance we expect will be between 1 and 100 ohms, a resistivity of 1 ohm/square is satisfactory. The one reference available (6) at the time the work was done describes resistors having thickness of 2850 Angstroms and resistivity of 0.045 ohms/ square. The material is AuIn(2) deposited in a layered form in the order In-Au-In. We have tried this prescription and achieved a resistivity of 0.03 ohms/square. In order to increase the resistivity we decrease the film thickness while maintaining the ratio of In to Au. Achieved values of resistivity as a function of thickness are shown in Fig. 1. The curve is not quite smooth, probably because of errors due to our quartz crystal film thickness monitor. A sample error bar is shown for the left-most point. No changes in resistivity greater than 2 percent with room temperature storage or thermal cycling have been observed during a 20 day storage period and up to 23 thermal cycles. It appears possible to fabricate resistors having values within ten percent of that desired. Often results are within a few percent. Indeed the resistors are the most repeatable part of our fabrication process.

A new film thickness monitor has been installed in order to sample the film thickness more often (every 0.2 s compared to every 1 s before). In this way better control of thickness is expected.

4.4 Test Circuits Including 7-OR String

The following test circuits were fabricated and evaluated:

1. Shorts from the base electrode to the ground plane. Areas of 50 x 50 microns were found to have critical currents in excess of 40 mA. The standard size ground plane short now used is 20 x 20 microns and has a critical current known to be greater than 5 mA. Exact values of the critical current have not been determined as such measurements have not been required.

2. Numerous transmission lines. It is important to be able to predict the impedance of such lines. Impedance was calculated from

$$Z = (377/W)*((S1+S2+L1+L2)*(S1/e1+S2/e2))**(1/2)$$

where W is the width of the line, Sn is the thickness of the nth dielectric layer, Ln is the penetration depth of the nth metal film, and en is the dielectric constant of the nth layer. This formula assumes metal films which are thick compared to their penetration depths and wide compared to the dielectric thickness. As an example a 12 micron wide, lead alloy line was placed over a niobium ground plane covered with 1173 Angstroms of niobium oxide. The dielectric constant was assumed to be 29, the penetration depth

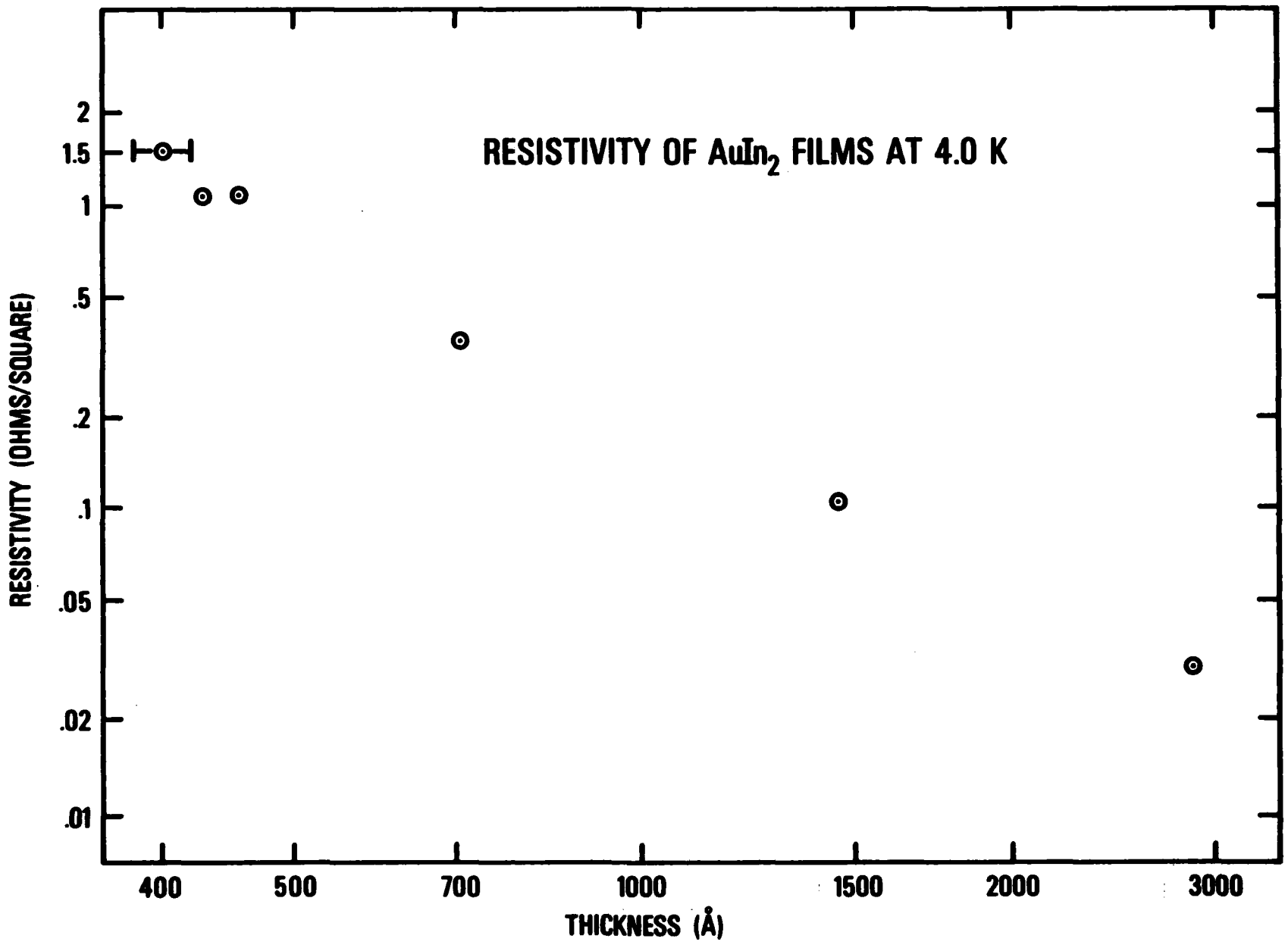
RESISTIVITY OF AuIn2 FILMS AT 4.0 K
RESISTIVITY (OHMS/SQUARE)
2
1.5
1
.5
.2
.1
.05
.02
.01
400
500
700
1000
1500
2000
3000
THICKNESS (Å)

Figure 1.

for the lead alloy was 1370 Angstroms, and for the niobium was 860 Angstroms. The calculated impedance was 1.17 ohms while that measured was 1.55 ohms, a difference of about 25%. However, when an additional layer of SiO, 5000 Angstroms thick, was added to the niobium oxide, the calculated impedance was 9.30 ohms while that measured was 9.52 ohms. The assumed SiO dielectric constant was 5. The difference in this case is less than 3 percent. These results suggest an error in the niobium oxide thickness.

Currently a more sophisticated formula is used to calculate impedance. The formula was obtained from Wen Chang of IBM Research, and is about to be published.

3. Junction matched to external transmission lines with 50 ohm resistors in order to evaluate risetime of probe. The probe risetime was found to be about 50 ps for a signal travelling on to or off a chip.

4. Bridge-type interferometer having two control lines. This device was the first fabricated which permitted logic to be performed. The functions AND, OR, exclusive OR, and NOT were performed at 25 MHz and provided our first experience with the difficulties of high speed testing.

5.0 ANTICIPATED FUTURE PROCESS CHANGES

1. A new upper electrode alloy has appeared in the literature (7,8). The alloy is 29 wt. percent bismuth in lead, deposited by evaporation from a premixed source. This material is reputed to provide reduced excess current, greater yield, and greater corrosion resistance. Initial experiments involving this alloy were unsuccessful, producing only uncontrollably high critical current densities. Further work is planned.

2. The use of thinner films (9) should improve cycling durability and improve edge coverage.

3. A niobium anodization process using photoresist instead of aluminum would speed that part of the process.

REFERENCES

1. J. H. Greiner, S. Basavaiah, and I. Ames, J. Vac. Sci. Technol. 11, 81, (1974).

2. T. W. Hickmott and W. R. Hiatt, Solid State Electronics 13, 1033 (1970).

3. R. H. Havemann, C. A. Hamilton, and R. E. Harris, J. Vac. Sci. Technol. 15, 392 (1978).

4. J. H. Greiner, J. Appl. Phys. 42, 5151 (1971).

5. J. H. Greiner, J. Appl. Phys. 45, 32 (1974).

6. S. K. Lahiri, Thin Solid Films 41, 209 (1977).

7. L. M. Geppert, J. H. Greiner, D. J. Herrell, and S. Klepner, IEEE Trans. Mag. MAG-15, 412 (1979).

8. S. K. Lahiri, IBM Tech. Disc. Bull. 21, 3403 (1979).

9. S. K. Lahiri and S. Basavaiah, J. Appl. Phys. 49, 2880 (1978).

APPENDIX A

Multiple-quantum interference superconduc[illegible]nalog-to-digital converter[a)]

Richard E. Harris, C. A. Hamilton, and Frances L. Lloyd
Electromagnetic Technology Division, National Bureau of Standards, Boulder, Colorado 80303

(Received 16 March 1979; accepted for publication 11 May 1979)

Multiple-quantum interference in a superconducting interferometer is used for analog-to-digital conversion. The simple fully parallel four-bit converter which is described is the first known use of this effect in a digital circuit. Sampling rates of 2×10^9 per second were achieved, and much higher rates appear possible.

PACS numbers: 06.60.Ja, 74.50. + r, 06.70.Dn, 06.70.Ep

This letter describes the first known use in a digital circuit of the multiple lobes of the threshold curve of a superconducting interferometer. Although digital applications of such interferometers have been known for several years,[1,2] only the first lobe has been used previously. An analog-to-digital (A/D) converter using multiple lobes has been proposed.[3,4] We demonstrate a realization of this concept in a four-bit A/D converter operating at a rate of 200 megasamples per second. An increase to rates well above one gigasample per second may be possible.

This experiment makes use of four current comparators, each consisting of a Josephson three-junction interferometer which has the junctions connected in parallel by superconducting loops.[3] A photograph of one of the interferometers is shown in Fig. 1 (a). The center junction has twice the critical current of each of the symmetrically arranged outer junctions. Such an interferometer has a current-voltage characteristic like that of a single junction. Its maximum 0-V current I_m (threshold current) is modulated by an applied magnetic field in a way determined by the junction critical currents and the loop inductances. The junctions are sufficiently small (about 4 μm square) that the magnetic fields used have negligible effect on them directly. By choosing $Li_0 \simeq \frac{1}{2}\phi_0$, a threshold curve like that shown in Fig. 2(a) is obtained. Here L is the inductance of one of the superconducting loops, i_0 is the critical current of one of the outer junctions, and ϕ_0 is the flux quantum $h/2e$.

The periodicity of the threshold curve is a manifestation of quantum interference occurring in the interferometer. The net phase change of the wave function describing the superconducting loops in the interferometer increases in proportion to the amount of magnetic flux applied through the loops of the interferometer. A net phase change of 2π corresponds to one additional flux quantum penetrating the loop. The threshold curve repeats whenever two additional flux quanta are added. In a two-junction interferometer, the curve would repeat for each additional flux quantum.

To use this interferometer as a current comparator, a magnetic field is applied equally through both loops. The magnetic field results from passing a current I_c through a control line above the interferometer. Its effect is illustrated by the horizontal arrow in Fig. 2(a). The current through the interferometer I_g is then raised from zero to a predetermined level $I_{g,max}$ indicated by the vertical arrow. If $I_{g,max}$ is above the threshold curve $I_m(I_c)$, the interferometer switches to the voltage state; otherwise it does not.

A single interferometer is used to generate a single bit of the output of an A/D converter, by choosing $I_{g,max}$ so that the interferometer switches, or does not switch, for equal intervals of control current. By making the control current the analog signal to be digitized, the voltage output of the gate V_g is one bit of the digital value of the signal as illustrated in Fig. 2(b). To take repeated samples, I_g is cyclically varied between 0 and $I_{g,max}$.

The next most significant bit can be generated by expanding the bit pattern of the least significant bit by a factor of 2. The expansion is produced by reducing the coupling of a second interferometer to the control line by a factor of 2. Similarly, the third and fourth bits are generated by further expanding the bit patterns of third and fourth interferometers. Thus only four interferometers are required for A/D conversion of four-bit accuracy. Moreover, since these interferometers operate in parallel, maximum speed is achieved with all four bits being produced essentially simultaneously. In general, only N interferometers are required to digitize to N-bit accuracy, with little decrease in speed needed for additional bits.

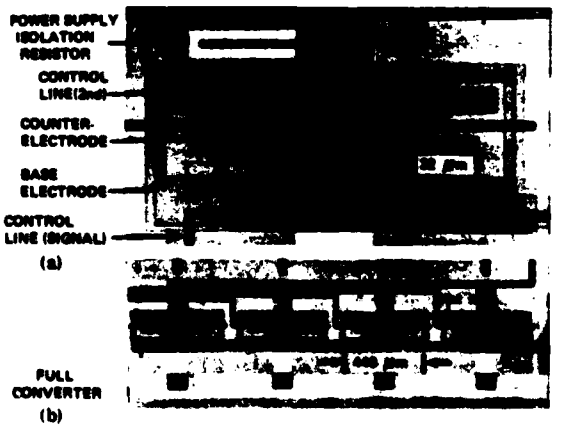

FIG. 1. (a) Photograph of one of the four interferometers in the A/D converter. (b) Photograph of a complete four-bit converter.

[a)]Work supported in part by the Office of Naval Research under contract number N00014-77-F-48.

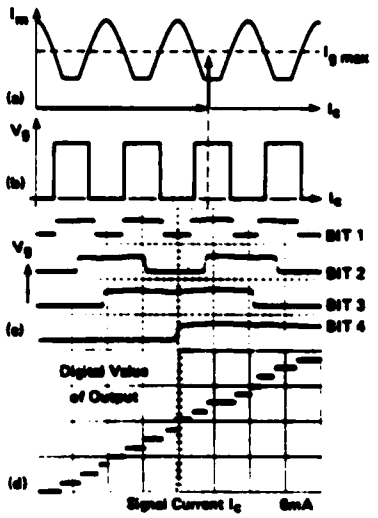

FIG. 2. (a) Threshold curve showing maximum zero voltage current I_m as a function of control current I_c. Ideal maximum curve current $I_{g,max}$ is shown by dashed line. (b) Output voltage for ideal $I_{g,max}$ as function of control current. (c) Actual bit pattern for the four-bit A/D converter. (d) Value of digital output of converter versus analog signal (traced).

Figure 1 (b) shows a complete four-bit converter. The observed bit patterns for this converter are shown in Fig. 2(c). This pattern is a Gray code representation of the analog signal. Gray code is frequently used in A/D conversion since only one bit changes as the signal crosses from one digital level to the next. Another significant feature of this A/D converter can be realized by adding a second control line to each interferometer. By applying a dc bias through one of these control lines, the bit pattern from that gate can be shifted to values of higher or lower current. Using this feature, a variety of unique codes can be produced.

Superconducting A/D converters of the type described have been fabricated with two converters on each 6.4-mm-square chip. The interferometers are much like those described in Ref. 5, although they are scaled up in linear size by a factor of 4 to make fabrication simpler. The circuits contain resistors for damping the interferometer resonances and for terminating transmission lines. The impedances of the striplines on the chip are chosen for proper matching to the interferometer impedances. The coupling of the signal to the interferometers is varied by adjusting the length of the control line above the interferometers in the ratios 1:2:4:8. As can be seen in Fig. 1, the control line is diverted around the portion of the wide counterelectrode passing over the interferometer. In this region the counterelectrode provides shielding which is not readily calculable. Furthermore, this control-line arrangement causes the coupling to each half of each interferometer to be insensitive to slight misalignment during fabrication.

The interferometers have been tested with a gate current having a frequency (i.e., sampling rate) of 200 MHz. Due to equipment limitations only two of the four bits were tested at this speed. They were found to produce outputs which repeat synchronously with a nominally 50-MHz signal. In this sense, the converter has been demonstrated to operate at 200 megasamples per second. Based on the observed switching times, we believe that the devices fabricated will operate properly at rates up to about 700 megasamples per second. Improving the ground plane contacts should allow the converter to operate at much higher rates. Reported switching times[4] of 42 ps for these devices suggest rates well above 1 gigasample per second.

To assess the accuracy of the full device, conventional circuitry was used to convert from Gray code back to an analog signal. The resulting output-vs-input curve [Fig. 2(d)] is monotonic with a maximum error in step width of 0.7 least significant bits. These measurements were performed at about 10 megasamples per second with the signal swept at a few hundred hertz.

The coupling of the signal to the interferometers was determined to be in the ratio 1:2:4:8 within about 1%, indicating that this design may be suitable for converters of 6 to 8 bits.

The initial tests of this A/D converter design suffer from variations in interferometer characteristics, trapped flux, and the general difficulties of high-speed testing. In addition the ultimate accuracy of the device may be limited by dynamic effects including subthreshold switching and signal line transients caused by switching. Nevertheless, the design appears to offer great promise for significantly higher speeds in the future.

It is a pleasure to acknowledge helpful conversations with T. Fulton, L. Geppert, D. Herrell, and H. Zappe. R. Peterson assisted with the understanding of the threshold curves, D. McDonald provided constant encouragement, and L. Mullen assisted with the fabrication.

[1]H.H. Zappe, Appl. Phys. Lett. 27, 432 (1975).
[2]A superconducting successive approximations A/D converter was reported by M. Klein, ISSCC 20, 202 (1977).
[3]H.H. Zappe, IBM Tech. Discl. Bull 17, 3053 (1975). Zappe's paper describes a related method of producing the various bits, but achieves the expansion of the patterns from one bit to the next by changing the inductances of the interferometers. The present approach of changing the coupling allows the use of optimally designed interferometers, each having identical response time, for each of the bits.
[4]An optical interference analog of the present converter is given by H.F. Taylor, Proc. IEEE 63, 1524 (1975); Appl. Phys. Lett. 32, 599 (1978).
[5]M. Klein, D.J. Herrell, and A. Davidson, ISSCC 21, 62 (1978); L.M. Geppert, J.H. Greiner, D.J. Herrell, and S. Klepner, IEEE Trans. Mag. MAG-15, 412 (1979).

APPENDIX B

Analysis of threshold curves for superconducting interferometers

R. L. Peterson and C. A. Hamilton
Electromagnetic Technology Division, National Bureau of Standards, Boulder, Colorado 80303

(Received 11 June 1979; accepted for publication 14 August 1979)

Threshold curves for multijunction superconducting interferometers have been calculated previously, showing general agreement with observed features, especially in symmetric cases. We here add some more details to the analysis, paying particular attention to the effects of asymmetries in coupling, inductance, or critical currents. Feed-loop inductance and flux quantization in the feed loop can be important. A changing lobe pattern over many periods, asymmetries within a period, shifting patterns between runs spanning a warm-up, and sudden changes in pattern because of noise in the environment are all quantitatively explainable on the basis of this model. By use of a single "calibration curve", the inductance for symmetric two- or three-junction interferometers can be obtained immediately.

PACS numbers: 74.50. + r, 85.25. + k

I. INTRODUCTION

A superconducting interferometer—a device containing two or more Josephson junctions connected in superconducting loops—is attractive for use in logic circuits because of its high sensitivity, high speed, good current transfer, and small heat dissipation. It can also be modeled quite accurately, as we hope to emphasize in this paper. One characterization of such a device is its threshold curve, $I_m(B)$ or $I_m(I_c)$, where I_m is the maximum bias current the device can accommodate before developing a voltage, and I_c is a control current, whose magnetic induction B threads the loops of the interferometer. The calculation of these threshold curves, or certain properties of them, has been the subject of many papers.[1-14]

The purpose of the present paper is to extend the analysis of the threshold curves in several directions. The empirical curve obtained by De Waele and De Bruyn Ouboter[3] for a double-junction interferometer, which provides a method for the rapid determination of the inductance of symmetric interferometers, is shown to be valid for the three-junction interferometer as well. Approximate analytical expressions for this curve are developed. We show the importance of including parameters of the feed loop—both its inductance and possible trapped flux—in the analysis. The effects of various asymmetries, whether in junction critical currents, loop inductances, or flux coupling, are discussed in some detail. We also summarize the salient features of the threshold curves, many of which have been mentioned before but not in one place. Finally, we make comparisons with some threshold curves measured for three-junction interferometers with slightly asymmetric coupling.

II. THEORY

The technique of constraint maximization, which is the calculational method we have used, has been described adequately before.[8,9] Briefly, one wishes to calculate the maximum or threshold value I_m of the gate current

$$I_g = \sum I_{0i} \sin\phi_i \,, \tag{1}$$

which can flow through all the junctions before a voltage develops. In Eq. (1), ϕ_i is the phase difference across the ith junction of critical current I_{0i}, and the summation is over all junctions in the interferometer. This relation is subject to the constraints imposed by fluxoid quantization within each loop, which may be written, for loop k,

$$f_k = \phi_{xk} + \sum(L_i I_i + \phi_i \Phi_0/2\pi) - N_k \Phi_0 = 0 \,. \tag{2}$$

In Eq. (2), ϕ_{xk} is the external flux in loop k, whether intentional, as from a control line, or accidental, as from flux trapped nearby in a ground plane. Also, I_i is the current flowing through inductance L_i, $\Phi_0 = 2.0685 \times 10^{-15}$ Wb is the flux quantum, and N_k is an integer. The summation is over all inductances and junctions in loop k, and may also include mutual inductances from other loops. To find the extrema of I_g, one uses the technique of Lagrange multipliers, forming

$$\Gamma(\phi_1, \phi_2, \ldots; \lambda_1, \ldots) \equiv I_g + \sum \lambda_k f_k \,, \tag{3}$$

and requiring $\partial\Gamma/\partial\lambda_i = 0$ and $\partial\Gamma/\partial\phi_i = 0$. The first of these conditions simply reproduces Eq. (2). The second creates a set of equations which overdetermine the λ_k, thus imposing relations among the ϕ_i. The sets $\{\phi_1, \phi_2, \ldots\}$ consistent with these relations are the allowed solutions. The threshold current I_m is found by substituting these values into Eq. (1). Generally the sum of all $f_k = 0$ equations results in a convenient equation into which the solution set $\{\phi_1, \phi_2, \ldots\}$ is substituted, thus giving the value of I_c or total flux ϕ_x to be paired with the calculated I_m.

This technique yields unstable as well as stable solutions. The unstable points can be rejected by evaluating the Hessian of the potential energy[9,11] (second derivatives of the Gibbs free energy G relative to principal axes) and retaining only the positive values. Although relatively simple for two-junction interferometers, evaluation of the Hessian can be quite involved for three-junction cases, especially when feed loops are considered. Landman[7] used an alternative approximate procedure. We have found that use of the necessary, but not sufficient, condition

$$1 + (LI_{0i}/\bar{\Phi})\cos\phi_i > 0 \,, \tag{4}$$

will reject most of the unwanted points. Here and subse-

 0021-8979/79/128135-08$01.10

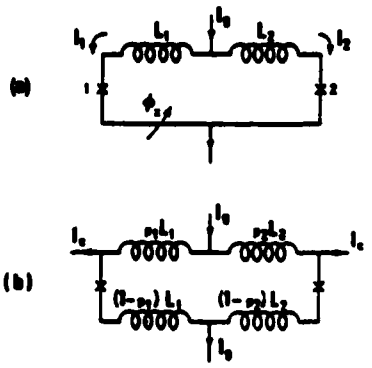

FIG. 1. Circuit diagrams for two-junction interferometers. (a) shows a magnetic flux ϕ_x threading the loop. (b) shows a control current injected directly into the interferometer, which may necessitate partitioning the inductances.

quently we use the convenient "phi-bar" symbol $\bar{\Phi} = \Phi_0/2\pi$. The inductance L in Eq. (4) is typically the inductance through which the junction current flows. Equation (4) is derivable from, but not generally identical to, $\partial^2 G/\partial\phi_i^2 > 0$ (i.e., the derivative condition before transformation to principal axes). In special cases, the latter is simple to evaluate and is an improvement over Eq. (4). However, we find that the simple Eq. (4) is usually quite satisfactory.

III. TWO-JUNCTION INTERFEROMETER

Various facets of the threshold curves for two-junction interferometers have been given earlier.[1-6,8,10-13] Fulton *et al.*[4,5] and Schulz-DuBois and Wolf[11] have given rather detailed analyses, and we shall add just a few new points here, while repeating some earlier material bearing on measurable quantities.

For the two-junction interferometer as depicted in Fig. 1(a), the equations are

$$C_2 = -C_1/(I_{02}/I_{01} + \beta C_1), \tag{5}$$

$$I_m = I_{01}S_1 + I_{02}S_2, \tag{6}$$

$$\theta = \phi_2 + \beta_2 S_2 - \phi_1 - \beta_1 S_1 + 2\pi N, \tag{7}$$

where $S_i = \sin\phi_i$, $C_i = \cos\phi_i$, $\beta = \beta_2 + \beta_1 I_{02}/I_{01}$, $\beta_i = L_i I_{0i}/\bar{\Phi}$, and $\theta = \phi_x/\bar{\Phi}$. Equations (5)–(7) show that I_m is periodic in θ with period 2π. Commonly, the phases ϕ_i are restricted to the range $-\pi < \phi_i < \pi$, and the integer N of Eq. (7) is changed to obtain the contour of a different fluxoid quantum state. However, there are ranges of parameter values, such as observation (3) below, where this identification of fluxoid states is not very meaningful, as Schulz-DuBois and Wolf[11] also point out. Clearly, one can alternatively set $N = 0$ and allow the ϕ_i to span an extended range.

We now make a few observations about double-junction interferometers which relate generally to measurable features, and from which the junction parameters may be deduced.

(1) $\phi_1 = \phi_2 = \pm\frac{1}{2}\pi$ are always solutions, even for asymmetric feeds or critical currents, as Eq. (5) shows. For these phases, $I_m = \pm(I_{01} + I_{02})$. Thus the maximum current is always the sum of the junction critical currents, which is not the case with the three-junction interferometer. Also, $\theta = \pm(\beta_2 - \beta_1) + 2\pi N$, or $\phi_x = \pm(L_2 I_{02} - L_1 I_{01}) + N\Phi_0$, at these extrema. Measurement of the relative displacement of the minimum and maximum of I_m thus provides one measure of the asymmetry. The three curves of Fig. 2 show this displacement. These points have been made earlier.[3,5,8,10,11]

(2) An asymmetry of the feed injection point ($L_1 \neq L_2$) while the junction critical currents are kept equal will leave the cusp ends of the lobes on the $I_m = 0$ axis, as curve (a) of Fig. 2 shows. Where there is an asymmetry of the critical currents, these ends will lift off from the $I_m = 0$ axis to near the values $\pm(I_{01} - I_{02})$. These currents are actually the points of zero slope, as evaluation of $dI_m/d\theta$ shows, and occur at, e.g., $\phi_1 = \frac{1}{2}\pi$ with $\phi_2 = \mp\frac{1}{2}\pi$, giving $\theta = \mp(\pi + \beta_2 + \beta_1) + 2\pi N$. Curve (b) of Fig. 2 and the inset illustrate this effect. In principal, a dynamic experimental procedure might be used to locate these extrema. These together with the measured maximum of I_m completely specify the critical currents. Reference 11 supplies additional details about the nature of the cusps.

(3) Both from experiments and graphical analysis, Fulton *et al.*[5] noted that double-junction interferometers can exhibit nearly sinusoidal I_m (I_c) behavior. This result is easily deduced. When

$$I_{02}/I_{01} + \beta \ll 1, \tag{8}$$

Eq. (5) has a solution for ϕ_2 only for a limited range of ϕ_1 near $\frac{1}{2}\pi$, $\frac{1}{2}\pi$, etc. Setting $\phi_1 = \frac{1}{2}\pi$ and noting that Eq. (8) requires $\beta_2 \ll 1$ (β_1 is not required to be small however), we get $\phi_2 \simeq \theta + \beta_1 + \frac{1}{2}\pi$ from Eq. (7). Hence $I_m \cong I_{01} + I_{02}\cos(\theta + \beta_1)$, showing the sinusoidal behavior. Similarly, with $\phi_1 = -\frac{1}{2}\pi$, one gets $I_m \cong -I_{01} - I_{02}\cos(\theta - \beta_1)$. A symmetric interferometer

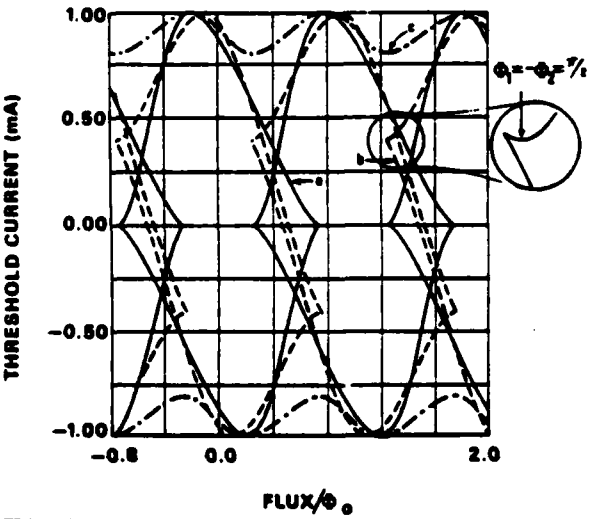

FIG. 2. Threshold curves for three double-junction interferometers having the same total inductance and total critical current. (a) $L_1 = 0.9$ pH, $L_2 = 0.1$ pH, $I_{01} = I_{02} = 0.5$ mA. (b) $L_1 = L_2 = 0.5$ pH, $I_{01} = 0.7$ mA, $I_{02} = 0.3$ mA. (c) $L_1 = L_2 = 0.5$ pH, $I_{01} = 0.9$ mA, $I_{02} = 0.1$ mA.

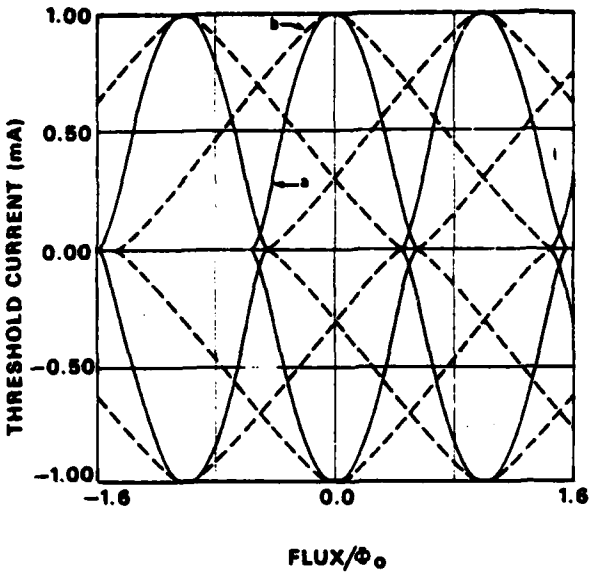

FIG. 3. Threshold curves for two symmetric double-junction interferometers. (a) $L = 0.2$ pH, $I_0 = 0.5$ mA, giving $\beta = 0.30$. (b) $L = 4.0$ pH, $I_0 = 0.5$ mA, giving $\beta = 6.1$.

can never exhibit this behavior since it cannot satisfy Eq. (8). Curve (c) of Fig. 2 shows that the threshold curve can be quite sinusoidal even when Eq. (8) is not particularly well satisfied ($I_{02}/I_{01} + \beta = 0.41$).

(4) When the interferometer is symmetric, there is always a slope discontinuity midway between the lobes at $\phi_x = \pm \frac{1}{2}\Phi_0$, etc. The interferometer is now governed by a single internal parameter β, which has the value of $LI_0/\bar{\Phi}$ where $L = L_1 + L_2$ is the total loop inductance and I_0 is the common junction critical current. Figure 3 shows two threshold curves for symmetric junctions with $\beta \ll 1$ and $\beta \gg 1$. The threshold current at the midpoints is a convenient measure of β. Curves of this current versus β based on numerical calculation have been given.[1,13] Although an exact formula for this curve has not been determined, formulas in the two limits can be established fairly easily. Figure 4 shows our calculated curve together with some analytical results in limiting cases.

For $\beta \ll 1$, Eq. (5) shows that ϕ_1 and ϕ_2 are separated by about π rad. Linearizing in β, one finds

$$\phi_2 = \phi_1 + \pi + \beta C_1^2/S_1 .$$

Substitution of this ϕ_2 into Eq. (7) with $\theta = \pi$ gives $C_1^2 = S_1^2$. Equation (6) then results in

$$|I_{mid}/I_{max}| = \tfrac{1}{2}\beta, \quad \beta \ll 1 . \tag{9}$$

When $\beta \gg 1$, Eq. (5) shows that $C_2 \approx -1/\beta$ when $\beta C_1 \gg 1$. Substitution of $\phi_2 = \frac{1}{2}\pi + 1/\beta + \cdots$ into Eq. (7) with $\theta = \pi$ then gives

$$\phi_1 + (\tfrac{1}{2}\beta)S_1 = \tfrac{1}{2}\beta - \tfrac{1}{2}\pi + O(\beta^{-1}) ,$$

which gives $\phi_1 = \frac{1}{2}\pi - (4\pi/\beta)^{1/2} + O(\beta^{-1})$. Hence

$$|I_{mid}/I_{max}| = 1 - \pi/\beta, \quad \beta \gg 1 . \tag{10}$$

This is equivalent to a modulation depth of Φ_0/L, a result noted earlier.[1,2]

However, a much better result can be obtained as follows, and now we generalize to permit asymmetric feed, although retaining $I_{01} = I_{02}$. At large β, the lobes degenerate toward parallelograms. Noting where the corners lie from the discussion of observations (1) and (2), one readily finds the equations for the straight-line segments of these parallelograms. The intersections lying highest (there can be more than one set of intersections at large β, as Fig. 3 shows) give

$$|I_{mid}/I_{max}| = \beta/(\pi + \beta), \quad \beta \gg 1 \tag{11}$$

and

$$\theta_{mid} = (2n+1)\pi + \beta(\beta_2 - \beta_1)/(\pi + \beta) . \tag{12}$$

Note that the current at the intersection is a function of β only, i.e., independent of the asymmetry, in this approximation. Fulton *et al.*[3] and Clarke and Paterson[4] had earlier noticed this independence from their numerical work. Figure 4 shows that this formula gives a better result than the preceding, and in fact is a fair approximation to the correct curve through the entire range of β. It is a useful analytical result since it allows a rapid determination of the inductance L from the threshold curve.

An alternative circuit for a double-junction interferometer is one in which the control current is injected directly into the interferometer, as shown in Fig. 1(b). Here, one must know what fraction of the total inductance is coursed by the control current, as illustrated in Fig. 1(b). It is this fraction which determines the period in I_c. The ϕ_x of the above formulas is now replaced by $(p_1 L_1 + p_2 L_2)I_c$. The remaining formulas are unaffected. Similarly, when the control line overlies the plane of the interferometer, the coupling is not generally perfect. When the widths of all lines are much greater than the distances separating them, and film thicknesses are much greater than their penetration depths, the control current can be treated as if directly injected and passing through all of the inductance of that length of line overlain by the control line. Since these conditions may not be met in some practical cases, the degree of coupling may be somewhat uncertain, and only a fraction of the inductance of

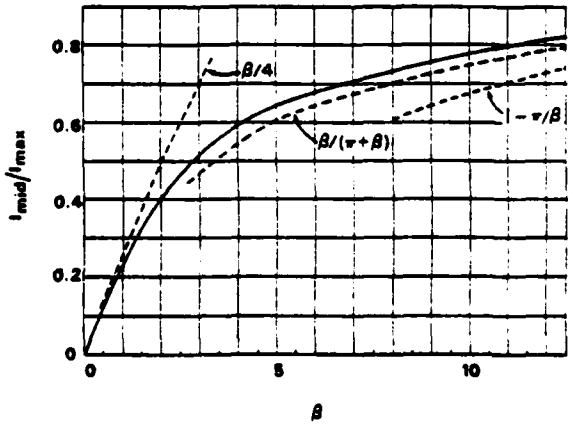

FIG. 4. Curve of the threshold current midway between maxima as a function of $\beta = LI_0/\bar{\Phi}$ (solid curve). The curves are valid for symmetric two- or three-junction interferometers as defined in the text.

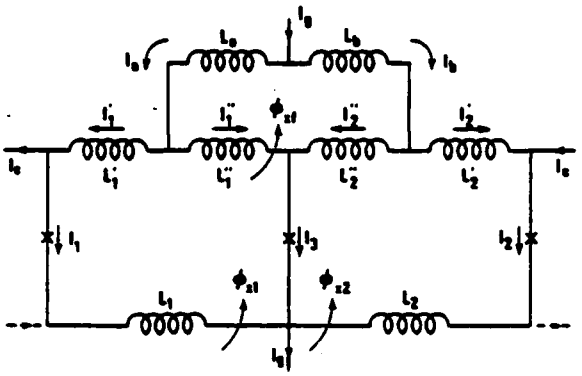

FIG. 5. Circuit diagram for a three-junction interferometer with a feed loop. Magnetic fluxes and direct injection of control current are shown together.

the overlain line is involved. In these cases the period of I_c in the lobe pattern is not a reliable measure of inductance, but is however a useful measure of the degree of coupling between control line and interferometer. Measurement of I_m at its lowest value between the lobes is superior for measurement of inductance in symmetric interferometers.

IV. THREE-JUNCTION INTERFEROMETER

An example of a three-junction interferometer circuit is shown in Fig. 5, in which a control current is injected directly into the interferometer, on the side containing a feed loop. Since the feed loop is entirely superconducting, flux quantization within it must be included in the analysis. This may be written

$$L_a I_a + L_1'' I_1'' - L_2'' I_2'' - L_b I_b + \phi_{xf} = N_f \Phi_0 , \tag{13}$$

where we have used the notation indicated in Fig. 5. ϕ_{xf} is feed loop flux from sources other than the control current, for example from flux trapped in the ground plane, and N_f is the number of flux quanta trapped in the feed loop. One may eliminate, e.g., I_a, I_b, and I_2'' in favor of I_1'', I_c, I_1, I_2, and I_3 by using the Kirchoff current equations, and solve Eq. (13) for I_1''. Substitution into the two fluxoid quantization conditions for the two loops containing the junctions then gives

$$\begin{aligned} f_1 &= \phi_{x1} + \alpha_1 \phi_{xf} + [L_1' + \alpha_1 (L_a + L_b)] I_c \\ &+ (L_1 + L_1' + \alpha_1 L_a) I_1 - (M + \alpha_1 L_b) I_2 \\ &- \alpha_1 (L_2'' + L_b) I_3 + \bar{\Phi} (\phi_1 - \phi_3) - (N_1 + \alpha_1 N_f) \Phi_0 \\ &= 0 , \end{aligned} \tag{14}$$

$$\begin{aligned} f_2 &= \phi_{x2} + \alpha_2 \phi_{xf} + [L_2' + \alpha_2 (L_a + L_b)] I_c \\ &+ (M + \alpha_2 L_a) I_1 - (L_2 + L_2' + \alpha_2 L_b) I_2 \\ &+ \alpha_2 (L_a + L_1'') I_3 + \bar{\Phi} (\phi_3 - \phi_2) - (N_2 + \alpha_2 N_f) \Phi_0 \\ &= 0 , \end{aligned} \tag{15}$$

where $\alpha_1 = L_1''/L_f$, $\alpha_2 = L_2''/L_f$, and $L_f = L_a + L_b + L_1'' + L_2''$. ϕ_{x1} and ϕ_{x2} have the same meanings as described for ϕ_{xf} above.

Following Tsang and Van Duzer,[8] we have included a "mutual inductance" M, representing coupling between the two loops. One sees from the terms $\alpha_1 L_b$ and $\alpha_2 L_a$ added to M that the feed loop also facilitates coupling between the loops. The terms containing N_f show that flux trapped in the feed loop adds fractionally to the flux in the other loops.

The "Lagrangian current" is now formed according to Eq. (3). The equations $\partial \Gamma / \partial \phi_i = 0$, with $i = 1, 2, 3$ give three equations containing the two Lagrange multipliers. Two of these equations are used to determine λ_1 and λ_2. When these are substituted into the third, a condition is imposed among the ϕ_i, which may be written

$$C_3 = \frac{-(I_{01} C_1 + I_{02} C_2 + A_{12} C_1 C_2)}{I_{03} + A_{13} C_1 + A_{23} C_2 + A_{123} C_1 C_2} , \tag{16}$$

where

$$\begin{aligned} A_{13} &= I_{03} \beta_1 + I_{01} \beta_3 , \\ A_{23} &= I_{03} \beta_2 + I_{02} \beta_3' , \\ A_{12} &= I_{01} (\beta_2 + \eta_2) + I_{02} (\beta_1 + \eta_1) , \\ A_{123} &= I_{01} (\beta_2 \beta_3 + \eta_2 \beta_3') \\ &\quad + I_{02} (\eta_1 \beta_3 + \beta_1 \beta_3') + I_{03} (\beta_1 \beta_2 - \eta_1 \eta_2) , \\ \beta_1 &= (L_1 + L_1' + \alpha_1 L_a) I_{01} / \bar{\Phi} , \\ \beta_2 &= (L_2 + L_2' + \alpha_2 L_b) I_{02} / \bar{\Phi} , \\ \beta_3 &= \alpha_1 (L_2'' + L_b) I_{03} / \bar{\Phi} , \\ \beta_3' &= \alpha_2 (L_1'' + L_a) I_{03} / \bar{\Phi} , \\ \eta_1 &= (M + \alpha_2 L_a) I_{01} / \bar{\Phi} , \\ \eta_2 &= (M + \alpha_1 L_b) I_{02} / \bar{\Phi} . \end{aligned}$$

Equations (14) and (15) impose another condition among the ϕ_i, which is found by eliminating I_c between them. At this point, we shall reduce the great generality of the above by imposing the restriction

$$L_a / L_b = L_1'' / L_2'' ,$$

which is a common design goal and which makes $\beta_3' = \beta_3$, and $\alpha_2 L_a = \alpha_1 L_b$. Combining Eqs. (14) and (15) then gives

$$\begin{aligned} (1 + F) B_3 &= B_2 + (N_2 \Phi_0 - \phi_{x2}) / \bar{\Phi} - E_1 \\ &\quad + F [B_1 - (N_1 \Phi_0 - \phi_{x1}) / \bar{\Phi} - E_2] \\ &\quad + (\alpha_2 - F \alpha_1) (N_f \Phi_0 - \phi_{xf}) / \bar{\Phi} , \end{aligned} \tag{17}$$

where

$$\begin{aligned} F &= [L_2' + \alpha_2 (L_a + L_b)] / [L_1' + \alpha_1 (L_a + L_b)] , \\ B_i &= \phi_i + \beta_i S_i , \\ E_i &= \eta_i S_i . \end{aligned} \tag{18}$$

The coupling factor F is the ratio of fluxes from the control current entering the two loops of the interferometer.

Our procedure, which is more direct and apparently simpler than those described by Landman[9] and Schulz-DuBois and Wolf,[11] is to choose ϕ_1 and ϕ_2, and determine C_3 from Eq. (16) and B_3 from Eq. (17). The values of C_3 and B_3 each specify a set of ϕ_3. Only certain pairs $\{\phi_1, \phi_2\}$ allow equality between members of these two sets. When the allowed ϕ_1, ϕ_2, and ϕ_3 are found, they are substituted into Eq. (1) and into Eq. (14), or Eq. (15), or the sum of the latter two, which is simpler:

$$\theta = B_2 + E_2 - B_1 - E_1 + 2\pi [N_1 + N_2 + (\alpha_1 + \alpha_2) N_f] , \tag{19}$$

where

$$\begin{aligned} \theta \equiv & [L_1' + L_2' + (\alpha_1 + \alpha_2) (L_a + L_b)] I_c / \bar{\Phi} \\ & + [\phi_{x1} + \phi_{x2} + (\alpha_1 + \alpha_2) \phi_{xf}] / \bar{\Phi} . \end{aligned} \tag{20}$$

Note that the coefficient of $I_c/\bar{\Phi}$ in Eq. (20) is the total inductance through which the control current passes, including that of the feed loop. If the control current were injected in the opposite side of the interferometer, as indicated by the dashed lines in Fig. 5, the coefficient of $I_c/\bar{\Phi}$ would be $L_1 + L_2$. None of the other formulas are affected. In the explicit flux term of Eq. (20), no assumptions concerning the apportionment of the flux from other sources among the separate loops is made; the coefficient of ϕ_{xf} results from the flux quantization condition in the feed loop.

When the control current is not injected into the interferometer, but lies above it, as is usually the case, one could drop the I_c term in Eq. (20) and treat the ϕ_{xi} as due to the control current, and stray flux if necessary. This requires a change in some of the terms in Eq. (17). The coupling factor F in Eq. (18) is the ratio of the coefficients of I_c in Eqs. (14) and (15). Dropping the I_c terms there requires taking the control current contributions ϕ^c_{xi} to the fluxes as proportional to each other. Thus, setting

$$\phi^c_{xf} = \alpha_f \phi^c_{x1} ,$$

$$\phi^c_{x2} = \alpha_{21} \phi^c_{x1} ,$$

casts F into the form

$$F = (\alpha_{21} + \alpha_f \alpha_2)/(1 + \alpha_f \alpha_1) , \tag{21}$$

of which Eq. (18) is a special case. The form of Eq. (17) remains intact if we take the ϕ_{xi} appearing there as possible stray fluxes. α_{21} and α_f are determined from the geometrical arrangement of control lines over the interferometer and feed loop.

The integers N_1 and N_2 are immaterial in determining the threshold curves if ϕ_1 and ϕ_2 are allowed to span an arbitrary range. That is, in both Eqs. (17) and (19), N_1 and N_2 appear only in the combinations $\phi_i \pm 2\pi N_i$. The same is not true for N_f, the number of flux quanta trapped in the feed loop. A changed value of N_f will not only translate the threshold curve along the I_c axis in an amount not generally equal to a multiple of 2π [in the units of Eq. (19)], but will also change the shape of the curve if $\alpha_2 \neq F\alpha_1$, as Eq. (17) shows. Stray flux will likewise both translate and change the shape of the curves.

We now make some specific observations about the threshold curves for three-junction interferometers.

(1) Although the set $\phi_1 = \phi_2 = \phi_3 = \pm \frac{1}{2}\pi$ satisfies Eq. (16), it is generally inconsistent with Eq. (17). Thus the maximum I_m is not the sum of the separate junction critical currents, except for special cases. Even for a symmetric interferometer ($I_{01} = I_{02} = I_0$, $L_a = L_b$, $L_1 = L_2$, $L'_1 = L'_2$, and $L''_1 = L''_2$), the sum of the individual critical currents will be realized only if

$$I_{03} L''_1 = 2I_0(L_1 + L'_1 - M) , \tag{22}$$

as deduced from Eq. (17), and provided there is no stray flux.

(2) Consider the symmetric interferometer with $I_{03} = 2I_0$, having negligible coupling M between loops, feed taps positioned such that each current path contains the same amount of inductance ($L''_1 = L_1 + L'_1$), and with no stray flux. This interferometer will have a maximum I_m of $4I_0$ when $N_2 = N_1$. For this case, one has $\beta_1 - \eta_1 = \beta_2 - \eta_2 = \beta_3 = \frac{1}{2}\beta$, where $\beta = LI_0/\bar{\Phi}$ and $L = L_1 + L'_1 + L''_1$ is the total inductance of one loop. This β thus has the same meaning as that of the symmetric two-junction interferometer. Equations (17) and (19) now are

$$2(\phi_3 + \beta_3 S_3) = \phi_2 + \phi_1 + \beta_3(S_2 + S_1) + 2\pi(N_2 - N_1) , \tag{23}$$

$$\theta = \phi_2 - \phi_1 + \beta'(S_2 - S_1) + 2\pi(N_1 + N_2 + 2\alpha_1 N_f) , \tag{24}$$

where $\beta' = \beta_1 + \eta_1$. These equations show that flux trapped in the feed loop translates the threshold curve along the I_c axis without distortion in this case. The maxima are separated by 4π in θ. For $N_f = 0$, θ is 2π midway between the first two maxima, which can happen only when $\phi_2 = \phi_1 + 2\pi$ according to Eq. (24). Then Eq. (16) becomes

$$C_3 = -C_1/(1 + \beta C_1) , \tag{25}$$

which is just the relation for a current-symmetric two-junction interferometer. This must be made consistent with Eq. (23) at $\phi_2 = \phi_1 + 2\pi$:

$$\phi_3 + \tfrac{1}{2}\beta S_3 = \pi + \phi_1 + \tfrac{1}{2}\beta S_1 . \tag{26}$$

What is important to note about these two equations, valid at the midpoints between major lobes, is that the feed loop inductance has dropped out. The threshold current at the mid-

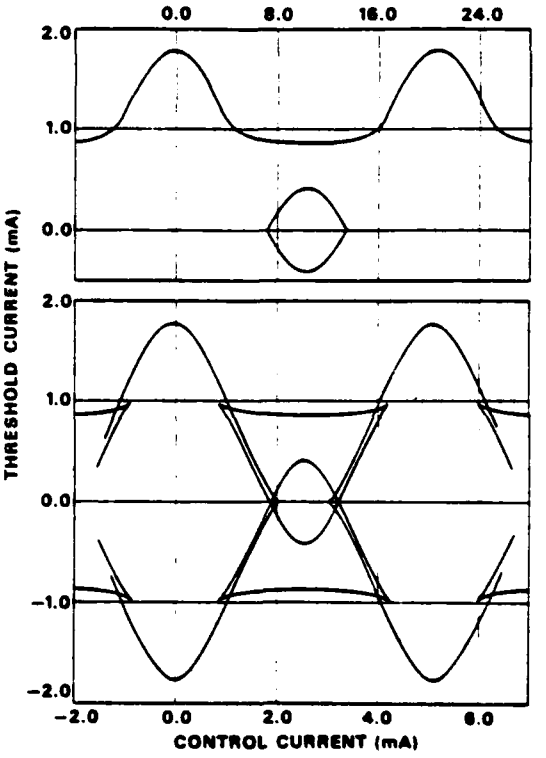

FIG. 6. Threshold curves for a symmetric three-junction interferometer with gate current injected close to the outside junctions (see Fig. 5). $L'_1 = L'_2 = 0.01$ pH, $L''_1 = L''_2 = 0.79$ pH, $L_1 = L_2 = 0$; $I_{01} = I_{02} = \frac{1}{2}I_{03} = 0.5$ mA. No stray flux, and $N_f = 0$. Lower graph: $L_a = L_b = 0.79$ pH. Upper graph (with reversed threshold current not shown): $L_a = L_b = 0.$ pH.

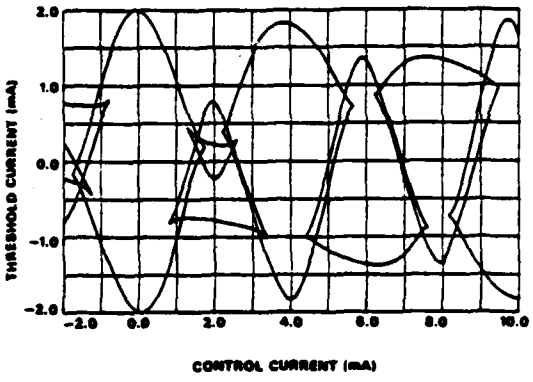

FIG. 7. Threshold curve for a three-junction interferometer having symmetric critical currents, but asymmetric inductances and fluxes, showing removal of lobe cusp ends from the axis, and a changing pattern. $I_{01} = I_{02} = \frac{1}{2}I_{03} = 0.5$ mA. $L_1' = L_1'' = L_a = 0.4$ pH; $L_2' = L_2'' = L_b = 0.3$ pH; $L_1 = L_2 = 0$; $N_f = 0$; no stray flux.

point thus provides a convenient measure of the loop inductance alone. The current ratio I_{mid}/I_{max} in fact is precisely that of the symmetric two-junction interferometer: Not only is Eq. (25) the same as the symmetric form of Eq. (5), but Eq. (26) is just the same as Eq. (7) with $\theta = \pi$, the midvalue for that case. Thus, Fig. 4 applies also to the symmetric three-junction interferometer as defined in this paragraph, and, we may speculate, would apply generally to the N-junction symmetric interferometer whose internal critical currents are twice those of the ends.

(3) If the feed arrangement for supplying gate current to the interferometer forms a superconducting loop, it is important to take the feed loop inductance into account. It is not just the control current scale which is affected, but also the shape of the threshold curve, since the β's are affected. Figure 6 illustrates a hypothetical case in which the gate current is injected close to the two outside junctions by means of a superconducting feed loop. For one curve the feed-loop inductance is made rather small, and for the other it is taken equal to the interferometer inductance. Not only is the control current scale much different for the two cases, but the connectedness of the threshold curves is also altered.

(4) In contrast to the two-junction case, the threshold pattern for the three-junction interferometer will have the lobe cusp ends removed from the $I_m = 0$ axis when inductances are asymmetric. This can be seen in Fig. 7, in which asymmetric inductances but symmetric critical currents are chosen. Of greater practical importance, however, is the fact that there is now a "long-range" change in the lobe pattern. This would ordinarily be undesirable in device operation. For example, a redistribution of trapped flux in the vicinity of the interferometer between runs could then drastically alter the shape of the threshold current near zero control current. Note that the maximum threshold current occurs at $I_c = 0$, and that there is point inversion symmetry about the origin.

(5) Figure 7 does not reveal an important point which has practical consequences, which is the fact that it is not the asymmetry in inductance, per se, which creates the long-range changing pattern, but rather the unequal amount of flux penetrating the two loops. This is seen in simulations, not shown here, in which the threshold curve is calculated for unequal inductances but equal fluxes through the two loops. (It would be unusual of course to realize such a situation experimentally.) The result is an identically repeating pattern of the same period as in symmetric cases. Thus, careful arrangement of control lines over the two loops of the interferometer is important in avoiding a lobe pattern which changes over many periods.

(6) Asymmetry of critical currents creates an asymmetry of the lobe pattern within a basic period, just as for the two-junction case.

V. COMPARISONS WITH EXPERIMENT

The usefulness of the foregoing observations is illustrated by considering some experimental data obtained from a three-junction interferometer fabricated in our laboratory,[15] and shown in Fig. 8. This device was fabricated with a nine-level vapor deposition process on an oxidized silicon substrate. The nine levels, in order of deposition are as follows: (1) 4000 -Å niobium ground plane; (2) 1200 -Å Nb_2O_5 formed by anodization; (3) 2000 -Å SiO dielectric; (4) 435-Å $AuIn_2$, 1 $\Omega/\square$, resistive intermetallic; (5) 3200 -Å lead-indium-gold base electrode alloy; (6) 3660 -Å SiO to define the junction windows; (7) 4000 -Å lead-gold alloy counterelectrode; (8) 7200 -Å SiO control line insulation; (9) 8000 -Å lead-indium-gold alloy control lines. Patterning was by etching for the ground plane and lift-off for the remaining eight levels. The interferometer occupies an area of $220 \times 70\ \mu$m and the minimum line width is $5\ \mu$m. The two interferometer loops are folded back on themselves so that the junctions are clustered in the center region.

The inductance of the various strips are given approximately by

$$L \simeq \mu_0 l(d + \lambda_1 + \lambda_2)/W, \tag{27}$$

where l is the strip length, d is the insulation thickness, and W is the strip width. Equation (27) is valid for $W > d$ and film

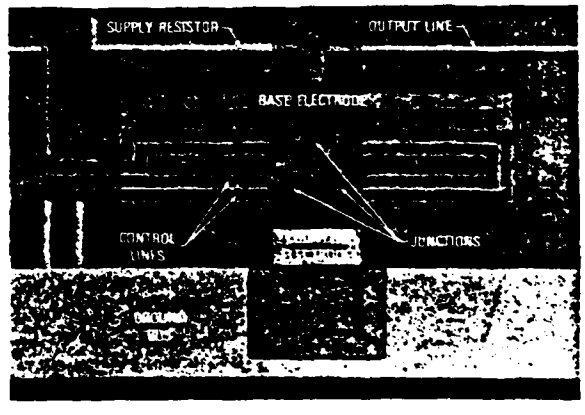

FIG. 8. Photograph of the type of three-junction interferometer whose threshold curves are depicted in Figs. 9 and 10. Note the very slight unequal coupling to the two halves of the interferometer because of the arrangement of the control line.

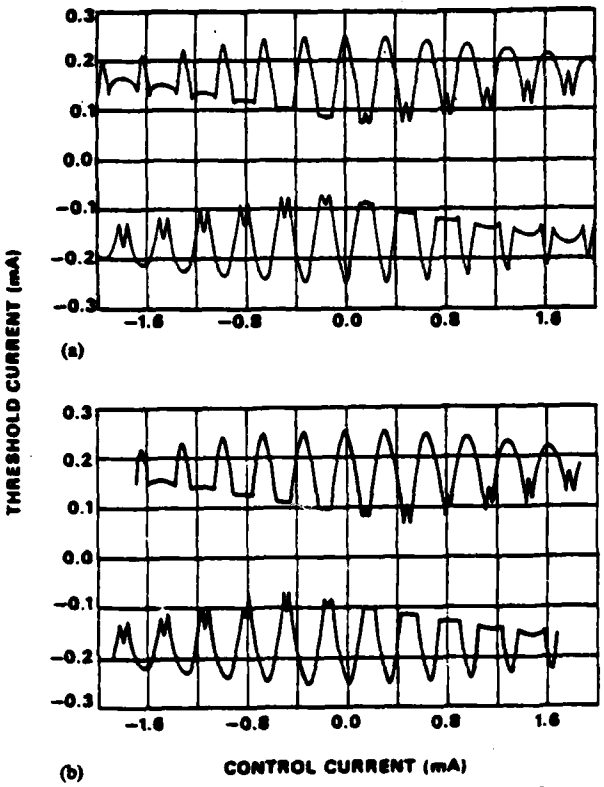

FIG. 9. (a) Experimental threshold curve for a three-junction interferometer of geometry shown in Fig. 8. The alignment of the highest maximum with zero control current shows that there was no flux trapped in the vicinity of the interferometer. (b) Result of simulation, with $L_1 = 1.14$, $L_1' = 3.48$, $L_1'' = 4.61$, $L_2 = 1.05$, $L_2' = 3.25$, $L_2'' = 4.30$, $L_e = 9.22$, $L_b = 8.60$ pH; $I_{n1} = I_{n2} = \frac{1}{2}I_{n3} = 63\ \mu$A; $N_f = 0$; no stray flux.

thicknesses much greater than their respective penetration depths λ_1 and λ_2. These conditions are only marginally satisfied for our interferometer. Two control lines overlie the interferometer loops. Figure 9(a) is a threshold curve obtained using the outer control line of this device. The essential symmetry within a period shows that the critical currents are quite symmetric and that the designed 1 : 2 : 1 ratio for critical currents has probably been achieved. The changing pattern on a long-range scale indicates that unequal fluxes are penetrating the two interferometer loops. This is probably a result of the asymmetry in the path of the control lines. The long-range pattern has a period of about 14 lobes, indicating an asymmetry on the order of 7%. (The long-range pattern repeats each time the difference in flux penetrating the two loops changes by Φ_0.)

Since the feed loop connects to the interferometer at the midpoint of each loop, we may assume that $L_1'' \cong L_1 + L_1' \cong L_2'' \cong L_2 + L_2'$, and $M \cong 0$. Thus Eq. (22) is satisfied and therefore $I_0 \cong \frac{1}{2}I_{max}$, or about 63 μA in the case of Fig. 9(a). Even though this interferometer is slightly asymmetric, the value of β can be estimated by measuring the ratio I_{mid}/I_{max}. I_{mid} is the current at the first midpoint on either side of I_{max}. The data of Fig. 9(a) together with Fig. 4 yield $\beta = 1.7$, and thus a single-loop inductance of

$$L = L_1 + L_1' + L_1'' = \beta\Phi_0/I_0 = 8.9\ \text{pH}.$$

The control current couples to $L_1' + L_2'$ and the parallel combination of $L_1'' + L_2''$ and $L_e + L_b$, as seen in Eq. (20). The product of this coupling inductance with the basic period ΔI_c for a symmetric interferometer is $2\Phi_0$. Taking this period from Fig. 9(a), one finds

$$L_1' + L_1''L_e/(L_1'' + L_e) = \Phi_0/\Delta I_c = 6.3\ \text{pH}.$$

One additional assumption is necessary to uniquely determine all of the L values. Since the inductance of a stripline is proportional to its length/width ratio [see Eq. (27)], we can estimate from the geometry of Fig. 8 that $L_1 + L_1' + L_1'' \cong L_e$. Combining these results, we obtain the inductances

$$L_1 = 1.1, \quad L_1' = 3.4, \quad L_1'' = 4.5, \quad L_e = 8.9\ \text{pH}.$$

Our control line geometry suggests that the 7% asymmetry is a result of asymmetric coupling to the interferometer, rather than unequal inductances. Simulation experience has shown, however, that for asymmetries as small as this, it makes very little difference whether one chooses in the model symmetric inductances and unequal coupling [using Eq. (21)], or simply makes the inductances asymmetric. For the theoretical curve of Fig. 9(b), we chose to use the control current form of Eqs. (17)–(20), and achieved the coupling asymmetry by increasing and decreasing the inductances by 3.5% on left and right, respectively. The resulting curve is quite a good representation of the data, both in shape and absolute scale. The calculated inductance values based on Eq. (27) are about 30% higher than the values given above. A fringing-field correction lowers the calculated value by about 10%. This is reasonable agreement in view of the uncertainty of the inductance calculation at the corners, and in particular, uncertainties in the values of λ_1, λ_2, and the insulation thickness d ($\sim$25%).

Often the maximum of threshold current does not coincide with the zero of control current, thus indicating the presence of flux trapped nearby. In another experimental

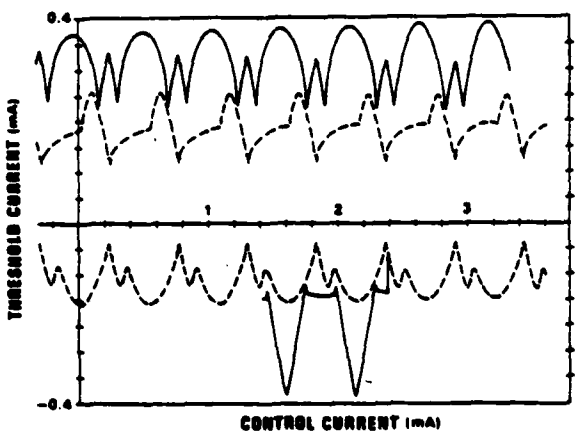

FIG. 10. Experimental threshold curves for a three-junction interferometer, showing the effects of unequal coupling as well as nearby trapped flux. An electrical disturbance caused a sudden shift from the solid to the dashed pattern. The trapped flux was redistributed, causing an asymmetrical decrease in the junction critical currents.

run, shown in Fig. 10, the local maximum increased with increasing I_c near $I_c = 0$, suggesting that trapped flux was opposing that from the control current. Postulating values for the fluxes ϕ_{x1}, ϕ_{x2}, and ϕ_{xf} resulting from an uncertain distribution of trapped flux is not very practical because of the great variation possible. The feed loop, however, offers a convenient analytical tool for including the effects of trapped flux. We found that the nearby trapped flux was the equivalent of about 30 flux quanta in the feed loop in this case. This number is interesting because it is about the number which would be present in an area the size of the feed loop, from the ambient flux pollution field in the Dewar. Using a procedure similar to that described in the preceding paragraphs, we deduced critical currents and inductances and achieved a very satisfactory match to the experimental curve, both in shape and scale.

In this particular run, the curve shifted abruptly from the solid curve to the dashed curve in Fig. 10, coincident with an electrical distrubtance in the room. The reduced maxima and the asymmetry within a basic period show that at least one of the junction critical currents has been reduced. The decreasing local maxima with increasing I_c near $I_c = 0$ suggests that now the trapped flux is penetrating the interferometer from the opposite direction. We found that changing the junction I_{0i}'s from the previous 0.10, 0.20, and 0.10 mA to 0.06, 0.11, and 0.10 mA, and taking $N_f = -25$, along with the previous inductances, satisfactorily reproduced the new curves. Apparently the electrical disturbance had rearranged the nearby trapped flux and had even caused some to lodge in the junctions themselves even though the junctions were "small" ($3\mu m \times 3\mu m$). Thus even an unusual situation has been found amenable to accurate simulation.

Trapped flux in these devices can thus be a considerable problem. Unless care is taken to cool the device in a very small field, the shift caused by trapped flux can result in radical variations in the threshold curve near the origin. To obtain a number of trapped flux quanta less than unity for devices such as that in Fig. 8, one requires a field less than about 10^{-7} T (1 mG).

It is sometimes desirable to control the lobe spacing of the threshold curve by varying the path of the control line which passes over the interferometer loops.[16] The lobe spacing may be made arbitrarily large simply by reducing the length of control line passing over the interferometer line. When doing this it is important to note that, because of the shunting effect of the feed loop, an interferometer such as that in Fig. 8 is less sensitive to control current across the upper half of its loops than to control current across the lower half.

VI. SUMMARY

Threshold curves for superconducting interferometers can be calculated on the basis of a fairly simple theory since only the $I_0 \sin\phi$ term is needed for characterizing the Josephson junctions; details of the quasiparticle curve, resistances, and capacitance are immaterial since a voltage is not developed. Feed-loop parameters and flux quantization within the feed loop are important and have been included in the present analysis. Experimental curves can be reproduced in detail, even for highly asymmetric cases as well as for very slightly asymmetric cases. The effects of flux trapping can be calculated. A "calibration curve" applicable to both two- and three-junction symmetric interferometers provides a rapid means for deducing interferometer inductance. An approximate simple analytical expression for this curve is given.

ACKNOWLEDGMENTS

We wish to thank R.E. Harris for helpful discussions throughout the course of this work, and F. Lloyd and L.O. Mullen for fabrication of the experimental devices.

[1] J.E. Zimmerman and A.H. Silver, Phys. Rev. 141, 367 (1966).
[2] J. Clarke, Philos. Mag. 13, 115 (1966).
[3] A. Th. A.M. De Waele and R. De Bruyn Ouboter, Physica 41, 225 (1969); 42, 626 (1969); *Progress in Low Temperature Physics*, edited by C.J. Gorter (North-Holland, Amsterdam, 1970), Vol. 6, p. 243.
[4] T.A. Fulton, Solid State Commun. 8, 1353 (1970).
[5] T.A. Fulton, L.N. Dunkleberger, and R.C. Dynes, Phys. Rev. B 6, 855 (1972).
[6] J. Clarke and J.P. Paterson, Appl. Phys. Lett. 19, 469 (1971).
[7] D.L. Stuehm and C.W. Wilmsen, Appl. Phys. Lett. 20, 456 (1972).
[8] Won-Tien Tsang and T. Van Duzer, J. Appl. Phys. 46, 4573 (1975).
[9] B.S. Landman, IEEE Trans. Magn. MAG-13, 871 (1977).
[10] H. Beha, Electron. Lett. 13, 218 (1977).
[11] E.O. Schulz-DuBois and P. Wolf, Appl. Phys. 16, 317 (1978).
[12] W.H. Henkels, Appl. Phys. Lett. 32, 829 (1978).
[13] H.H. Zappe and B.S. Landman, J. Appl. Phys. 49, 4149 (1978).
[14] L.M. Geppert, J.H. Greiner, D.J. Herrell, and S. Klepner, IEEE Trans. Magn. MAG-15, 412 (1979).
[15] This device is similar to one described in Ref. 14.
[16] R.E. Harris, C.A. Hamilton, and F.L. Lloyd, Appl. Phys. Lett. 35, 720 (1979).

APPENDIX C

Analog-to-digital conversion with a SQUID: Conditions for a countable pulse train

Robert L. Peterson

Electromagnetic Technology Division, National Bureau of Standards, Boulder, Colorado 80303
(Received 29 August 1978; accepted for publication 16 December 1978)

A superconducting loop containing a Josephson junction develops voltage pulses when it admits and expels magnetic flux quanta, and thus may be used as an A/D converter. We here develop and discuss several conditions which must be satisfied for the generation by the SQUID of an unambiguously countable pulse train, from which the analog signal can be faithfully reconstructed. These conditions can be satisfied over a broad range of realizable values of inductance and resistance. The capacitance, however, must be carefully controlled. The results of simulations are also presented, illustrating the various ways in which the pulse trains are affected.

PACS numbers: 74.50. + r

I. INTRODUCTION

A superconducting loop containing a Josephson junction—a single-junction SQUID (SJ-SQUID)—will admit or expel magnetic flux in quantized units with concurrent development of voltage pulses. These pulses may be of picosecond width at the junction. Figure 1(a) shows one possible arrangement of such a SQUID circuit. That this behavior might be used for the conversion of a fast analog signal to a digital one has doubtless occurred to many workers in the field. A patent based on the concept has recently been granted,[1] following a technical disclosure.[2] Hurrell and Silver[3] have considered a scheme in which the pulses from a SJ-SQUID are counted by means of a linear array of coupled double-junction SQUID's.

However, there are many conditions which must be met before this idea can be realized. The purpose of this paper is to examine in detail those conditions necessary for the production of a train of well-resolved pulses, free from the distortions which prevent faithful reconstruction of the analog signal. We also present the results of some simulations illustrating the various effects. Our conclusion is that such a device can be made to work, in the sense that the SQUID parameters (R,L,C) can be chosen to meet all the conditions simultaneously. A wide range for R and L are possible, but C must be carefully controlled.

Other A/D converter designs utilizing the Josephson effect could be somewhat faster. One can readily imagine a network of sampling circuits operating in parallel, each circuit containing a Josephson junction sensitive at a different threshold. The SQUID A/D converter discussed here produced pulses sequentially, which then must be processed serially. However, the inherent simplicity and great linearity of a SQUID A/D converter makes it appealing for use in cases where ultimate speed is not required. Even so, it should be faster than any existing A/D converter.

The SQUID model we shall analyze is shown in Fig. 1(b), in which the analog signal is an external current $I_x(t)$ applied directly to the loop. The three elements on the right comprise the Josephson junction with shunt capacitance C and phase-dependent conductance $G(\phi)$. The superconducting phase difference ϕ across the junction is related to the junction voltage $V(t)$ by

$$V = \left(\frac{\Phi_0}{2\pi}\right)\frac{d\phi}{dt}, \tag{1}$$

where $\Phi_0 = 2.068\times10^{-15}$ V s is the flux quantum. The current $I(t)$ where indicated in Fig. 1(b) was first derived by Josephson[4] as

$$I = I_0 \sin\phi + G(\phi)\ V, \tag{2}$$

where

$$G(\phi) = G_0 + G_1\cos\phi. \tag{3}$$

Here I_0 is the junction critical current, $G_0 \equiv 1/R$ is the normal-state junction conductance, and $G_1 V\cos\phi$ is often referred to as the $\cos\phi$ term, or the interference term between

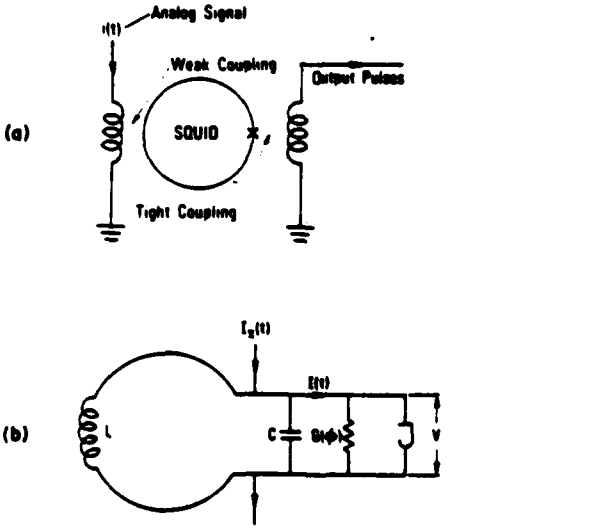

FIG. 1. (a) Schematic of one arrangement for generating pulses in a SQUID. (b) Elements of the SQUID analyzed in this paper.

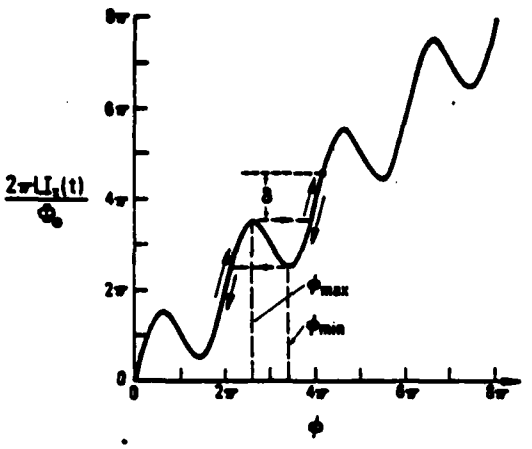

FIG. 2. Graphical solution of Eq. (8) for $\beta = 3$ showing hysteresis and a window uncertainty factor δ.

the supercurrent and the quasiparticle current G_0V. It is conventional in analyzing SQUID behavior to use Eq. (2) but to ignore the $\cos\phi$ term, and to treat I_0 and G_0 as constants.

We begin by considering only the loop inductance L together with the junction supercurrent since the basic ideas of pulse production and spacing are contained therein. Resistance and capacitance are then inserted and their effects analyzed. Finally, we discuss the effects of the $\cos\phi$ term and the voltage dependence of the coefficients. In Appendix A we provide some of the details for estimating the pulse widths when inductance is important, and in Appendix B we discuss the factors affecting the linearity of a SQUID A/D converter.

Once a satisfactory sequence of pulses is produced, the next step in building a converter is to use the pulses to activate a counter or shift register, which is then sampled.[3] It is beyond the scope of this paper to discuss these devices, which would themselves be circuits containing Josephson junctions. Likewise, the various techniques and algorithms which might be used for reconstructing the signal will not be discussed in much detail in this paper, although we do give two simple examples.

II. CONDITIONS FOR ADEQUATE PULSES

The differential equation appropriate to Fig. 1(b), but without the $\cos\phi$ term, is

$$LC\frac{d^2\phi}{dt^2} + \frac{L}{R}\frac{d\phi}{dt} + \theta = \phi_x(t), \tag{4}$$

where

$$\theta = \phi + \beta\sin\phi, \tag{5}$$

$$\phi_x(t) = 2\pi LI_x(t)/\Phi_0, \tag{6}$$

$$\beta = 2\pi LI_0/\Phi_0. \tag{7}$$

The essential aspects of pulse production may be deduced by considering just the inductive, supercurrent, and driving terms of Eq. (4), i.e.,

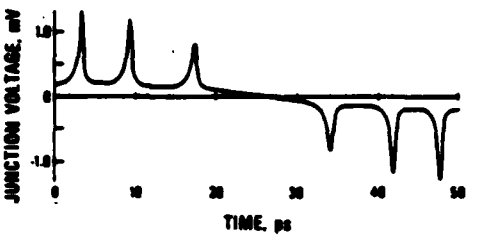

FIG. 3. Pulses from a nonhysteretic SQUID, driven by a sinusoidal current of amplitude $I_1 = 2.0$ mA and frequency 10 GHz. $I_0 = 0.1$ mA, $R = 20\ \Omega$, and $L = 3$ pH. These give $\beta = 0.91$. The response to a half-cycle is shown.

$$\theta = \phi_x(t). \tag{8}$$

Equation (8) is readily solved graphically, as shown in Fig. 2 for $\beta = 3$. Let ϕ_0 be the principal value of $\cos^{-1}(-1/\beta)$, lying between $\frac{1}{2}\pi$ and π. As the current I_x is increased, ϕ increases and at values

$$\phi_{max}^{(n)} = \phi_0 + 2\pi n, \quad n = 0,1,2,\cdots, \tag{9}$$

jumps discontinuously to a higher value. When R or C are included, this jump is not discontinuous. The jumps in ϕ correspond to voltage pulses, and the entry of flux quanta, according to Eq. (1). When the signal decreases, the jumps in ϕ initiate at

$$\phi_{min}^{(n)} = 2\pi - \phi_0 + 2\pi n, \quad n = 0,1,2,\cdots. \tag{10}$$

The voltage pulses are of reversed polarity. The hysteretic effect seen in Fig. 2 causes an abnormal spacing between *pulses of opposite polarity*.

When $\beta < 1$, there are no extrema in the I_x-vs-ϕ plot. Nevertheless, $d\phi/dt$ is highest when the slope is smallest (at $\phi = \pi, 3\pi,\cdots$), and the voltage will tend to develop pulses. These pulses in fact can be quite respectable, as Fig. 3 shows

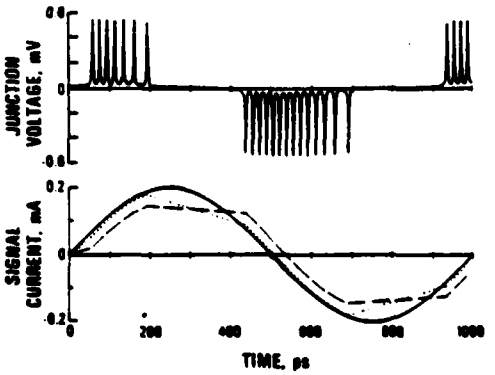

FIG. 4. Top: Pulses from a very hysteretic SQUID, driven by a sinusoidal current of amplitude $I_1 = 0.2$ mA and frequency 1 GHz. $I_0 = 0.05$ mA, $R = 5\ \Omega$, and $L = 100$ pH, giving $\beta = 15.2$. Bottom: The driving current together with two reconstructed signals based on the counting of the SQUID pulses. The dashed "curve" is constructed by adding or subtracting a current Φ_0/L at each pulse, depending on its polarity. The dotted "curve" includes hysteretic corrections as discussed in the text. The dotted and dashed "curves" are drawn so as to connect the leading edges of each step corresponding to a pulse count. The steps are not shown, to avoid cluttering.

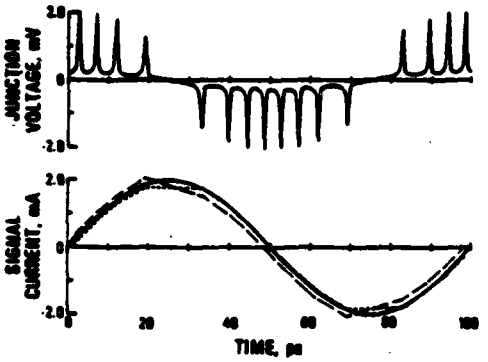

FIG. 5. Top: Pulses from a SQUID with very small hysteresis, driven by a sinusoidal current of amplitude $I_1 = 2.0$ mA and frequency 10 GHz. $I_0 = 0.1$ mA, $R = 20\ \Omega$, and $L = 4$ pH, giving $\beta = 1.21$. Bottom: The driving current and two reconstructed signals with the same meanings as in Fig. 4.

for $\beta = 0.91$. However, the pulse heights and widths are rather sensitive to the rate of change of $I_x(t)$, which would likely be undesirable. On the other hand, $\beta > 1$ introduces the hysteretic effect mentioned above. A rather extreme case is shown in the top half of Fig. 4, together with the badly distorted reconstructed signal in the bottom half of the figure. Clearly, large β should be avoided.

Figures 3 and 4 also show what is generally true: there is no cumulative gain or loss of pulses during successive sign changes of dI_x/dt.

Pulse spacing, signal reversal effects, and "baseline" variation can also be obtained from Eq. (8), as follows.

For a linearly rising singal, $I_x(t) = I_1\omega t$, the times of occurrence of the voltage pulses are, from Eqs. (8) and (9),

$$t_n = \frac{\Phi_0}{2\pi L I_1 \omega}(\theta_0 + 2\pi n), \qquad n = 0,1,2,\cdots, \tag{11}$$

where

$$\theta_0 = \phi_0 + (\beta^2 - 1)^{1/2}. \tag{12}$$

The separation between pulse centers is thus

$$\Delta t = \Phi_0/LI_1\omega. \tag{13}$$

To maintain a given separation, fast signals thus require small SQUID area or small or attenuated signal amplitude I_1. Pulse separation is compared to pulse width below, where resistance is introduced.

When the continuous signal reverses, i.e., when dI_x/dt changes sign, the spacing between pulses is "abnormal" both because of the hysteretic effect mentioned above and the "window quantization" effect, common to all digitization schemes, in which it is uncertain just where within a window the turnaround has taken place. (Of course, since no signal turnaround is instantaneous, the pulse spacing will also increase as dI_x/dt decreases). It is of interest to compare window quantization and SQUID hysteresis in their effects upon the spacing between reversed pulses. This is easily obtained in the present case where we are not yet considering R and C. For a signal rising linearly, stopping suddenly, and then falling at the same rate, one gets using Eqs. (9) and (10)

$$t_{rev} = \Delta t\left(\frac{\theta_0}{\pi} - 1 + \frac{\delta}{\pi}\right), \tag{14}$$

where Δt is the normal pulse spacing given by Eq. (13), and θ_0 is given by Eq. (12). The term δ/π is the window quantization factor, and the remainder is due to hysteresis. The hysteretic factor is zero at $\beta = 1$, and about equal to β for $\beta \gg 1$. The value of δ is uncertain, by definition, within the range 0 to 2π. Thus the hysteretic effect dominates the window quantization only for β larger than, say, 4.

The hysteretic effect on pulse spacing can be compensated in part during signal reconstruction by appropriately weighting the first reversed pulse in each signal reversal. Figure 4 shows a calculated response to a sinusoidal signal, in which there is large hysteresis ($\beta \simeq 15$). The lower half of Fig. 4 shows the associated input signal together with two methods for restructuring the signal from the pulses. The "naive" method simply adds or subtracts a constant current increment Φ_0/L for each detected pulse. The other method notes that the current at the first pulse is $(\Phi_0/L)(\theta_0/2\pi)$, according to Eq. (8), and that the current drop between reversed pulses is $(\Phi_0/L)(\theta_0/\pi) - 1$. Figure 5 shows another pulse train and reconstructed signals at $\beta \simeq 1$. Figures 4 and 5 illustrate the fidelity with which signals can be digitized and reproduced, assuming perfect counting. Note that in Fig. 5, the pulse number can be increased considerably without detriment, e.g., by increasing I_1.

Even for well-separated pulses, the voltage does not return to zero between pulses, as Figs. 3–5 show. The reason is discovered from Eq. (8) by setting $\phi = 2\pi n + \delta\phi$, and letting $|\delta\phi| \ll 1$ in order to examine the situation between pulses (refer to Fig. 2). By taking the time derivative of Eq. (8) and using the voltage relation (1), one gets for the voltage between pulses

$$V_B(t) = L_1 \frac{dI_x}{dt}, \tag{15}$$

where

$$L_1 = L/(1 + \beta). \tag{16}$$

L_1 is the loop inductance reduced by the junction parametric inductance factor $1 + \beta$, and appears frequently in the subsequent analysis. From the equations incorporating resistance and capacitance, one can show that the presence of resistance subtracts approximately the term

$$\frac{L_1^2}{R}\frac{d^2I_x}{dt^2},$$

from the right-hand side of Eq. (15). Capacitance subtracts another

$$L_1^2 C \frac{d^3I_x}{dt^3}.$$

In the linearly rising or falling portions of the signal, the latter two make no contribution, whereas in the turn-around portions, they are the most important.

The reason for concern about baseline variation is that

if a pulse discriminator has a constant threshold level, that level must be set above the maximum baseline voltage; if this maximum is high, then pulses occurring when the baseline voltage is low might be missed. However, there are two reasons for expecting that baseline variation should not be a substantial problem. First, an expression for V_{max}, the maximum voltage of a pulse, may be obtained from $V_{max}\tau' \simeq \Phi_0$, where τ' is a measure of the pulse width. For well resolved pulses, $\tau' \lesssim \Delta t/M$, where M is, say, 4 or 5. Noting the relationship between Δt and V_B, given by Eqs. (13) and (15), one thus gets

$$V_{max} \gtrsim M(1+\beta)V_B. \tag{17}$$

Thus for well-separated pulses, the pulse height will be several times greater than the baseline voltage during the linear portions of the signal. Similar arguments can be used for the changing parts of the signal, with similar conclusions. This, of course, does not guarantee that a given pulse height will be greater than the maximum baseline voltage. Of more importance is the fact that it should be possible to design the discriminator level to vary according to $V_B(t)$, or to filter out that background on the basis of frequency in the circuitry following the SQUID.

A junction with finite resistance R is known[7] to switch in and out of its voltage state, when driven with a current larger than I_0, in the time

$$\tau_0 = \Phi_0/\pi R I_0. \tag{18}$$

This is the voltage pulse width at half-height. We wish to determine now by how much this pulse width is affected by the presence of the SQUID inductance L. By consulting Fig. 2 and Eq. (4) without the capacitance term, we see that the state of the system, represented by a "particle" riding on the θ curve, does now not simply follow $I_x(t)$, but lags by an amount $(L/R)(d\phi/dt)$. Thus, discontinuous jumps in ϕ dc not occur; rather the particle makes a fast ride through the local valleys. This "inertial" effect can also be manifested in the appearance of a final positive pulse just after an increasing signal has started back down.

Good pulse resolution requires that the pulse width τ be much less than pulse spacing Δt. The finite resistance now being considered will not alter pulse spacing; i.e., when the transients are finished, the "steady-state" response to a linearly increasing signal must be a series of pulses with the same periodicity as when the resistance is infinite. Thus Eq. (13) for the spacing Δt is still valid.

The effect of loop inductance on pulse width is not simple to analyze. An approximation is developed in Appendix A. The expressions obtained there do not yield a simple formula for τ except at $\beta \gg 1$. However, when $\beta \gtrsim 1.5$, τ and τ_0 are not so different that we cannot replace τ by τ_0 in the pulse resolution condition. The simulations show that $\Delta t = 4\tau_0$ is about the minimum condition for adequate resolution. Thus from Eqs. (13) and (18), we arrive at

$$L/R \lesssim I_0/8fI_1 \tag{19}$$

as a reasonable condition for satisfactory pulse resolution, where $f = \omega/2\pi$.

Figures 3–5 are representative of simulations of SQUID behavior when junction (or shunt) resistance R is included, but capacitance is not. Figure 3 shows well separated well-developed pulses from a nonhysteretic SQUID ($\beta \simeq 0.9$). The parameter values are given in the figure caption. Equation (19) is well satisfied, and all pulses are well above the maximum value of V_B. The measured $1/e$ width of 0.80–0.85 ps for the first pulse (i.e., in the region of a linearly rising signal) is more than a factor of 2 greater than the simple junction τ_0, but close to the τ as calculated from Eqs. (A1)–(A4). The third and fourth pulses, occurring when the signal is changing more slowly, are noticeably broader, as expected for a nonhysteretic SQUID.

In the very hysteretic SQUID ($\beta \simeq 15$) of Fig. 4, the pulses are well developed and Eq. (19) is just satisfied. The long delay between pulses of opposite polarity shows principally the effects of the great hysteresis. Pulse heights here are far above V_B, and pulse broadening as the signal slows is not discernible. Now τ_0 and τ are about equal, and close to the measured width.

Figure 5 shows the response of a slightly hysteretic SQUID ($\beta \simeq 1.2$). Only the inductance is changed from Fig. 3. The inductance increase by one-third results in a pulse width decrease by one-third. A slight broadening of the pulses in the signal slow-down regions can be seen.

Good pulse trains of course also occur in quite different regimes of operation. For example, simulations for a rather typical shunted point-contact SQUID ($L = 500$ pH, $R = 100\ \mu\Omega$, $I_0 = 1\ \mu$A) driven at 1 kHz show good pulses. However, the very low peak voltages ($\simeq 10^{-16}$ V) for such a case would make pulse detection perhaps impossibly difficult because of noise.

Capacitance is the bad actor in pulse production from SQUID's and must be kept as small as possible, consistent with an adequate current I_0. The main effects of capacitance can be understood qualitatively by the device of rewriting Eq. (4) in the form of an energy equation, in which a particle can be pictured as sliding along a time-dependent potential well, and restricted by viscous damping. Thus, Eq. (4) is equivalent to

$$\dot{\mathscr{T}} + \dot{\mathscr{V}} = -D\dot{\phi}^2 - (\phi - \phi_x)\dot{\phi}_x, \tag{20}$$

where the dot over a symbol refers to differentiation with respect to $t_1 \equiv t/(LC)^{1/2}$. Here $D = (LC)^{1/2}/RC$, $\mathscr{T} = \frac{1}{2}\dot{\phi}^2$, and

$$\mathscr{V} = \tfrac{1}{2}(\phi - \phi_x)^2 - \beta\cos\phi. \tag{21}$$

The "potential" $\mathscr{V}$ is a parabola centered at ϕ_x, with local minima which become progressively shallower, and finally disappear, as one moves farther up the sides of the parabola.[4] As I_x is increased, a particle once displaced from its vanished minimum drops into the adjacent well, and if the damping constant D is large enough, becomes trapped in that well, and oscillates about the minimum before coming to rest. Each new local minimum entered corresponds to the generation of a voltage pulse, and the oscillations within a local minimum are the plasma oscillations. In the present case, I_x does not generally change slowly, and the pulse

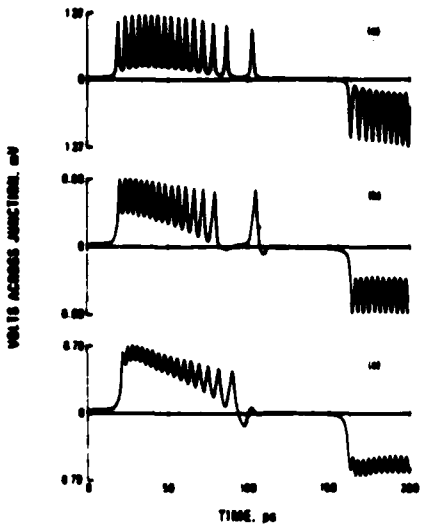

FIG. 6. An 80-pH SQUID driven at 2.5 GHz, with $I_0 = 0.1$ mA, $I_1 = 0.5$ mA, and $R = 5\,\Omega$. (a) $C = 0$; (b) $C = 0.2$ pF; (c) $C = 0.5$ pF. The sequence illustrates the appearance of an extra pulse (c) when the capacitance is large enough that the damping is less than threshold damping for single fluxoid entry. Equation (25) is not satisfied in the middle and bottom curves.

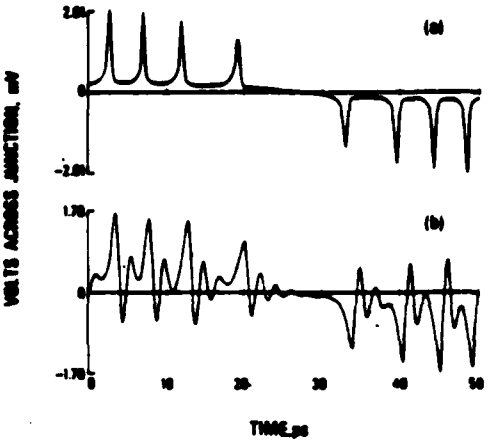

FIG. 7. A 4-pH SQUID driven at 10 GHz, with $I_0 = 0.1$ mA, $I_1 = 2.0$ mA, and $R = 20\,\Omega$. (a) $C = 0$; (b) $C = 0.05$ pF. The plasma oscillations in the latter case produces an unacceptable pulse train, and Eq. (25) is not satisfied.

characteristics are determined also by the rate of change of I_x as well as by the values of D and β, as Eq. (20) shows.

If the damping D is too small (capacitance too large), at least three undesirable things can happen. One, the plasma oscillations may be of such large amplitude that they could be counted as pulses. Second, if the ringing does not damp out soon enough, it can interfere with the effect of the changing potential, causing the particle to move too soon or too late into the next local minimum. Third, even for a very slowly changing signal, if D is smaller than a threshold value D_1, the particle might move rapidly through more than one minimum, producing pulses in groups. If the signal at a given time is fast enough to prevent this, extra pulses can still appear as the signal slows. All these effects have been seen in the simulations. Obviously, any of them could produce a digitized signal so distorted that the result may be worthless.

The damping threshold D_1 mentioned above is the condition for single-pulse (as opposed to multiple) generation as the signal is very slowly increased through a value which gives a pulse. The formula

$$D_1 = 1.193\beta^{1/2} - 2.530 \qquad (22)$$

has been shown[4] to be quite accurate for β above about 4.6 and is certainly accurate enough for SQUID A/D conversion considerations. When the signal changes rapidly, the threshold between single and multiple quantum transitions becomes blurred, however.

Figures 6(a)–6(c) illustrate an effect when $D < D_1$. Here an 80-pH SQUID is driven at 2.5 GHz. Figure 6(a) for $C = 0$ shows an acceptable pulse train even though pulse spacing is perhaps not large enough. At $C = 0.2$ pF in Fig. 6(b), the pulses are still regularly spaced, although resolution may now be a problem. Note that the sixteenth pulse in Figs. 6(a) and 6(b) actually occurs after the signal has started to decrease. This is common in the simulations and illustrates the "inertial" effect mentioned earlier. The damping D is 4.0 in Fig. 6(b), larger than the threshold D_1 of 3.3 Figure 6(c) at $C = 0.5$ pF shows a still worse train, but of interest here is the fact that there are now 17 pulses (and the seventeenth occurs before signal reversal). This is because now $D = 2.5$, less than D_1.

Figures 7(a) and 7(b) illustrate plasma oscillation effects in a 4-pH SQUID driven at 10 GHz. Figure 7(a) shows a clean train of pulses at $C = 0$. However, when C is increased to just 0.05 pF in Fig. 7(b), large-amplitude plasma oscillations appear. Note that the pulse spacing is relatively

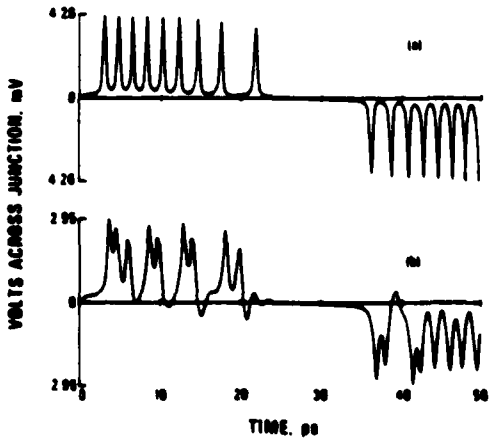

FIG. 8. A 10-pH SQUID driven at 10 GHz, with $I_0 = 0.1$ mA, $I_1 = 2.0$ mA, and $R = 10\,\Omega$. (a) $C = 0$; (b) $C = 0.05$ pF. Curve (b) shows an unacceptable case of "ringing interference" with the analog signal. Equation (25) is not satisfied in (b).

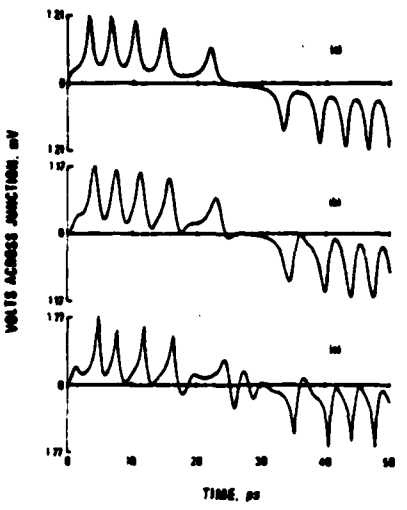

FIG. 9 A 5-pH SQUID driven at 10 GHz, with $I_0 = 0.1$ mA, $I_1 = 2.0$ mA, and $R = 5\ \Omega$. (a) $C = 0$; (b) $C = 0.1$ pF; (c) same as middle graph, but with $\cos\phi$ term included, assuming $G_1 = -G_0$. Equation (25) is satisfied in each case.

unchanged, but that there would now be a problem of how to avoid counting the larger of the plasma oscillations as pulses.

Figures 8(a) and 8(b) illustrate the "ringing interference" mentioned above, with a 10-pF SQUID responding to a 10-GHz signal. At $C = 0$, Fig. 8(a), a good pulse train appears, but at $C = 0.05$ pF, Fig. 8(b), an intolerable situation has already developed. The pulses are now irregularly spaced because of the ringing interference between the plasma oscillations and the signal motion.

Figures 9(a)–9(c) show a case in which a 5-pH SQUID driven at 10 GHz has a fair pulse train at $C = 0$, Fig. 9(a), which is not materially affected when a capacitance of 0.1 pF is introduced, Fig. 9(b). Figure 9(c) is addressed later in connection with the $\cos\phi$ term.

The conditions for maintaining a good pulse train in the presence of the inevitable capacitance are deduced as follows. Of principal interest are the plasma oscillation period and damping time. These may be analyzed by examining Eq. (4) near the midpoints between the pulses, at $\phi = 2\pi n + \delta\phi$, where $|\delta\phi| \ll 1$. The homogeneous solution to Eq. (4) linearized in $\delta\phi$ has the form $\exp(pt)$, where

$$p = -\frac{1}{2RC} \pm \frac{1}{2L_1C}\left[\left(\frac{L_1}{R}\right)^2 - 4L_1C\right]^{1/2}, \tag{23}$$

and the reduced inductance L_1 is defined in Eq. (16). When the radicand is negative, damped plasma oscillations occur, having the period

$$T_p = 4\pi L_1 C\,(4L_1C - L_1^2/R^2)^{-1/2} \tag{24}$$

and damping time $2RC$.

The various effects seen in Figs. 7–9 can be predicted from knowledge of the SQUID and junction parameters. First, let us dispose of two insufficient conditions for good pulse trains. If the pulse spacing Δt satisfied $\Delta t > 2RC$, there would be no ringing interference, and the pulses would maintain their correct spacing. However, this condition is too weak since it still allows the possibility that initial large-amplitude plasma oscillations may be counted as pulses. This could be avoided by requiring the plasma period to be long compared with Δt, so that succeeding pulses occur before the plasma oscillations have a chance to develop. But it is clear that this condition is also not sufficient; the signal must eventually slow and reverse, and the resulting increased pulse spacing would allow the plasma oscillation effects to occur again.

One way to avoid these problems is to require the "overdamped" condition, in which the radicand of Eq. (23) is positive: $L_1/R > 4RC$. Small R and C are thus desirable. However, modest underdamping can certainly be tolerated, as our simulations generally show. This may be quantified as follows. Noting that the falling side of a pulse is actually the first part of the plasma oscillation, we should require that $\frac{1}{2}T_p$—the approximate time at which the voltage has its least value—should be somewhat greater than the damping time $2RC$, in order that the oscillation amplitudes not be so large as to be possibly counted as pulses. Using $T_p \gtrsim \alpha(2RC)$ where α is somewhat larger than 2 for a minimal condition, we have with Eq. (24)

$$\frac{L_1}{R} > \frac{4\alpha^2}{4\pi^2 + \alpha^2} RC. \tag{25}$$

Simulations show that $\alpha = 3$ is about right. The coefficient of RC in Eq. (25) is then about $\frac{1}{2}$.

It may be necessary to use a shunt resistance to satisfy this condition. Let us consider an example which would appear to be fairly typical. Take $C = 0.3$ pF, an attainable value. For $I_0 = 0.2$ mA and $\Delta = 2$ mV, where Δ is the half-gap voltage, the normal-state junction resistance R_j would be about 16 Ω, according to $R_j I_0 = \frac{1}{2}\pi\Delta$. If the pulse voltage does not rise above about 2 mV, the actual junction resistance will be considerably greater than 16 Ω. Thus $RC \gtrsim 5$ ps, requiring $L_1 > 60$ pH to satisfy Eq. (25). But taking note of the definition of β, we see that $L_1 > 60$ pH cannot be satisfied for positive L. In fact, Eq. (25) demands a maximum value for R of about

$$R_{max} = (3\Phi_0/2\pi I_0 C)^{1/2}. \tag{26}$$

Figures 6–8 illustrate cases in which Eq. (25) is not satisfied, whereas in Fig. 9 it is satisfied.

To sum up, Eqs. (19) and (25) should be simultaneously satisfied for good pulse production from a SJ-SQUID.

III. OTHER EFFECTS

Equation (2) with conductance $G(\phi)$ given by Eq. (3) is derived[4] for constant voltage across the junction. So far we have ignored the $\cos\phi$ term and have treated $G_0 = 1/R$ and I_0 as constants, even though the derivation shows them to be voltage dependent. When one confronts a situation, as here, in which picosecond voltage pulses occur, whose peak values can reach or exceed the gap voltage, several questions arise. Will a nonequilibrium description of the superconductors be essential for a quantitative analysis? Should a time-depen-

dent microscopic formulation[7,8] (but still within an equilibrium theory) be used? Should the voltage dependence of the parameters I_0, G_0, and G_1 be used in the constant-voltage formulation? How important is the $\cos\phi$ term? We shall address questions in the order asked.

The nonequilibrium question is difficult to answer rigorously. As long as the superconductors are not driven far out of equilibrium (say with voltages exceeding the gap voltage), or if the equilibration times are shorter than the pulse widths when the voltage peaks *are* substantial, one would not expect a gross deviation from equilibrium-based computations. Since superconductor relaxation times are substantially less than picosecond times, and since the pulse peaks only rarely exceeded gap values in our simulations, we expect that nonequilibrium effects should not be serious in SQUID A/D conversion.

As for going to a time-dependent formulation, this is in fact what one should do for the best analysis within an equilibrium theory. Such an analysis, is, of course, much more expensive than the present one. We have already made comparisons between the microscopic[7] and phenomenological[3] theories in the context of examining the possibility of using tunnel junctions as picosecond pulsers and found no substantial differences in pulse configurations. Further, it has been observed for many years that the phenomenological, or resistively-shunted-junction, model is respectable in a wide variety of applications. The reason is probably somewhat as follows, and this also addresses the remaining questions asked above. The critical current I_0 varies only slightly with V for $V \ll \Delta$ and thus can be treated as a constant in A/D converter applications. A shunt conductance, which would probably be used, will usually dominate G_0. Since G_0 and G_1 are comparable in magnitude, the voltage dependence of both G_0 and G_1 is not then significant. The time-dependent formulation thus probably introduces changes only in detail.

Some effects of the $\cos\phi$ term, and a new way for measuring G_1 have been discussed in Ref. 6. It is, however, interesting to note the effect of the $\cos\phi$ term in the present context. One sees that its contribution to Eq. (20) is to multiply the damping coefficient D by the factor $1 + \epsilon\cos\phi$, where $\epsilon = G_1/G_0$. BCS theory applied to tunnel junctions states that $\epsilon \simeq +1$ for $V \ll \Delta$. Thus at $\phi = 2\pi n$, $n = 0,1,2\cdots$, which are the positions of the local minima in the "potential" $\mathcal{V}$, the effective damping is doubled; the bottoms of the wells are "stickier" and plasma oscillations would be less of a problem; that is, larger capacitance could be tolerated. However, if $\epsilon \simeq -1$, as it is in the theory of microbridges, and as several experiments on microbridges, point contacts, and tunnel junctions have suggested (see Ref. 6 for a fuller discussion and references), then the damping in the local wells would be very much smaller, and plasma oscillations would pose a more severe problem. We show an example of this in Fig. 9(c), in which the parameters are the same as in the middle curve, except that the $\cos\phi$ term with $\epsilon = -1$ is added. Although Eq. (25) is satisfied, this pulse train would probably not be acceptable. We repeat the caveat given above, that in the realm of rapid and large voltage changes, the constant-voltage formulation may not be quantitatively reliable.

However, we would also expect it to be not completely wrong. Thus, if it turns out that $\epsilon \simeq -1$ for tunnel junctions at $V \ll \Delta$, the avoidance of disruptive plasma oscillations may be very difficult unless a large shunt conductance is provided.

ACKNOWLEDGMENTS

I wish to thank D.B. Sullivan and N.V. Frederick for suggesting this problem, and several colleagues for useful discussions.

APPENDIX A

In this Appendix, we analyze the voltage pulse width for a junction with resistance but no capacitance, taking into account the loop inductance.

We consider a linearly rising signal $I_x = I_1\omega t$, as before. From Fig. 2 one can see that the pulses will be asymmetric. The voltage pulse "begins" when θ, defined in Eq. (5), ceases to rise linearly, and rises most rapidly when θ decreases most rapidly, at about $\theta = \pi, 3\pi, \cdots$. The pulse peaks near the minimum of θ then generally falls more rapidly than it rose. We can estimate the pulse width by replacing θ by a series of straight lines on a θ-vs-ϕ plot, with the lines passing through the points of greatest slope, and having the correct slopes $(1 \pm \beta)$ at those points. The solutions to the approximated Eq. (4) with $C = 0$ are then increasing or decreasing exponential functions. The decreasing part of the pulse is exponential with time constant

$$\tau_r = L_1/R, \tag{A1}$$

where L_1 is the reduced inductance of Eq. (16). The increasing exponential has a time constant $(L/R)(\beta - 1)^{-1}$, but this does not measure the "left" half pulse width. If we equate the voltage on the rising portion to the $1/e$ point on the falling side, we find

$$\tau_f = \frac{L}{R}\frac{1}{\beta - 1}(X - Y), \tag{A2}$$

where X and Y are solutions of

$$X + \frac{\pi\Phi_0 R}{I_1 f}\left(\frac{\beta - 1}{2\pi L}\right)^2 = \left(1 + \frac{\beta - 1}{\beta + 1}\right)(e^X - 1) \tag{A3}$$

and

$$e^Y = 1 + e^{-1}(e^X - 1). \tag{A4}$$

Many simulations have shown that the resulting computed pulse width $\tau = \tau_f + \tau_r$ is always a little smaller than the measured width at the $1/e$ level, averaging about 80% of the measured value. In fact, the simple expression for τ_0 in Eq. (18) is found to be good to within about 50% for $\beta \gtrsim 1.5$. For $\beta \lesssim 1.5$, we have found some cases in which τ_0 is in error by as much as a factor of 3. However, τ remains "good" at all β.

The pulse width τ according to the above formulas is thus dependent upon the signal rate, especially near $\beta = 1$, as one expects. When $\beta \gg 1$, $X - Y \simeq 1$, and

$$\tau \simeq 2L/\beta R = \tau_0. \tag{A5}$$

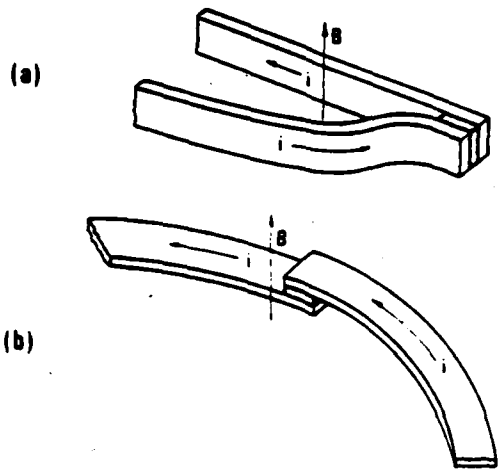

FIG. 10. Portions of two possible junction arrangements in SQUID's constructed by microfabrication techniques.

Thus, the very hysteretic SQUID develops voltage pulses comparable to those produced by the simple resistive junction,[3] whereas the nonhysteretic or only slightly hysteretic SQUID gives rate-dependent pulses.

APPENDIX B

Here we shall examine some factors affecting the linearity of the SQUID. As was seen in Sec. II, the two most important SQUID parameters are the inductance L of the loop and the critical current I_o of the junction. Both of these parameters can be changed by the signal being measured, producing a nonlinearity.

Typically, the magnetic field from the current in a nearby control line will be used to bring the critical current to some convenient operating point. The addition of a signal, whether as a magnetic field or as a current, will change the number of fluxoids in the loop, which in turn will change I_o if the associated magnetic induction B crosses the junction (see Fig. 10). We need to know by how much I_o changes for a given number of fluxoids entering the loop due to an increasing signal.

Consider a square tunnel junction of side W and thickness d. If $W \lesssim \lambda_J$, where λ_J is the Josephson penetration depth, the critical current follows the Fraunhofer diffraction formula[10]

$$I_o = I_m\,|(\sin x)/x|, \tag{B1}$$

where

$$x = BW(2\lambda + d)\pi/\Phi_o \tag{B2}$$

and λ is the London penetration depth of the magnetic field into a superconductor. A skewed I_o-vs-B curve, rather than Eq. (B1), results for configurations utilizing a ground plane, but Eq. (B1) is adequate for our purpose. Expanding $\sin x$ about a representative operating point $x_o = 2$ rad, and replacing B by $N\Phi_o/\pi r^2$, where r is an effective radius of the loop and N is the number of flux quanta enclosed by the loop, one obtains

$$N - N_{op} = \frac{r^2}{2\lambda W}\,\frac{I_m - 2I_o}{I_m}. \tag{B3}$$

Here we have dropped $d \lesssim 50$ Å compared to $\lambda \gtrsim 500$ Å, and set N_{op} equal to the number of enclosed flux quanta at the operating point. Clearly, the number of enclosed flux quanta is quite sensitive to the loop and junction dimensions. For $\lambda = 860$ Å (niobium), a junction with $W = 0.1$ mm and a loop of $r = 1$ mm—dimensions which are large by typical microfabrication standards—the relative suppression of I_o is 1.7×10^{-5} for each new flux quantum, or about 3×10^{-4} for a signal producing 16 pulses (4-bit resolution). That is, each pulse will be mispositioned relative to its neighbor by a relative amount 1.7×10^{-5}, and a train of 16 pulses of the same polarity, from a linearly increasing positive signal, will be compressed by 3 parts in 10^4. Stated another way, if a nominal 16-pulse signal were within 3 parts in 10^4 of its 17-pulse value, it would generate that seventeenth pulse because of the decrease of I_o.

The error increases as the r and W dimensions are reduced to the microfabrication scale. However, the nonlinearity is considerably reduced if one would operate near the top of the I_o-vs-B curve, where the slope is small. For example, at $x \ll 1$, Eq. (B1) gives a relative suppression of I_o equal to 5×10^{-11} per quantum, for the dimensions given above.

All the above numbers are not, possibly, as good as may be desired, but it should be pointed out that we have treated the worst case, in which all of the flux density within the loop is assumed to cross the junction, for example as depicted in Fig. 10(a). An overlap geometry as shown in Fig. 10(b) would largely shield the junction from the magnetic field. Also, one could design shielding elements about the junction. One may wish to use the SQUID as an essentially dc ammeter with extreme precision, in which case a very large number of quanta would be desired. For such applications, one could scale up the effective loop radius, as well as provide for shielding. Thus it appears that the nonlinearity associated with the field dependence of the critical current is a problem which can be handled readily.

A second source of nonlinearity is the field dependence of the penetration depth. Ginzburg-Landau theory predicts[11]

$$\lambda(B) = \lambda(0)\left(1 + \frac{\kappa(\kappa + \sqrt{8})}{8(\kappa + \sqrt{2})}\,\frac{B^2}{B_c^2}\right). \tag{B4}$$

For niobium at 4 K, the Ginzburg-Landau parameter κ is 1, and the critical field B_c is 0.16 T. A field of 3.6×10^{-3} T will change λ by 1 part in 10^4. It would change the effective area and the number of enclosed flux quanta by twice that amount. This field corresponds to more than 5×10^4 flux quanta for a loop of 1 mm effective radius, and 5×10^2 quanta for a 100-μm radius. Thus, for the usual fields expected for A/D conversion, the loop area and inductance would change by entirely negligible amounts. For a precision dc ammeter, the effect could be made negligible by scaling up the dimensions.

[1]F.F. Fang, United States Patent No. 3,983,419; Sept. 28, 1976.
[2]W. Anacker, IBM Tech. Disc. Bull. 18, 567 (1975).
[3]J.P. Hurrell and A.H. Silver, AIP Conf. Proc. 44, 437 (1978).
[4]B.D. Josephson, Phys. Lett. 1, 251 (1962); Rev. Mod. Phys. 36, 210 (1964); Adv. Phys. 14, 419 (1965).
[5]R.L. Peterson and D.G. McDonald, IEEE Trans. Magn. MAG-13, 887 (1977).
[6]R.L. Peterson and R.I. Gayley, Phys. Rev. B 18, 1198 (1978).
[7]D.G. McDonald, E.G. Johnson, and R.E. Harris, Phys. Rev. B 13, 1028 (1976).
[8]R.E. Harris, Phys. Rev. B 13, 3818 (1976).
[9]D.G. McDonald, R.L. Peterson, and B.K. Bender, J. Appl. Phys. 48, 5366 (1977).
[10]See, e.g., C.W. Owen and D.J. Scalapino, Phys. Rev. 164, 538 (1967).
[11]See, e.g., E.A. Lynton, *Superconductivity* (Methuen, London, 1962), p. 46.

APPENDIX D

ATTENUATION IN SUPERCONDUCTING STRIPLINES†

Richard L. Kautz*

ABSTRACT

Measurements of the Q of stripline resonators yield values for the attenuation of Nb-Nb_2O_5-Pb striplines typical of those used in superconducting microcircuits. At 4 K the attenuation between 50 and 500 MHz is proportional to frequency and probably results from dielectric losses. Near the transition temperature of Pb, the attenuation begins to show the frequency-squared dependence associated with superconducting losses.

I. INTRODUCTION

Superconducting stripline resonators have been used by several authors to examine the surface impedance Z_s of superconductors. Measurement of the resonant frequency has been used to determine the imaginary part of Z_s and hence the superconducting penetration depth [1-4] and measurement of the Q has been used to determine the real part of Z_s [2,5]. The present study applies the resonant-cavity technique to measure the attenuation of a Nb-Nb_2O_5-Pb stripline.

II. SAMPLE PREPARATION

The striplines to be considered consist of a niobium groundplane, a dielectric layer of anodic Nb_2O_5, and a Pb-Au alloy strip. In fabrication, a 400 nm layer of Nb is first deposited on a silicon wafer using e-beam evaporation in ultra-high vacuum. The Nb is then anodized under conditions similar to those of Hickmott and Hiatt[6]. The electrolyte consists of 18 gm of ammonium pentaborate dissolved in 200 ml of ethylene glycol. Anodization is carried out at 70° C at a current density of 1 mA/cm^2 until the cell voltage reaches 50 V. This voltage is then maintained until the current has fallen to 0.05 mA/cm^2. Assuming a dielectric constant[4,7] of 29, capacitance measurements yield a dielectric thickness of 134 nm. The stripline is completed by evaporation of Pb and Au to form a pair of Pb-Au alloy strips patterned by photoresist lift-off. Each strip is 600 nm thick, 50 μm wide, and 70 cm long. Use of this balanced pair of striplines, shown in Fig. 1, avoids the necessity of contacting the groundplane. Since the 75 μm separation between strips is much greater than the 134 nm dielectric thickness, the two strips are not coupled.

III. EXPERIMENT

The experimental arrangement for studying the stripline samples consists of a sweep oscillator connected to one end of the stripline via a 50 Ω coaxial line and an oscilloscope connected to the other end also via 50 Ω coax. The difference in characteristic impedance between the stripline (a few tenths of an ohm) and the coaxial lines produces a large reflection coefficient at the ends of the stripline and turns it into a resonant cavity. In this configuration, transmission through the stripline peaks at frequencies for which an integral number of half wavelengths equals the stripline length. Measuring the resonant frequency and stripline length thus yields the phase velocity of the stripline.

In order to accurately measure the cavity Q, it is essential that the external circuit does not significantly load the stripline. To insure this condition, capacitors are inserted in series between the stripline and the 50 Ω coaxial lines. An equivalent circuit of the experimental arrangement then takes the form shown in Fig. 2. The capacitors are chip capacitors of a few pF placed directly against the contact pads on the sample. By changing the size of these capacitors one can determine whether or not external loading is affecting the cavity Q.

If the stripline is characterized by a propagation constant γ and a characteristic impedance Z_o, then the sinusoidal-steady-state solution of the equivalent circuit shown in Fig. 2 is

$$V_L/V_S = \frac{R_L}{R_L + 1/i\omega C_L}\left[2\cosh \gamma \ell + \left\{\frac{Z_o}{R_L + 1/i\omega C_L} + \frac{R_L + 1/i\omega C_L}{Z_o}\right\}\sinh \gamma \ell\right]^{-1} \quad (1)$$

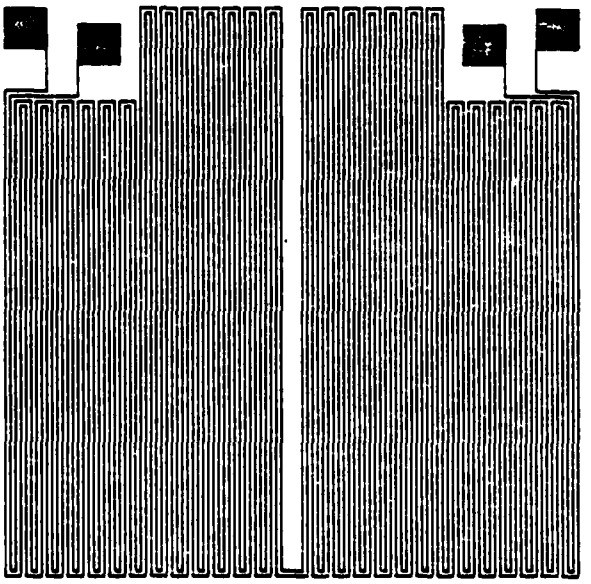

Fig. 1. Geometry of the stripline samples. The pattern is 1.4 cm on a side.

Manuscript received September 28, 1978.

†Partially supported by the Office of Naval Research under contract number N00014-77-F-0048, dated May 1, 1977. Contribution of the U. S. Government, not subject to copyright.

*NRC/NBS Postdoctoral Fellow, Electromagnetic Technology Division, National Bureau of Standards, Boulder, Colorado 80303

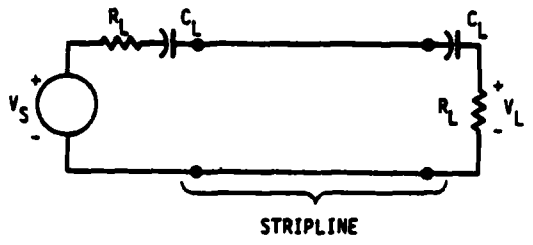

Fig. 2. Equivalent circuit of the experimental arrangement. The resistors R_L replace the 50 Ω coax and 50 Ω load resistors of the sweep generator and oscilloscope. The balanced pair of striplines may be thought of as simple transmission line with the same propagation constant as a single strip and a characteristic impedance twice that of a single strip.

where ℓ is the length of the stripline. This equation defines the amplitude, position, and shape of the resonances observed as the oscillator V_S is swept in frequency. For sufficiently small losses the parameters γ and Z_o can be approximated by

$$\gamma = \alpha + i\omega\sqrt{LC} \quad , \tag{2}$$

$$Z_o = \sqrt{L/C} \quad , \tag{3}$$

where α is the attenuation of the line and L and C are the series inductance and shunt capacitance per unit length. The quantities L and C can be obtained experimentally from a measurement of the phase velocity

$$V_\phi = 1/\sqrt{LC} \quad , \tag{4}$$

combined with a direct capacitance measurement made using a low-frequency bridge. A capacitance measurement made at low frequencies is sufficient in the present case as the dielectric constant of Nb_2O_5 proves to be the same at 10^{11} Hz as at 10^3 Hz[7]. The one parameter of Eq. 1 which remains to be determined is the attenuation. Provided the external loading is small, α fixes the widths of the resonances predicted by Eq. 1 and a least-squares fit to the observed line shape provides an accurate measurement of α. The unloaded Q is related to α by $Q = n\pi/2\alpha\ell$ where n is the resonance number.

IV. RESULTS

Attenuation measurements were made for four striplines for which the Pb-Au alloys of the strip were 0, 4, 8, and 16% Au by weight. The attenuation of each sample was measured over frequencies between 50 and 500 MHz and at temperatures of 4 K and 95% of T_c for the Pb-Au alloy. Data for the 16% Au sample, shown in Fig. 3, typify the results. At 4 K the attenuation of all samples was nearly identical and appeared to be proportional to frequency. As the temperature approached T_c (which ranged from 7.3 K for pure Pb to $7.0^{T_c Pb}$ K for 16% Au), the attenuation began to increase rapidly and the frequency dependence changed from the first power of frequency to something approaching the second power.

While interpretation of this data is far from certain, some tentative conclusions can be reached. The possibility that radiation losses determine the Q can be eliminated on the basis of estimates of the radiation from various stripline discontinuities[8,9] which yield Q's about five orders of magnitude above those observed. Of the remaining two types of loss, dielectric and conductor, we believe the first applies at 4 K and that the second begins to appear as the T_c of the Pb-Au alloy is approached.

Attenuation due to dielectric losses can be expressed in terms of the loss tangent $\varepsilon''/\varepsilon'$.

$$\alpha = \frac{\omega}{2V_\phi} \frac{\varepsilon''}{\varepsilon'} \quad . \tag{5}$$

If the loss tangent is independent of frequency, as is common for many materials, then α is proportional to ω as observed here at 4 K. The attenuation due to conductor losses can be expressed in terms of the surface resistance R_S

$$\alpha = \frac{1}{2wZ_o} \left(R_{S,Pb} + R_{S,Nb}\right) \quad , \tag{6}$$

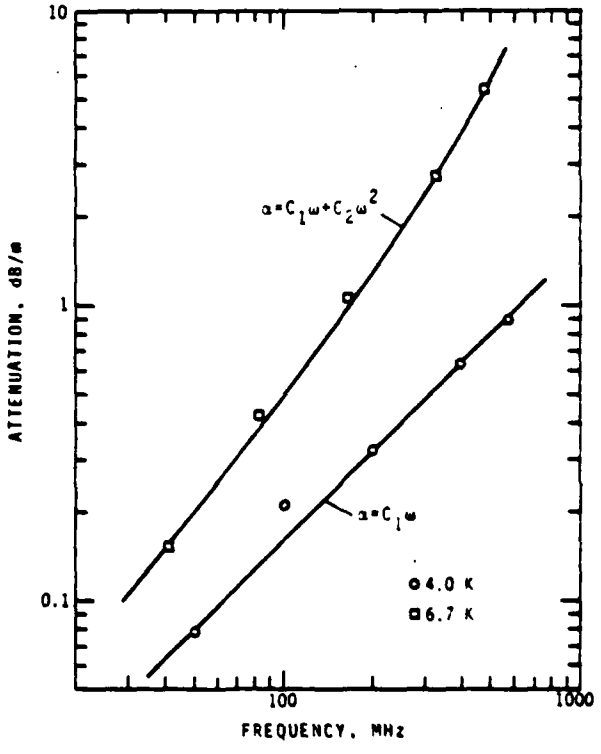

Fig. 3. Attenuation of the 16% Au sample. Circles and squares indicate experimental points at 4 K and 95% of T_c for the Pb-Au alloy respectively. Solid lines are fits to the data based on the indicated frequency dependencies.

where w is the width of the stripline. For superconductors, R_s is very nearly proportional to ω^2 and increases rapidly as the temperature approaches T_c. Thus, it is reasonable to suppose that the attenuation observed near $T_{c,Pb}$ results from a combination of losses in the dielectric and the Pb-Au strip. Losses in the Nb groundplane remain small since temperatures near $T_{c,Nb} = 9.2$ K are never reached.

An experiment that confirms the assumption that dielectric losses dominate at 4 K involves two samples which were prepared differently only in that the final anodization voltages were 50 V and 100 V. If the two samples are assumed identical except for dielectric thickness, then the only parameters to change in equations 5 and 6 are V_f and Z_o. In measurements of the two samples V_f changed by a factor of 1/.86 and Z_o changed by a factor of 1/.57 while the attenuation changed by a factor of 0.82. Thus, the attenuation at 4 K scaled nearly as $1/V_f$, as expected for dielectric losses.

In analyzing the attenuation data to determine the loss tangent of Nb_2O_5 and the surface resistance of Pb, we fit the data at 4 K to the form $\alpha = c_1\omega$ and at 95% of $T_{c,Pb}$ to the form $\alpha = c_1\omega + c_2\omega^2$. The resultant fitting curves for the 16% Au sample are shown in Fig. 3. The values of ϵ''/ϵ' so obtained are given in the following table.

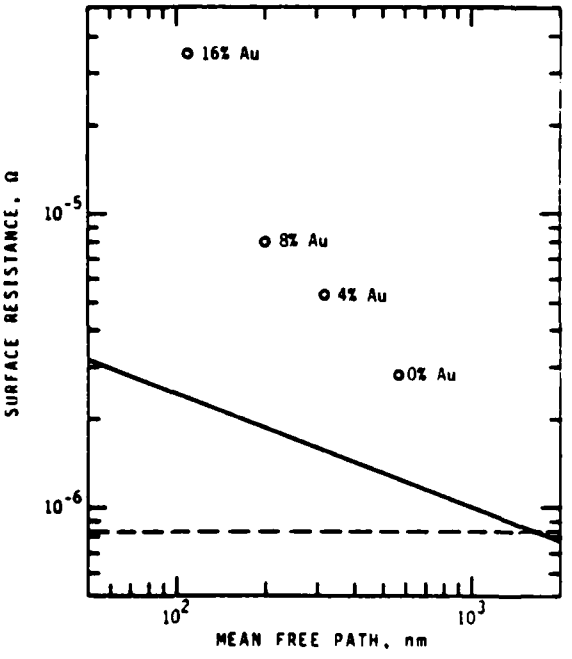

Fig. 4. Surface resistance of the Pb-Au alloy as a function of bulk mean free path. Theoretical results from Mattis-Bardeen theory are indicated by the solid line (local limit) and dashed line (extreme anomalous limit, diffuse scattering.)

Table I. Loss tangent for Nb_2O_5

Sample	T = 4 K	T= 0.95 $T_{c,Pb}$
0% Au	2.21×10^{-3}	3.1×10^{-3}
4% Au	2.14×10^{-3}	2.7×10^{-3}
8% Au	2.12×10^{-3}	2.6×10^{-3}
16% Au	2.08×10^{-3}	3.3×10^{-3}

Since the loss tangent should be independent of the Pb-Au alloy, the scatter obtained for the higher temperature is indicative of an error; most probably due to the insensitivity of the fit to the way losses are apportioned between C_1 and C_2, but perhaps due to experimental errors or an error in interpretation. It is interesting to note that a frequency-independent loss tangent has also been observed by Fuschillo et al.[10] for anodic Nb_2O_5 at room temperature and frequencies above 5×10^9 Hz. Fuschillo et al. attribute this behavior to uncorrelated hopping conduction for which ϵ'' is proportional to temperature. If their room temperature value is extrapolated to 4 K one obtains a loss tangent of 1.4×10^{-3}, in rough agreement with our measurements.

The surface resistance of the Pb-Au alloy at 500 MHz obtained from our fitting procedure is shown in Fig. 4 as a function of the bulk mean-free path ℓ for normal electrons. To estimate ℓ we assume that[11]

$$\sigma_n/\ell = 10^{15} \ \Omega^{-1} \ m^{-2} , \qquad (7)$$

where σ_n is the bulk conductivity at T_c. σ_n is derived in turn from the thin-film conductivity by estimating thickness effects under the assumption of diffuse scattering at the surface[12]. Also shown in Fig. 4 are theoretical results for R_s at 500 MHz and a reduced temperature of 0.95 obtained by applying Mattis-Bardeen theory to Pb in the local limit (solid line) and the extreme anomalous limit with diffuse scattering (dashed Line)[13]. Because the Pippard coherence length ξ_o is 80 nm and the observed penetration depth λ at .95 $T_{c,Pb}$ ranged from 160 nm (for 0% Au) to 250 nm (for 16% Au), neither the local limit (which requires $\ell \ll \lambda$ or $\xi_o \ll \lambda$) or the extreme anomalous limit (which requires $\ell \gg \lambda$ and $\xi_o \gg \lambda$) can be legitimately applied in the present case. However, the rough estimates for R_s so obtained confirm that the observed losses are of the right order of magnitude to be due to superconducting Pb.

CONCLUSION

At 4 K the attenuation observed in the sample striplines can be explained as losses in the Nb_2O_5 dielectric and yield a loss tangent of about 2×10^{-3}. Extrapolation of the dielectric losses to 10 GHz yields an attenuation of 10 dB/m, leading to losses acceptable for most microcircuit applications where stripline lengths are 1 cm or less.

REFERENCES

1. D. R. Young, et al., "Use of a Superconducting Transmission Line for Measuring Penetration Depths," Solid-State Electron., Vol. 1, pp. 378-380, 1960.

2. P. V. Mason and R. W. Gould, "Slow-Wave Structures Utilizing Superconducting Thin-Film Transmission Lines," J. Appl. Phys., Vol. 40, pp. 2039-2051, April 1969.

3. P. V. Mason, "Effect of Tin Additive on Indium Thin-Film Superconducting Transmission Lines," J. Appl. Phys., Vol. 42, pp. 97-102, Jan. 1971.

4. W. H. Henkels and C. J. Kircher, "Penetration Depth Measurements on Type II Superconducting Films," IEEE Trans. Magn., Vol. MAG-13, pp. 63-66, Jan. 1977.

5. A. J. DiNardo, et al., "Superconducting Microstrip High-Q Microwave Resonators," J. Appl. Phys., Vol. 42, pp. 186-189, Jan. 1971.

6. T. W. Hickmott and W. R. Hiatt, "Electrode Effects and Bistable Switching of Amorphous Nb_2O_5 Diodes," Solid-State Electron., Vol. 13, pp. 1033-1047, 1970.

7. G. Basavaiah and J. H. Greiner, "Capacitance and Ellipsometrically Determined Oxide Thickness of Nb-oxide-Pb Josephson Tunnel Junctions," J. Appl. Phys., Vol. 47, pp. 4201-4202, 1976.

8. L. Lewis, "Radiation from Discontinuities in Strip-Line," Proc. IEE, Vol. 107C, pp. 163-170, Feb. 1960.

9. L. J. van der Psuw, "The Radiation of Electromagnetic Power by Microstrip Configurations," IEEE Trans. Microwave Theory Tech., Vol. MTT-25, pp. 719-725, Sept. 1977.

10. N. Fuschillo, et al., "Hopping Conduction in Amorphous Nb_2O_5 Thin Films," J. Non-Crystalline Solids, Vol. 21, pp. 85-94, 1976.

11. R. G. Chambers, "The Anomalous Skin Effect," Proc. Roy. Soc. (London), Vol. A215, pp. 481-497, 1952.

12. E. H. Sondheimer, "The Mean Free Path of Electrons in Metals," Advance in Phys., Vol. 1, pp. 1-42, Jan. 1952.

13. G. M. Ginsberg and L. C. Hebel, "Nonequilibrium Properties," in Superconductivity, Vol. 1, R. D. Parks Ed., New York: Dekker, 1969.

APPENDIX E

JOURNAL OF RESEARCH of the National Bureau of Standards
Vol. 84, No. 3, May–June 1979

Miniaturization of Normal-State and Superconducting Striplines†

R. L. Kautz*

Center for Electronics and Electrical Engineering, National Bureau of Standards, Boulder, Colorado 80303

December 19, 1978

The properties of normal-state and superconducting striplines are calculated as a function of miniaturization. For normal conductors the Reuter-Sondheimer theory is applied in order to account for the effects of finite film thickness and mean free path. For superconductors the Mattis-Bardeen theory is used in order to include effects due to the energy gap. Calculations for three example conductors, copper at 295 K and 4.2 K and niobium at 4.2 K, examine the attenuation, dispersion, and characteristic impedance of striplines as a function of frequency and dielectric thickness. Simulations of pulse transmission are used to evaluate the utility of the example striplines for high-speed digital applications.

Key words: Copper; niobium; stripline; superconductivity; surface impedence.

1. Introduction

Striplines interconnect the active devices of both semiconductor and Josephson-junction high-speed integrated circuits. The desirability of high device densities, particularly for digital circuits, provides motivation for the miniaturization of all circuit components, including striplines. At present, device densities for semiconductor logic circuits having 100 ps propagation delays are limited to about 25 gates per chip, simply because each gate consumes 40 mW of power [1][1]. In contrast, Josephson-junction circuits of comparable speed require only about one thousandth as much power [2] and correspondingly higher device densities are anticipated [3]. While power dissipation presently limits the scale of integration for high-speed semiconductor circuits, it has also been noted that the normal-metal interconnections used in such circuits degrade much more rapidly with miniaturization than the superconducting interconnections of Josephson-junction circuits [4]. Here we present detailed calculations comparing the properties of normal-state and superconducting striplines.

The stripline geometry to be considered is shown in figure 1. For striplines typical of semiconductor circuits, the conductor and dielectric thickness, d and s, are 1 and 200 μm respectively [5], while for superconducting circuits these dimensions are both around 0.2 μm [6]. Thus, although the conductors are of roughly the same thickness in both technologies, the dielectric thicknesses differ by three orders of magnitude. The thinner dielectric of the superconducting circuit permits higher device densities for two reasons. First, because the characteristic impedance of a stripline is, to a good approximation, a function only of the dielectric constant and the ratio of strip width to dielectric thickness w/s, shrinking the dielectric layer permits smaller strip widths while maintaining the same impedance level. Second, because adjacent striplines become coupled if the separation between them is less than a few dielectric thicknesses [7], thinning the dielectric layer permits closer spacing of the striplines while avoiding crosstalk. The actual strip widths used in semiconducting and superconducting circuits are typically 100 μm [5] and 5 μm [8] respectively, and differ by less than a factor of 10^3 primarily because different impedance levels are appropriate for the active devices of the two technologies. For present superconducting circuits, crosstalk can probably be avoided if striplines are separated by 1 μm, while for semiconducting circuits a separation of at least 400 μm is required. One concludes that the miniaturi-

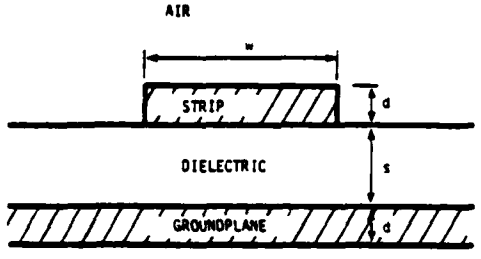

FIGURE 1. *Stripline geometry in cross-section.*

† Partially supported by the Office of Naval Research under contract number N0001-4-77-F-0048, dated May 1, 1977.

* NRC-NBS Postdoctoral Research Associate, Electromagnetic Technology Division.

[1] Figures in brackets indicate literature references at the end of this paper.

zation of striplines beyond their present size in semiconductor circuits can proceed without reduction of the conductor thickness but not without thinning the dielectric.

As will be shown, both radiation and dielectric losses become relatively less important compared to conductor losses as the dielectric thickness is reduced. For the purpose of this study, it thus proves sufficient to focus on the effects associated with imperfect conductors, assuming a lossless dielectric and neglecting radiation. The effect of miniaturization is considered for striplines made from three different conductors, copper at 295 K and 4.2 K and niobium at 4.2 K. These conductors represent respectively, a normal metal exhibiting the normal and anomalous skin effects (at the frequencies of interest) and a superconductor.

To further simplify the calculations, we consider only the TEM mode and the stripline width is taken to be much greater than the dielectric thickness, $w \gg s$, such that fringing fields can be neglected. These assumptions eliminate dispersion associated with the discontinuity in dielectric constant at the air/dielectric interface, an important source of dispersion for w comparable to or smaller than s [9, 10]. One notes, however, that for the TEM mode such dispersion can be reduced to an arbitrary magnitude by overlaying the stripline with a dielectric layer of sufficient thickness.

Under the above assumptions the properties of a stripline follow almost immediately once the surface impedance of the conductor is calculated. In section 2, expressions for the surface impedance of both normal-metals and superconductors of finite thickness are reviewed. These expressions are used in section 3 to evaluate the attenuation, phase velocity, and characteristic impedance as a function of dielectric thickness assuming a fixed conductor thickness of 1 μm. Section 4 looks at the propagation of short pulses over various lengths of stripline.

2. Surface Impedance

The surface impedance required here is a quantity which abstracts information about the penetration of fields into an infinite conducting slab of thickness d. Taking the surfaces of the conductor as the planes $z = 0$ and $z = d$, the surface impedance is defined for a sinusoidal electric field $E_x(z, \omega)e^{i\omega t}$ and current density $J_x(z, \omega)e^{i\omega t}$ by

$$Z_s(\omega) = \frac{E_x(0, \omega)}{\int_0^d dz J_x(z, \omega)}. \tag{2.1}$$

with the boundary condition that the magnetic field be zero at $z = d$ as is appropriate for a stripline with $w \gg s$. The real part of Z_s, called the surface resistance, accounts for stripline losses and the imaginary part, the surface reactance, contributes to the stripline inductance.

Evaluation of the surface impedance for copper at 295 K and niobium at 4.2 K is simplified by the fact that J and E are related by the local equation

$$\mathbf{J} = \sigma \mathbf{E}, \tag{2.2}$$

where σ is the complex conductivity. This local equation can be assumed because the mean free path l for normal electrons is short compared to all other dimensions in the problem. Combining eq. (2.2) with Maxwell's equations yields for the surface impedance [11]

$$Z_s = (i\omega\mu_o/\sigma)^{1/2} \coth\left[(i\omega\mu_o\sigma)^{1/2}d\right] \tag{2.3}$$

The surface impedance thus follows once the conductivity is known. For copper σ is simply a real constant. For superconducting niobium, σ is a complex, frequency-dependent quantity which we take to be of the form given by Mattis and Bardeen [12]. The Mattis-Bardeen equation yields the conductivity of a superconductor at a given frequency and temperature provided two material parameters are known; the energy gap parameter Δ and the normal state conductivity at the superconducting transition temperature σ_n. A more complete account of the application of Mattis-Bardeen theory to superconducting striplines has been given elsewhere [13].

In the derivation of eq. (2.3) for the case of infinite conductor thickness, it is observed that the field amplitudes decay exponentially with distance into the conductor. For a normal metal the characteristic decay length is the classical skin depth

$$\delta_c = (\omega\mu_o\sigma/2)^{-1/2}. \tag{2.4}$$

Because δ_c decreases with increasing frequency there exists a frequency above which $\delta_c < l$ and a local relation between J and E can no longer be assumed. At such high frequencies the skin effect is said to be anomalous. For a superconductor, the decay length at frequencies less than the energy gap frequency, $2\Delta/\hbar$, is the penetration depth [14]

$$\lambda = (\hbar \coth(\Delta/2kT)/\pi\mu_o\Delta\sigma_n)^{1/2}, \tag{2.5}$$

which, in contrast to δ_c, is frequency independent. In the process of miniaturizing striplines, the depth of field penetration plays an increasingly important role as the dielectric thickness is reduced.

Because the mean free path of copper at 4.2 K can be long compared to both δ_c, and d, the relation between J and E assumes the non-local form [15]

$$\mathbf{J}(\mathbf{r}) = \frac{3\sigma}{4\pi l}\int d^3\rho\,\boldsymbol{\rho}(\boldsymbol{\rho}\cdot\mathbf{E}(\mathbf{r}+\boldsymbol{\rho}))\,\rho^{-4}e^{-\rho/l}. \tag{2.6}$$

where we have assumed that the relaxation time τ is small compared to the inverse frequency, $\omega\tau \ll 1$. Evaluation of

the surface impedance in this case requires an additional boundary condition regarding the scattering of electrons from the conductor surface. Of the two simple limits, diffuse scattering and specular reflection, the former seems to provide the better agreement with experiment [15] and has been assumed in the present calculations. Equation (2.4) and Maxwell's equations applied to the surface problem with diffuse scattering yield [15].

$$\frac{d^2E_x}{dz^2} = i\alpha l^{-3}\int_0^d dz' E_x(z')K((z'-z)/l)$$
$$K(u) = \int_1^\infty dr\left[\frac{1}{r} - \frac{1}{r^3}\right]e^{-|u|r} \tag{2.7}$$

where $\alpha = 3/2\ l^3/\delta_c^3$. Reuter and Sondheimer [16] solved this equation in the limit of infinite d and obtain for the surface impedance

$$Z_s = i\frac{4\pi}{3}\frac{\alpha}{\sigma l}\left[\int_0^\infty dt\ ln(1 + i\alpha k(t)/t^3)\right]^{-1}$$
$$k(t) = \frac{2}{t^3}[(1+t^2)\tan^{-1}(t) - t]. \tag{2.8}$$

For $\alpha \ll 1$, (normal skin effect), this expression reduces to the $d = \infty$ limit of eq (2.3). For $\alpha \gg 1$ (extreme anomalous skin effect), Reuter and Sondheimer obtain

$$Z_s = \frac{1}{3^{1/3}\pi^{1/3}}(1+\sqrt{3}\,i)\frac{\alpha^{2/3}}{\sigma l}, \quad \alpha \gg 1. \tag{2.9}$$

The expressions for the surface impedance of a normal metal given above are valid either for $l \ll \delta_c$, d (eq (2.3)) or for arbitrary l and $d = \infty$ (eq (2.8)). The numerical solution of eq (2.7) and calculation of the surface impedance for arbitrary l, δ_c, and d is discussed in the appendix. The resulting general program was used to obtain all results for normal metals presented here.

Although the fields do not fall off in a precisely exponential way for the anomalous skin effect, it remains possible to define a characteristic penetration length. In general, the distance over which the field amplitude decays is given by

$$\delta = \frac{1}{\omega\mu_0}\frac{|Z_s|^2}{Re[Z_s]}. \tag{2.10}$$

In the local limit this reduces to δ_c for a normal metal and to λ for a superconductor. In the extreme anomalous limit, eq (2.9) may be used to obtain

$$\delta_a = \frac{2^{1/3}3^{1/6}}{\pi^{1/3}}(\delta_c^2 l)^{1/3}. \tag{2.11}$$

so that the skin depth for $l > \delta_c$ is greater than δ_c.

TABLE I. *Material Parameters.*

	σ (Ω^{-1}m^{-1})	l (m)	τ (s)	
Cu, 295 K	5.88×10^7	3.82×10^{-8}	2.34×10^{-14}	
Cu, 4.2 K	2.94×10^{10}	1.91×10^{-6}	1.19×10^{-11}	
	σ_n (Ω^{-1}m^{-1})	l (m)	Δ (meV)	λ (m)
Nb, 4.2 K	1.57×10^7	1.1×10^{-6}	1.48	8.6×10^{-8}

The material parameters of copper and niobium used here are presented in table 1. The conductivity of copper at room temperature [17] is limited by phonon scattering and all specimens have nearly the same value. At 4.2 K scattering from impurities and defects dominate and, although the conductivity can be more than 10^4 times that at 295 K for specially prepared samples, a residual resistance ratio of 10^2 is common for off-the-shelf wires [18]. Here we assume, perhaps optimistically, that the conductivity at 4.2 K is 500 times the room temperature value. The mean free path is derived from the fact that σl is approximately constant for a given material and has a value of $1.54 \times 10^{15}\ \Omega^{-1}\ m^{-2}$ for copper [11]. The relaxation time is calculated from

$$\tau = l/v_F, \tag{2.12}$$

where the Fermi velocity v_F is 1.6×10^6 m/s for copper [11]. Material parameters for superconducting niobium are based on the thin-film measurements of Henkels and Kircher [19]. The measured value of σ_n, $1.59 \times 10^7\ \Omega^{-1}\ m^{-1}$, was modified slightly so that eq (2.5) is exactly satisfied.

The real and imaginary parts of the surface impedance of the three example metals are shown in figure 2 for a metal thickness of 1 μm. Because the mean free path is much shorter than the film thickness, the surface impedance of copper at 295 K is described by the local formula, eq. (2.3), for frequencies below about 3×10^{12} Hz. Above this frequency, the classical skin depth is smaller than the mean free path and the skin effect is anomalous. At sufficiently low frequencies δ_c is large compared to the conductor thickness and eq (2.3) reduces to

$$Z_s = \frac{1}{\sigma d} + i\frac{1}{3}\omega\mu_0 d, \quad l \ll d \ll \delta_c. \tag{2.13}$$

This equation, which results when the electric field is uniform across the conductor thickness, accounts for the impedance of copper at 295 K and below about 4×10^9 Hz

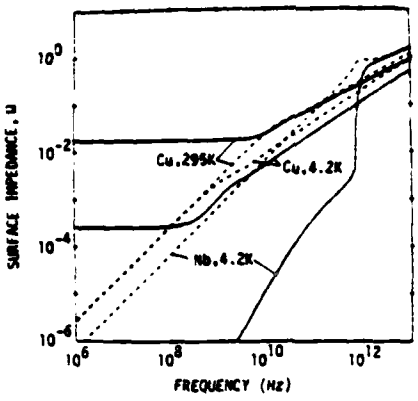

FIGURE 2. *The real (solid line) and imaginary (dashed line) parts of the surface impedance for 1 μm thick films of copper at 295 K and 4.2K and niobium at 4.2 K.*

The results for copper at 4.2 K and frequencies above 10^{13} Hz may be inaccurate due to the omission of relaxation-time effects.

shown in figure 2. At higher frequencies δ_c becomes small compared to d and eq 2.3 reduces to

$$Z_s = (1 + i)\left(\frac{\omega\mu_0}{2\sigma}\right)^{1/2}. \quad l \ll \delta_c \ll d. \quad (2.14)$$

In this limit the electric field decays exponentially to a small value before reaching the back surface of the conductor.

At 4.2 K the mean free path of copper is sufficiently long that δ_c is comparable to l even at 2×10^4 Hz. Thus, the anomalous skin effect is exhibited over the entire frequency range of figure 2. The relaxation time is sufficiently long at 4.2 K that $\omega\tau$ is unity at 10^{10} Hz (compared to 7×10^{12} Hz at room temperature). Pippard [15] has shown, however, that in the extreme anomalous limit, relaxation-time effects are important only when $\omega\tau$ is considerably greater than unity and in the present case need not be considered for frequencies less than about 10^{12} Hz. Since the relaxation time has been neglected, the results shown in figure 2 for copper at 4.2 K are probably not accurate above this frequency. As at room temperature, the surface impedance at 4.2 K depends critically on whether the skin depth is greater or less than the conductor thickness. The break point occurs when $\delta_n = d$ or about 2×10^8 Hz. Below this frequency, Z_s is given by an equation similar to eq (2.13) in which the bulk conductivity σ is replaced by an apparent conductivity $\tilde{\sigma}$ that accounts for the effect of finite conductor thickness on the mean free path [20]. In the present case, the apparent conductivity is 0.13 times the bulk conductivity. At frequencies above 2×10^8 Hz we have $\delta_c \ll l, d$ and eq (2.9) applies. As can be easily verified from eq (2.9), the surface impedance in this region depends only on σ/l, a constant of the material, and thus does not depend on the somewhat arbitrarily chosen residual resistivity ratio. If, for example, the resistivity ratio had been taken as 5000 rather than 500, the only significant change in the surface impedance would be a six-fold decrease in $Re[z_s]$ below 2×10^8 Hz. These considerations have been discussed in detail by Keyes et al. [4].

Below the energy gap frequency, 7.2×10^{11} Hz for Nb at 4.2 K, the surface resistance of a superconductor is orders of magnitude smaller than that of a normal metal. In a stripline the smaller surface resistance results in lower attenuation. Also, the surface reactance below the energy gap varies as ω, making it appear exactly as an inductance. This property yields a stripline with very low dispersion. Above the energy gap, a superconductor behaves like a normal metal of conductivity σ_n.

3. Propagation Constant and Characteristic Impedance

The propagation constant γ and characteristic impedance Z_0 of a stripline can be expressed in terms of the series impedance Z and shunt admittance Y of a unit length of line.

$$\gamma = \sqrt{ZY}. \quad (3.1)$$

$$Z_0 = \sqrt{Z/Y}. \quad (3.2)$$

where Z and Y for $w >> s$ are in turn [11]

$$Z = i\omega\mu_0 \frac{s}{w} + \frac{2}{w} Z_s. \quad (3.3)$$

$$Y = i\omega\epsilon\epsilon_0 \frac{w}{s}. \quad (3.4)$$

The first term of Z is the inductive impedance associated with the magnetic field in the dielectric region and the second term accounts for penetration of fields into the conductor. Y is the capacitive admittance between the strip and the ground plane. In the following calculations a relative dielectric constant ϵ of 4 is arbitrarily assumed. Note that γ is independent of w while Z_0 is proportional to $1/w$. Thus, both γ and $\frac{w}{s} Z_0$ can be calculated without specifying the stripline width. The power attenuation in decibels per length α_{dB} and the phase velocity v_ϕ are related to the real and imaginary parts of γ by

$$\alpha_{dB} = C_{dB}\, Re[\gamma]. \quad (3.5)$$

$$v_\phi = \omega / Im[\gamma]. \quad (3.6)$$

where $C_{dB} = 20 \log_{10} e$. The properties of a stripline thus follow from the surface impedance of the conductor.

The phase velocity, attenuation, and characteristic impedance of a room temperature copper stripline are shown in figure 3 for a conductor thickness of 1 μm and a dielectric thickness ranging from 200 μm to 0.2 μm. As the dielectric thickness is reduced toward 0.2 μm, the line becomes highly dispersive and lossy and develops a characteristic impedance far from the real, frequency-independent impedance of an ideal line. As a function of frequency the degradation of a fixed length of line due to loss and dispersion increases with increasing frequency. This increase in dispersion is less than obvious since the phase velocity approaches a constant at high frequencies but will be explained presently. Problems with impedance matching are reduced at high frequencies as the characteristic impedance approaches a real constant.

A better understanding of the results shown in figure 3 can be obtained by reviewing approximate expressions for γ and Z_o applicable in the four regions bounded by dotted lines. These regions are defined by

$$\text{I. } d, \sqrt{sd} << \delta_c$$

$$\text{II. } d << \delta_c << \sqrt{sd}$$

$$\text{III. } \delta_c << s, d$$

$$\text{IV. } s << \delta_c << d$$

and result from the two possible forms for the surface impedance, eqs (2.13) and (2.14), combined with two possibilities for the series impedance of eq (3.3), either resistive or reactive. Of the four regions, I, II, and III are of principal interest here since condition IV is satisfied only for the 0.2 μm dielectric case over a narrow range of frequencies.

The asymptotic forms for the phase velocity in the regions of interest are

$$\text{I. } v_\phi = \sqrt{\frac{\omega s d \sigma}{\epsilon\epsilon_o}}\left[1 - \frac{1}{3}\frac{d^2}{\delta_c^2} - \frac{1}{2}\frac{sd}{\delta_c^2}\right]. \tag{3.7}$$

$$\text{II. } v_\phi = \frac{1}{\sqrt{\mu_o\epsilon\epsilon_o}}\left[1 - \frac{1}{3}\frac{d}{s} - \frac{1}{8}\frac{\delta_c^4}{s^2 d^2}\right] \tag{3.8}$$

$$\text{III. } v_\phi = \frac{1}{\sqrt{\mu_o\epsilon\epsilon_o}}\left[1 - \frac{1}{2}\frac{\delta_c}{s}\right] \tag{3.9}$$

where correction terms have been indicated in brackets. As figure 3 indicates, approximations I, II, and III become valid at successively higher frequencies. In the lowest frequency range v_ϕ is proportional to $\sqrt{\omega}$ and goes to zero at zero frequency. If, however, one considers the phase shift that results because the low frequencies travel at a velocity less than the high-frequency asymptotic velocity then for a fixed length of line ℓ this phase shift

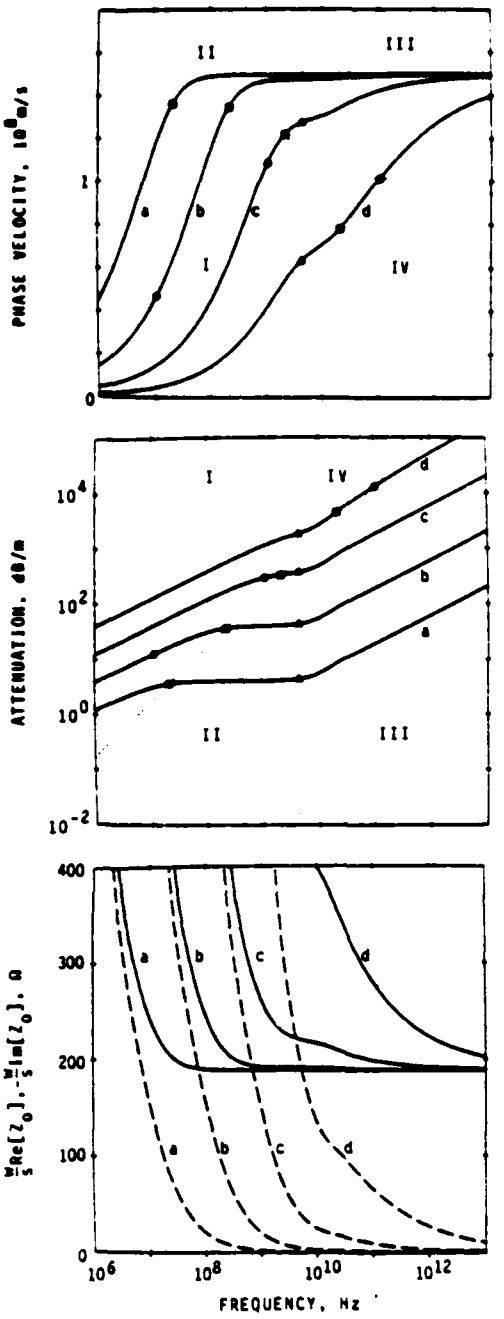

FIGURE 3. *Phase velocity, attenuation, and real (solid line) and imaginary (dashed line) parts of the characteristic impedance of a 295 K copper stripline with 1 μm conductor thickness.*

Results are shown for a relative dielectric constant of 4 and dielectric thicknesses of 200 μm (a), 20 μm, (b) 2 μm, (c), and 0.2 μm (d). Dotted lines divide the graphs of phase velocity and attenuation into regions where simple approximate equations hold. Circles, squares, and triangles mark points at which $\delta_c = s$, $\delta_c = \sqrt{sd}$, and $\delta_c = d$, respectively.

$$\Delta\phi = \omega\ell\left(\frac{1}{v_\phi(\omega)} - \frac{1}{v_\phi(\infty)}\right).$$

also goes to zero at zero frequency as $\sqrt{\omega}$. Thus, dispersion at low frequencies is not the problem that figure 3 suggests. At somewhat higher frequencies δ_c becomes less than $\sqrt{sd}$ and approximation II applies. In this region v_ϕ approaches the asymptotic value $(1 - d/3s)/\sqrt{\mu_o\epsilon\epsilon_o}$ with a correction term which decreases as ω^{-2} with increasing frequency. Finally, as δ_c becomes less than d as well as s, v_ϕ approaches $1/\sqrt{\mu_o\epsilon\epsilon_o}$ with a correction term of $-\delta_c/2s$. Because this term goes as $1/\sqrt{\omega}$, the phase shift $\Delta\phi$ goes as $\sqrt{\omega}$ and dispersion effects increase with ω just as at very low frequencies. Also note that the correction term is proportional to $1/s$ so that thin dielectrics enhance dispersion.

The attenuation can be approximated in the regions of interest by

$$\text{I. } \alpha_{dB} = C_{dB}\sqrt{\frac{\omega\epsilon\epsilon_o}{sd\sigma}}\cdot\left[1 - \frac{1}{3}\frac{d^2}{\delta_c^2} - \frac{1}{2}\frac{sd}{\delta_c^2}\right]. \quad (3.10)$$

$$\text{II. } \alpha_{dB} = \frac{C_{dB}}{\sigma sd}\sqrt{\frac{\epsilon\epsilon_o}{\mu_o}}\left[1 - \frac{1}{3}\frac{d}{s} + \frac{4}{45}\frac{d^4}{\delta_c^4}\right]. \quad (3.11)$$

$$\text{III. } \alpha_{dB} = \frac{C_{dB}}{s}\sqrt{\frac{\omega\epsilon\epsilon_o}{2\sigma}}\left[1 - \frac{1}{2}\frac{\delta_c}{s}\right]. \quad (3.12)$$

As a function of frequency, α_{dB} increases as $\sqrt{\omega}$ at very low and very high frequencies with a frequency independent plateau in between. As a function of dielectric thickness, α_{dB} always increases with decreasing dielectric thickness, either as $1/\sqrt{s}$ or as $1/s$.

Lastly, the characteristic impedance is approximated by

$$\text{I. } Z_o = \frac{1}{w}\sqrt{\frac{s}{\omega\epsilon\epsilon_o\sigma d}}\left\{\left[1 + \frac{1}{3}\frac{d^2}{\delta_c^2} + \frac{1}{2}\frac{sd}{\delta_c^2}\right] - i\left[1 - \frac{1}{3}\frac{d^2}{\delta_c^2} - \frac{1}{2}\frac{sd}{\delta_c^2}\right]\right\} \quad (3.13)$$

$$\text{II. } Z_o = \frac{s}{w}\sqrt{\frac{\mu_o}{\epsilon\epsilon_o}}\left\{\left[1 + \frac{1}{3}\frac{d}{s} + \frac{1}{8}\frac{\delta_c^4}{s^2d^2}\right] - i\frac{1}{2}\frac{\delta_c^2}{sd}\left[1 - \frac{1}{3}\frac{d}{s} + \frac{4}{45}\frac{d^4}{\delta_c^4}\right]\right\}. \quad (3.14)$$

$$\text{III. } Z_o = \frac{s}{w}\sqrt{\frac{\mu_o}{\epsilon\epsilon_o}}\left\{\left[1 + \frac{1}{2}\frac{\delta_c}{s}\right] - i\frac{1}{2}\frac{\delta_c}{s}\left[1 - \frac{1}{2}\frac{\delta_c}{s}\right]\right\}. \quad (3.15)$$

In the limit of low frequencies the real and imaginary parts of Z_o both diverge as $1/\sqrt{\omega}$. The significance of this divergence relates to the reduction of the transmission line to a simple resistor at low frequencies. For $\delta_c < s, d$ the real part of Z_o approaches its high frequency asymptote, $\frac{s}{w}\sqrt{\mu_o/\epsilon\epsilon_o}$, and the imaginary part goes to zero. The correction term to the real part is $\delta_c/2s$ so that the dielectric thickness directly influences the ability to match impedances over a wide range of frequencies.

The properties of copper and niobium striplines at 4.2 K are shown in figure 4, again for a conductor thickness of 1 μm and dielectric thicknesses ranging from 200 μm to 0.2 μm. Comparing copper at 295 K and 4.2 K shows that the 500 fold increase in conductivity which might result from cooling leads to substantial improvements, especially at low frequencies. These improvements becomes less significant at frequencies approaching 3×10^{12} Hz, where the skin effect becomes anomalous even for copper at 295 K. The superiority of a superconducting stripline at frequencies below $2\Delta/\hbar$ is at once apparent from figure 4. In this region v_ϕ is independent of frequency, α_{dB} is orders of magnitude below the attenuation for a normal conductor, and the characteristic impedance is a real constant. Above 7.2×10^{11} Hz all of these desirable properties disappear as the superconductor begins to behave like a normal conductor.

As for the normal skin effect case at 295 K, simple approximate formulas can be derived for the properties of a stripline in the extreme anomalous limit. The regions of approximation are defined as for the normal skin effect except that δ_c is replaced by δ_a. These regions can be located in figure 4 by using the points marked with circles ($\delta_a = s$), squares ($\delta_a = \sqrt{sd}$), and triangles ($\delta_a = d$) as guides.

At frequencies less than $2\Delta/\hbar$ simple approximations also exist for the parameters of a superconducting stripline [11, 13]. The phase velocity is

$$v_\phi = \frac{1}{\sqrt{\mu_o\epsilon\epsilon_o}}\left(1 + \frac{2\lambda}{s}\coth\frac{d}{\lambda}\right)^{-1/2}, \quad \omega << 2\Delta/\hbar. \quad (3.16)$$

While this equation is similar to eq (3.9) for a normal metal, it differs critically in that λ, as opposed to δ_c, is independent of frequency. Thus, as s decreases v_ϕ also decreases but remains frequency independent. The attenuation is

$$\alpha_{dB} = C_{dB}\,\mu_o^{3/2}\epsilon^{1/2}\epsilon_o^{1/2}\frac{\omega^2\lambda^3\sigma_1}{2s}\left(1+\frac{2\lambda}{s}\coth\frac{d}{\lambda}\right)^{-1/2} \times\left(\coth\frac{d}{\lambda}+\frac{d/\lambda}{\sinh^2 d/\lambda}\right). \quad \omega << 2\Delta/\hbar. \tag{3.17}$$

where σ_1 is the real part of the conductivity. Because σ_1 is only weakly frequency dependent, α_{dB} is nearly proportional to ω^2. For the striplines considered here $\lambda << s, d$ and the attenuation is proportional to $1/s$. The characteristic impedance is

$$Z_o = \frac{s}{w}\sqrt{\frac{\mu_o}{\epsilon\epsilon_o}}\left(1+\frac{2\lambda}{s}\coth\frac{d}{\lambda}\right)^{1/2}. \quad \omega << 2\Delta/\hbar. \tag{3.18}$$

which like v_ϕ changes with s but remains frequency independent. The imaginary part of Z_o is negligible. Thus, for $\omega << 2\Delta/\hbar$, the only serious deterioration of superconducting stripline properties with miniaturization involves the attenuation.

Before discussing how the transmission of pulses is affected by stripline properties, we briefly examine the two sources of loss, dielectric and radiation, which were neglected in the above calculations. Dielectric losses occur when ϵ has a non-zero imaginary part such that $\epsilon = \epsilon' + i\epsilon''$. Assuming $\epsilon'' << \epsilon'$ and a perfect conductor ($Z_s = 0$), the attenuation due to dielectric loss is

$$\alpha_{dB} = \frac{1}{2}C_{dB}\sqrt{\mu_o\epsilon'\epsilon_o}\,\frac{\epsilon''}{\epsilon'}\,\omega. \tag{3.19}$$

For many materials ϵ' and ϵ'' are approximately independent of frequency and α_{dB} increases roughly as ω. For good dielectrics ϵ''/ϵ' is typically 10^{-4} at 10^{10} Hz [21] yielding, for $\epsilon' = 4$, an attenuation of 0.2 dB/m. Because this attenuation is independent of s, the conduction losses will always dominate for small enough s. As can be seen from figures 3 and 4, conduction losses at 10^{10} Hz are greater than 0.2 dB/m for all the normal-state lines considered and for the superconducting lines with $s' = 2\ \mu$m and $0.2\ \mu$m. Because 0.2 dB/m represents a small loss over distances typical of a microcircuit, neglecting dielectric loss will not affect the conclusions of section 4.

A comparison of radiation and conduction losses is complicated by the fact that radiation losses cannot be converted to a loss per unit length, radiation being associated only with discontinuities in the line. In order to estimate the importance of radiation we consider the Q of a half-wave open-end stripline resonator. Radiation from this structure has been calculated by a number of authors, most recently by van der Pauw [22]. Assuming $w >> s >> \delta$, van der Pauw's result for the Q due to radiation losses reduces to

$$Q_R = \frac{1}{\mu_o\epsilon_o\omega_o^2 w^2}\,\frac{\pi^2\epsilon^{3/2}}{2}\left\{\frac{(2\epsilon-1)^2}{3}+\frac{1}{5}\right\}^{-1}. \tag{3.20}$$

where $\omega_o = \pi/\ell\sqrt{\mu_o\epsilon\epsilon_o}$ is the resonant frequency and ℓ is the length of the cavity. The Q due to conduction losses for the same resonator is

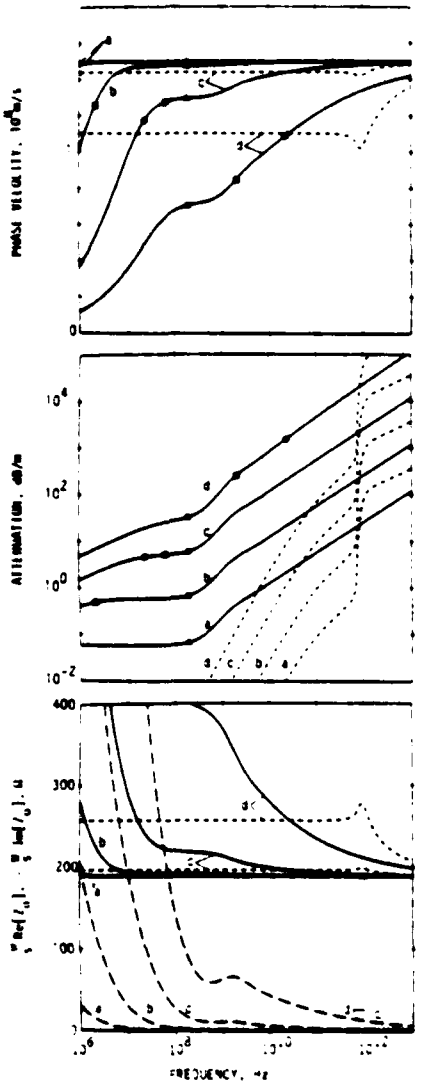

FIGURE 4. *Graphs analogous to figure 3 for copper at 4.2 K (solid lines except long dashes for $Im(Z_o)$) and niobium at 4.2 K (short dashes except dots for $Im(Z_o)$).*

For copper, circles, squares, and triangles mark the points at which $\delta_o = s$, $\delta_o = \sqrt{sd}$, and $\delta_o = d$, respectively.

$$Q_C = \frac{\mu_o \omega_o s}{2Re[Z_s]}. \tag{3.21}$$

If the characteristic impedance is held fixed (w/s constant) then Q_R increases with miniaturization and Q_C decreases. Davidheiser [23] recently noted this fact and determined the dielectric thickness at which the Q of a superconducting resonator is maximum. Since the ratio Q_R/Q_C decreases with increasing ω_o for both the normal and superconducting cases, there is a resonant frequency above which radiation losses dominate conduction losses. This breakpoint frequency is given in table II for the various striplines considered here assuming $w/s = 10$. For the 0.2 and 2 μm dielectrics, the breakpoint occurs at frequencies higher than those of practical interest and radiation losses can be neglected. For the 20 and 200 μm dielectrics, radiation begins to become important at frequencies around 10^{10} Hz. Since the wavelength is 1.5 cm at 10^{10} Hz for $\epsilon = 4$, microcircuit striplines could be of the right length to approximate a half-wavelength antenna.

While the load at the ends of a microcircuit stripline is not infinite, the radiation from a matched or shorted end is a sizable percentage of that from an open end [24]. Thus radiation losses may well be important at gigahertz frequencies for dielectric thickness greater than 20 μm.

A further consideration omitted from the present calculations regards the propagation of modes of higher order than the assumed TEM mode. Such higher-order modes become possible at frequencies sufficiently high that a half wavelength is comparable to the cross-sectional dimensions of the stripline (10). Assuming $w >> s$ the cutoff frequency is

$$\omega_c = \pi / w \sqrt{\mu_o \epsilon \epsilon_o}. \tag{3.22}$$

such that for $\epsilon = 4$ and $w = 200$ μm the cutoff is at 4×10^{11} Hz. Thus, even for striplines of large dimensions in the context of microcircuits, the higher-order modes are important only at frequencies above those of immediate interest.

TABLE II. *Frequency (Hz) at which radiation and conduction losses are equal for a half-wave open-ended stripline resonator with w/s = 10 and $\epsilon = 4$.*

s (μm)	0.2	2	20	200
Cu, 295 K	2.0×10^{12}	1.3×10^{12}	8.0×10^{10}	5.0×10^{9}
Cu, 4.2 K	1.7×10^{13}	8.9×10^{11}	4.6×10^{10}	2.4×10^{9}
Nb, 4.2 K	2.6×10^{13}	1.7×10^{12}	1.4×10^{9}	3.2×10^{9}

IV. Pulse Propagation

The evaluation of a stripline from the standpoint of pulse transmission follows from a knowledge of γ and Z_o but is sufficiently complicated that simulations prove valuable. In this section we consider the propagation of Gaussian pulses over a stripline of length ℓ using the circuit shown in figure 5. The source/load impedance R_L is matched to the asymptotic high-frequency value of Z_o in the case of a normal-state stripline

$$R_L = \frac{s}{w} \sqrt{\frac{\mu_o}{\epsilon \epsilon_o}}. \tag{4.1}$$

and in the superconducting case is matched to the low-frequency impedance

$$R_L = \frac{s}{w} \sqrt{\frac{\mu_o}{\epsilon \epsilon_o}} \left(1 + \frac{2\lambda}{s} \coth \frac{d}{\lambda} \right)^{1/2}. \tag{4.2}$$

The degree to which a voltage pulse V_S is faithfully reproduced across the load is affected both by γ, in the dispersion and attenuation of the line, and by Z_o, in reflections at the interface between the line and the source or load due to imperfect impedance matching.

The Gaussian pulses considered are of the form

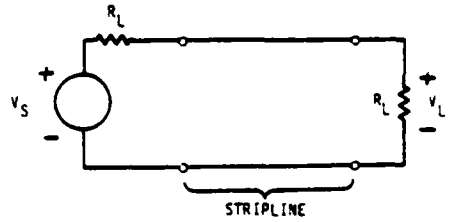

FIGURE 5. *Circuit for analysis of pulse transmission.*

$$V_S(t) = V_o e^{-t^2/2\tau^2}. \tag{4.3}$$

where the standard deviation τ measures the pulse width. Taking the Fourier transform obtains

$$V_S(\omega) = (2\pi)^{1/2} \tau V_o e^{-\omega^2 \tau^2/2}. \tag{4.4}$$

so that the frequency spectrum is also Gaussian with a standard deviation $\Delta\omega = 1/\tau$. Solving the circuit of figure 5 for the sinusoidal steady-state yields

$$V_L(\omega)/V_S(\omega) = \left(2 \cosh \gamma \ell + \left(\frac{Z_o}{R_L} + \frac{R_L}{Z_o} \right) \sinh \gamma \ell \right)^{-1}. \tag{4.5}$$

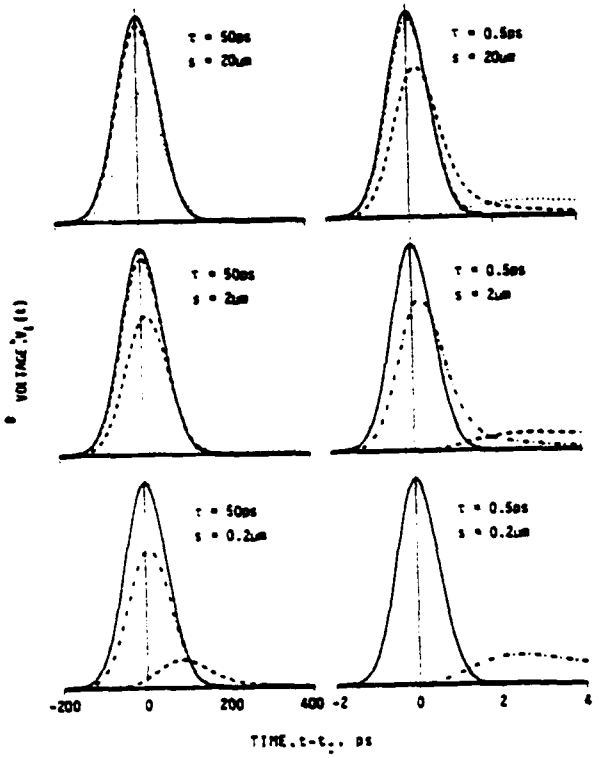

FIGURE 6. *Propagation of Gaussian pulses for a copper stripline at 295 K for various dielectric thicknesses, line lengths, and pulse widths.*

Pulses are shown for line lengths of zero (solid curve), 0.1 cm (dot-dash), 1 cm (dash), and 10 cm (dot). Curves which essentially coincide with the zero length curve have not been graphed. The time origin is shifted by an amount $t_\ell = \ell/v_\phi(\infty)$ where $v_\phi(\infty) = 1.5 \times 10^8$ m/s is the high-frequency phase velocity.

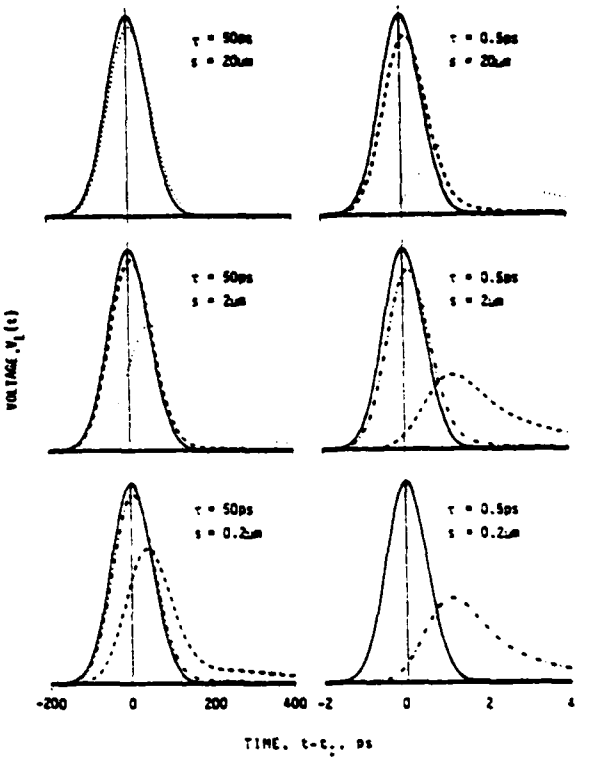

FIGURE 7. *Graphs analogous to figure 6 for a copper line at 4.2 K.*

so that the pulse received at the load takes the form

$$V_L(t) = (2/\pi)^{1/2}\,\tau V_0 \int_0^\infty d\omega\, e^{-\omega^2\tau^2/2} \times Re\left[e^{i\omega t}\left(2\cosh\gamma\ell + \left(\frac{Z_0}{R_L} + \frac{R_L}{Z_0}\right)\sinh\gamma\ell\right)^{-1}\right] \tag{4.6}$$

Numerical evaluation of the above integral was used to determine the shape of a pulse after traversing various lengths of stripline. Since R_L and Z_0 are both proportional to $1/\mu$ these calculations do not depend on the stripline width.

The results of such simulations for copper striplines at 295 K and 4.2 K are shown in figures 6 and 7. For a given dielectric thickness and initial pulse width, pulses are shown as they would appear after traversing striplines of length 0, 0.1, 1, and 10 cm. The time origin for each trace has been shifted by an amount

$$\tau_\ell = \ell/v_\phi(\infty). \tag{4.7}$$

such that a pulse traveling at the asymptotic high-frequency phase velocity $v_\phi(\infty)$ would always be centered at the origin. The results shown in the left column of figures 6 and 7 are for a pulse of $\tau = 50$ ps or roughly at the upper limit of speed for present digital circuits. If we arbitrarily require that a pulse be received with at least 80 percent of its original amplitude to be useful in digital applications, then we see from figure 6 that for $s = 20$ μm, 2 μm, and 0.2 μm useful stripline lengths are less than 10 cm, 1 cm, and 0.1 cm, respectively. Thus, the performance of a room-temperature copper stripline with a dielectric thickness of 2 μm or less can be a limiting factor even for lengths typical of microcircuit dimensions. At 4.2 K this situation is improved by an order of magnitude in that a dielectric thickness of only about 0.2 μm yields lines of sufficient quality for digital microcircuits.

Theoretical arguments indicate that it may be possible to generate pulses with widths as short as 1 *ps* using superconducting devices [25]. The propagation of such a pulse on normal-state striplines is shown in the right column of figures 6 and 7, using a τ of 0.5 *ps* to give a full width of about 1 *ps*. In going from $\tau = 50$ *ps* to $\tau = 0.5$ *ps* one notes that the distortion of the shorter pulse is much the same as that of the

longer after propagating only one tenth the distance. Thus, for $\tau = 0.5$ *ps*, a copper line at 295 K suitable for digital microcircuits requires more than 20 μm of dielectric and at 4.2 K requires more than 2 μm.

Further insight into the transmission of pulses is gained by examining four limiting situations in which the transfer function of eq (4.5) can be simplified. To do this we introduce the series resistance R and inductance L of a unit length of line defined by

$$Z = R + i\omega L \tag{4.8}$$

and the shunt capacitance C per unit length defined by

$$Y = i\omega C \tag{4.9}$$

For the striplines considered here both R and L are in general frequency dependent. The four limits to be discussed result from two different possibilities for Z in combination with two possibilities for the length of the line. If the resistive part of Z is much larger than the reactive part then L can be neglected and we describe the line as being an RC line. The propagation constant and characteristic impedance of the *RC* line are

$$\gamma = (1 + i)\sqrt{R\omega C/2}, \qquad \omega << R/L \tag{4.10}$$

$$Z_o = (1 - i)\sqrt{R/2\omega C},$$

These forms are precisely those which lead to the low-frequency divergences shown in figures 3 and 4 for normal-state lines. Because $Re[Z_s] << Im[Z_s]$ for a superconductor, no similar *RC* behavior occurs in this case. When the reactive part of Z is much larger than the resistive part the line is said to be an *LC* line and we have

$$\gamma = \frac{R}{2\sqrt{LC}} + i\omega\sqrt{LC}\left[1 + \frac{1}{8}\frac{R^2}{\omega^2 L^2}\right], \qquad \omega >> R/L. \tag{4.11}$$

$$Z_o = \sqrt{L/C} - i\frac{R}{2\omega\sqrt{LC}},$$

such that γ is nearly pure imaginary and Z_o is nearly real. The length of a line will be called short or long depending on whether $|\gamma\ell| << 1$ or $|\gamma\ell| >> 1$.

For a short *RC* line eq (4.5) reduces to

$$V_L/V_S = \frac{R_L}{2R_L + \ell R}, \quad \omega << R/L, \quad 1/RC\ell^2. \tag{4.12}$$

where we have assumed $R_L = \sqrt{L/C}$. That is, in the short *RC* limit the transmission line can be replaced simply by a resistor of value ℓR. The complicated behaviors of γ and Z_o indicated in eq (4.10) thus combine to give the expected low-frequency result. If the $\Delta\omega$ of a pulse satisfies the conditions of eq (4.12), then the pulse is received with reduced amplitude but unchanged shape. The reduction in amplitude becomes significant if the line is long enough that ℓR is comparable to R_L. For copper at 295 K the length of line for which $\ell R = R_L$ is

$$\ell = \frac{\sigma ds}{2}\sqrt{\frac{\mu_o}{\epsilon\epsilon_o}}. \tag{4.13}$$

so that the useable length increases in proportion to s and d. For $d = 1$ μm and $\epsilon = 4$, this length varies from 0.11 cm at $s = 0.2$ μm to 11 cm at $s = 20$ μm. One concludes that at least 2 μm of dielectric are required to make striplines show sufficiently small amplitude reduction. This is the same conclusion that was drawn from the $\tau = 50$ ps pulses of figure 6 and for good reason. The frequencies below which the various normal-state striplines can be considered *RC* lines are listed in table III. Since for $\tau = 50$ ps, $\Delta\nu \equiv \Delta\omega/2\pi$ is 3×10^9 Hz, the 295 K lines with $s = 0.2$ μm and 2 μm are on the border between RC and LC lines. Moreover, we shall see that the transfer function of eq (4.12) also applies in the short *LC* range so that, with the exception of those pulses displaced from the origin, all the 50 ps pulses of figure 6 show the amplitude reduction predicted by eq (4.12).

At 4.2 K one can define a useable length for copper lines at low frequencies similar to that of eq (4.13) but with σ replaced by $\tilde{\sigma}$. This length varies from 7.4 cm at $s = 0.2$ μm to 740 cm at $s = 20$ μm, so that the low-frequency characteristics of cooled copper lines should be very good for lengths typical of microcircuits. As can be seen from table III, however, frequencies considered low are in this case considerably less than those characteristic of a $\tau = 50$ ps pulse.

For a long RC line the frequency response is limited by the RC time constant of the line. The transfer function is

TABLE III. *Frequency (Hz) at which the resistive and reactive parts of the series impedance Z are equal for striplines with $d = 1$ μm, $\epsilon = 4$, and various dielectric thicknesses.*

s (μm)	0.2	2	20	200
Cu, 295 K	6×10^9	1.5×10^9	2.1×10^8	2.1×10^7
Cu, 4.2 K	7×10^7	2.5×10^7	3.2×10^6	3.2×10^5

$$V_L/V_S = \sqrt{\omega L/R}\exp(-\ell\sqrt{R\omega C/2}) \times \exp\left[-i\left(\frac{\pi}{4} + \ell\sqrt{R\omega C/2}\right)\right]. \qquad (4.14)$$

$$1/RC\ell^2 << \omega << R/L.$$

which includes both attenuation and phase lag. Impedance mismatch causes the $\sqrt{\omega L/R}$ attenuation and the $\frac{\pi}{4}$ phase lag. The propagation constant contributes the exponential attenuation and the phase lag proportional to ℓ. The long RC limit describes the 50 ps pulse traveling the $s = 0.2$ μm, $\ell = 1$ cm line shown in figure 6.

In the LC limit, impedance mismatch is present only as a second-order effect and can be neglected. The transfer function in this limit is

$$V_L/V_S = \frac{1}{2}\exp\left(-\ell\frac{R}{2\sqrt{L/C}}\right) \times \exp\left[-i\ell\omega\sqrt{LC}\left(1 + \frac{R^2}{8\omega^2L^2}\right)\right] \qquad (4.15)$$

$$\omega >> R/L.$$

such that waves propagate with a phase velocity of very nearly $1/\sqrt{LC}$. An LC line is short provided ℓ is much less than the wavelength, $\ell << 1/\omega\sqrt{LC}$, and in this case eq (4.15) approximates eq (4.12). Thus, the short RC and LC lines both can be simply modeled with a resistor.

Of the pulses shown in figure 6, all except the 50 ps pulse on the $s = 0.2$ μm line are described by the transfer function for an LC line, eq (4.15), and the impedance mismatch can be neglected. The propagation of these pulses can be explained in terms of the attenuation and dispersion shown in figure 3. Because $\Delta\nu$ is 3×10^9 and 3×10^{11} Hz for τ equal 50 and 0.5 ps, respectively, the relevant forms for v_ϕ and α_{dB} are approximately those of region III. In this region α_{dB} is proportional to $\sqrt{\omega}$ (see eq (3.12)) so that in going from 3×10^9 to 3×10^{11} Hz the attenuation increases by a factor of 10. This is confirmed in figure 6 by the fact that the 0.5 ps pulses show the same attenuation as the 50 ps pulses after traveling only 1/10 the distance. Because α_{dB} is also proportional to $1/s$, an increase in attenuation of a 50 ps pulse on a 2 μm line is comparable to that of a 0.5 ps pulse on a 20 μm line. A similar conclusion can be drawn for the phase velocity. As eq (3.9) indicates, the deviation of v_ϕ from its high-frequency value is proportional to $1/\sqrt{\omega}s$. The phase shift over a given length of line due to this deviation is thus proportional to $\sqrt{\omega}/s$. Thus, broadening of a pulse and displacement of its peak from $t = t_\ell$ change with ω and s just as the attenuation.

The LC approximation applies to all of the pulses shown in figure 7 for copper at 4.2 K. For frequencies typical of the pulses shown the surface impedance is governed by the extreme-anomalous equations with $\delta_n < s, d$. In this limit, the attenuation and phase shift are proportional to $\omega^{2/3}/s$. Conclusions similar to those drawn for copper at 295 K can thus be made for figure 7.

An analysis of pulse propagation for superconducting niobium is shown in figure 8 for pulses with $\tau = 1$ and 0.5 ps. For a pulse with $\tau = 50$ ps there is no significant distortion even after propagating a distance of 10 cm on a line with 0.2 μm of dielectric. Pulse degradation is essentially negligible for superconducting lines until the frequencies involved begin to approach the energy-gap frequency, at which point the stripline characteristics degrade rapidly. The increase in distortion between the 1 and 0.5 ps pulses of figure 8 is thus nearly as great as that between 50 and 0.5 ps pulses on a normal-state stripline. The distortion evident in figure 8 is primarily due to dispersion at frequencies somewhat below the energy gap as discussed elsewhere in detail [13]. Comparison of figures 7 and 8 shows that a superconducting line is marginally superior to a normal-state line even for $\tau = 0.5$ ps. For longer pulses the superiority of superconducting lines is beyond question.

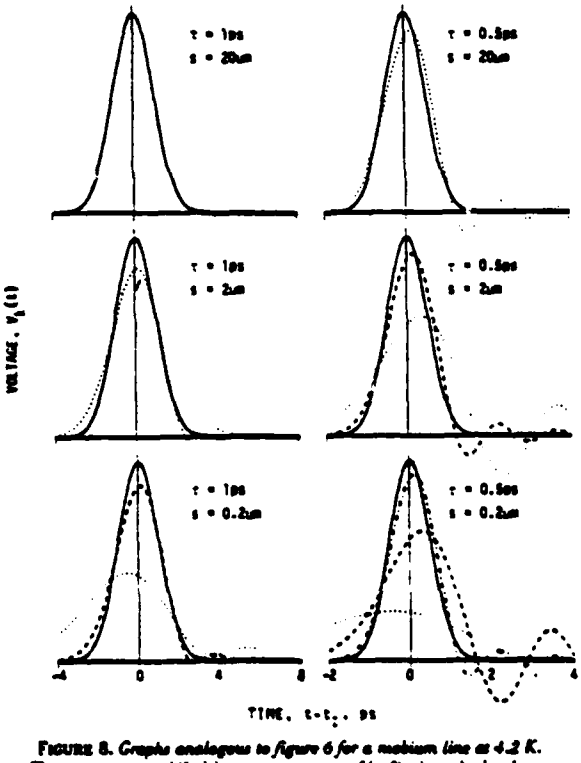

FIGURE 8. *Graphs analogous to figure 6 for a niobium line at 4.2 K.* The time origin is shifted by an amount $t_\ell = \ell/v_\phi(0)$ where the low-frequency phase velocity $v_\phi(0)$ is 1.10×10^8, 1.44×10^8, and 1.49×10^8 m/s for dielectric thickness of 0.2, 2, and 20 μm, respectively.

V. Appendix

The numerical solution of eq (2.7) and calculation of the surface impedance for general l, δ_c, and d follows a method presented by Mason and Gould [26] for the superconducting case. Applying the transformations of Mason and Gould to eq (2.7) yields

$$E_x(z) = E_x(d) + i\frac{\alpha}{l}\int_0^d dz' E_x(z') \cdot G_1((z' - d)/l, (z' - z)/l) \tag{A.1}$$

$$G_1(u, v) = \int_u^v dr \int_1^\infty ds\,(v - r)\left(\frac{1}{s} - \frac{1}{s^3}\right) e^{-|r|s}.$$

where the kernal G_1 can be evaluated in terms of E_1, the exponential integral [27]. Over the domain of interest ($u \leq 0$, $v \geq u$),

$$\begin{aligned} G_1(u, v) = {} & \frac{1}{24}\left[(u^3 + u^2 - 10u - 6)e^u \right. \\ & \left. + (u^4 - 12u^2)E_1(|u|)\right] \\ & + \frac{1}{24}\left[(|v^3| - v^2 - 10|v| + 6)e^{-|v|} \right. \\ & \left. + (v^4 - 12v^2)E_1(|v|)\right] \\ & + \frac{1}{6}(v - u)\left[(u^2 + u - 4)e^u \right. \\ & \left. + (u^3 - 6u)E_1(|u|)\right] \\ & + \frac{2}{3}(|v| + v) \end{aligned} \tag{A.2}$$

A numerical solution of the above integral equation results when the integral is approximated by a sum consisting of N terms in which the integrand is evaluated at the points $z' = z_1, z_2, \cdots, z_N$. By choosing z to be each of these z_i in succession, one obtains a set of N linear equations which can be solved for the unknowns $E_x(z_i)$. In this procedure $E_x(d)$ may be taken as any non-zero constant as it merely sets the scale.

Once $E_x(z)$ is known, the integral over current density required for the surface impedance can be obtained from

$$\int_0^d dz\, J_x(z) = \frac{3}{4}\sigma \int_0^d dz\, E_x(z) G_2((z - d)/l, z/l) \tag{A.3}$$

$$G_2(u, v) = \int_u^v dr \int_1^\infty ds\left(\frac{1}{s} - \frac{1}{s^3}\right) e^{-|r|s},$$

where for the domain of interest ($u \leq 0$, $v \geq 0$),

$$G_2(u, v) = \frac{4}{3} + \frac{1}{6}\left[(u^2 + u - 4)e^u + (u^3 - 6u)E_1(|u|)\right] + \frac{1}{6}\left[v^2 - v - 4)e^{-v} - (v^3 - 6v)E_1(v)\right]. \tag{A.4}$$

The above procedure gives accurate results using a small number of integration points except when the depth of field penetration is small compared to d. In this limit, however, d can be taken as infinity and the Reuter-Sondheimer result, eq (2.8), adopted in place of the integral equation.

VI. References

[1] Van Tuyl, R. L., Liechti, C. A., Lee, R. E., and Gowen, E. GaAs MESFET Logic with 4-GHz Clock Rate. IEEE J. Solid-State Circuits, Vol. **SC-12**, pp. 485–496, (Oct. 1977).

[2] Herrell, D. J. Femtojoule Josephson Tunneling Logic Gates. IEEE J. Solid-State Circuits, vol. **SC-9**, pp. 277–282, (Oct. 1974).

[3] Keyes, R. W. Physical Limits in Digital Electronics, Proc. IEEE, vol. **63**, pp. 740–767, (May 1975).

[4] Keyes, R. W., Harris, E. P., Konnerth, K. L. The Role of Low Temperatures in the Operation of Logic Circuitry, Proc. IEEE, vol. **58**, pp. 1914–1932, (Dec. 1970).

[5] Hasan, M. M. and Mullick, S. K. Monolithic MIC's, in *Microwave Integrated Circuits*, K. C. Gupta and A. Singh, Eds. (New York: Wiley, 1974).

[6] Lahiri, S. K. and Basavaiah, S. Lead-Alloy Josephson-Tunneling Gates with Improved Stability upon Thermal Cycling, J. Appl. Phys., vol. **49**, pp. 2880–2884, (May 1978).

[7] Bryant, T. G. and Weiss, J. A. Parameters of Microstrip Transmission Lines and Coupled Pairs of Microstrip Lines, IEEE Trans. Microwave Theory Tech., vol. **MTT-16**, pp. 1021–1027, (Dec. 1968).

[8] Herrell, D. J., Arnett, P. C. and Klein, M. High Performance Josephson Interferometer Latching Logic and Power Supplies, in *Future Trends in Superconductive Electronics*, B. S. Deaver et al. Eds. (New York: American Institute of Physics, 1978), pp. 470–478.

[9] Denlinger, E. J. A Frequency Dependent Solution for Microstrip Transmission Lines, IEEE Trans. on Microwave Theory Tech., vol. **MTT-19**, pp. 30–39, (Jan. 1971).

[10] Corr, D. G. and Davies, J. B. Computer Analysis of the Fundamental and Higher Order Modes in Single and Coupled Microstrip, IEEE Trans. on Microwave Theory Tech., vol. **MTT-20**, pp. 669–678, (Oct. 1972).

[11] Matick, R. E. *Transmission Lines for Digital and Communication Networks*, (New York: McGraw-Hill, 1969), Chapters 4 and 6.

[12] Mattis, D. C. and Bardeen, J. Theory of the Anomalous Skin Effect in Normal and Superconducting Metals, Phys. Rev., vol. **111**, pp. 412–417, (July 1958).

[13] Kautz, R. L. Picosecond Pulses on Superconducting Striplines, J. Appl. Phys., vol. **49**, pp. 308–314, (Jan 1978).

[14] Tinkham, M. *Introduction to Superconductivity*, (New York: McGraw-Hill, 1975), Chapters 2 and 3.

[15] Pippard, A. B. Metallic Conduction at High Frequencies and Low Temperatures, in *Advances in Electronics and Electron Physics*, vol. VI, L. Marton, Ed. (New York: Academic Press, 1954), pp. 1–45.

[16] Reuter, G. E. H. and Sondheimer, E. H. The Theory of the Anomalous Skin Effect in Metals, Proc. Roy. Soc., (London), vol. **A195**, pp. 336–364, (Dec. 1948).

[17] *American Institute of Physics Handbook*, D. E. Gray, Ed. (New York: McGraw-Hill, 1972), p. 9–39.

[18] Rosenblum, S. S., Steyert, W. A., and Fickett, F. R. A Simple Method for Producing High Conductivity Copper for Low Temperature Applications. Cryogenics, vol. 17, pp. 645–647, (Nov. 1977).

[19] Henkels, W. H. and Kircher, C. J. Penetration Depth Measurements on Type II Superconducting Films. IEEE Transactions on Magnetics, vol. MAG-13, pp. 63–66, (Jan. 1977).

[20] Sondheimer, E. H. The Mean Free Path of Electrons in Metals. Advances in Phys., vol. 1, pp. 1–42, (Jan 1952).

[21] Ramo, S., Whinnery, J. R., and Van Duzer, T. *Fields and Waves in Communication Electronics*. (New York: Wiley, 1965), p. 334.

[22] van der Pauw, L. J. The Radiation of Electromagnetic Power by Microstrip Configurations. IEEE Trans. Microwave Theory Tech., vol. MTT-25, pp. 719–725, (Sept. 1977).

[23] Davidheiser, R. A. Superconducting Microstrip Filters, in *Future Trends in Superconductive Electronics*, B. S. Deaver et al. Eds., (New York: American Institute of Physics, 1978), pp. 219–222.

[24] Lewin, L. Radiation from Discontinuities in Strip-Lines. Proc. IEE, vol 107C, pp. 163–170, Feb. 1960.

[25] McDonald, D. G., Peterson, R. L. and Bender, B. K. Design of a Josephson-Junction Picosecond Pulser. J. Appl. Phys., vol. 48, pp 5366–5369, (Dec. 1977).

[26] Mason, P. V. and Gould, R. W. Slow-Wave Structures Utilizing Superconducting Thin-Film Transmission Lines. J. Appl. Phys., vol. 40, pp. 2049–2051, (April 1969).

[27] *Handbook of Mathematical Functions*, M. Abramowitz and I. A. Segun, Eds. (New York: Dover, 1965), p. 228.

APPENDIX F

A superconducting sampler for Josephson logic circuits

C. A. Hamilton, F. L. Lloyd, R. L. Peterson, and J. R. Andrews
Electromagnetic Technology Division, National Bureau of Standards, Boulder, Colorado 80303

(Received 9 July 1979; accepted for publication 20 August 1979)

A method is described for automating a technique which is used to sample transition duration (rise time) in superconducting logic circuits. The method is based on measuring the time at which a biased Josephson junction switches under the influence of an applied signal. The system transition duration is limited primarily by time jitter which is estimated to be 7 ps. Transition durations of as little as 9 ps have been observed.

PACS numbers: 74.50. + r

The characterization of Josephson logic circuits often requires the measurement of very fast low-level signals. Such measurements are difficult to perform because of the loss of bandwidth for signal transmission to room temperature. Also, standard sampling oscilloscopes have transition durations (rise time) of about 20 ps whereas high current density Josephson devices switch in times less than 10 ps. It is therefore desirable to provide for high-speed measurements directly on the superconducting logic chip. This may be accomplished by using a biased Josephson detector as an amplitude discriminator for the signal to be measured.[1,2] This detector will switch to the voltage state when the signal plus the bias exceed the detector critical current. Since the bias and the critical current are known, the signal level at the time the detector switches can be determined. Thus, by measuring the delay in the detector output as a function of bias, rising edges on the signal may be mapped out. This has commonly been done[1,2] by recording traces of the detector output for a number of values of bias. The signal may then be computed point by point. This method is somewhat tedious and may yield erroneous results if the time base used drifts during the measurements. Since time-base drift may be as much as several ps/min, it is a serious problem for ultrafast measurements.

Typical sampling oscilloscopes used to record the detector waveform have an external time-base input which may be used to specify the sampling time. By driving this input from the sampled voltage, the sampling time can be locked to the steepest portion of the detector output waveform. The time-base input, therefore, is a measure of the detector switching time. The signal waveform is thus reproduced by sweeping the bias and recording the bias versus the time-base input. This method yields the signal waveform directly and in a time short enough to minimize drift problems.

Figure 1 shows in more detail how this is accomplished. The superconducting integrated circuit is shown in the dashed box. It consists of a first junction $J1$ which serves to produce a very fast signal transition which is then sampled by the second detector junction $J2$. The sequence is as follows: a tunnel diode step generator operating at 60 kHz applies a repetitive 200-ps transition duration step to junction $J1$. When its critical current I_{c1} is exceeded, $J1$ switches to its energy gap (2.5 mV) in a time determined primarily by its critical current and capacitance. This applies a signal current I_s through the 8-Ω resistor to junction $J2$. $J2$ will switch when the current I_s plus the bias current I_b exceeds I_{c2}. The output of $J2$ is transmitted to room temperature and sampled at time t. The sampled voltage is compared with a reference level, typically 1 mV, by applying the reference as an offset voltage to the sampling head amplifier. The difference signal from the sampling head amplifier is integrated by inverting amplifier A1 and used to drive the sampling time base input. Thus, if the sampled voltage is below the reference level, the integrator output increases, advancing the sampling time to the point where the signal equals the reference. If the sampled voltage is greater than the reference, the sampling time is decreased in the same way. This servo loop thus causes the sampling time to lock to the point at which the rising edge of the $J2$ transition crosses the reference level. The time base input is therefore a measure of the time at which $J2$ switches, i.e., the time at which I_s equals $I_{c2} - I_b$. As I_b is slowly swept by the ramp generator (~ 30-s sweep time), the X-Y recorder, which plots $-I_b$ versus sampling time, will trace out the rising portion of the transition in I_s. Since the sampling rate (60 kHz) is much greater than the servo loop frequency response, noise and time jitter in the sampling system are averaged. The 600-ps delay line on the IC chip provides isolation to separate the $J2$ transition from cross talk between input and output lines at the chip mount. The timing network and analog switch pull the bias to zero between samples to reset the junctions to the zero voltage state.

The advantage of this method lies in the fact that it can measure transition durations which are substantially faster than the transition duration of either the chip mount (~ 50 ps) or the sampling scope (~ 20 ps). The measurable transi-

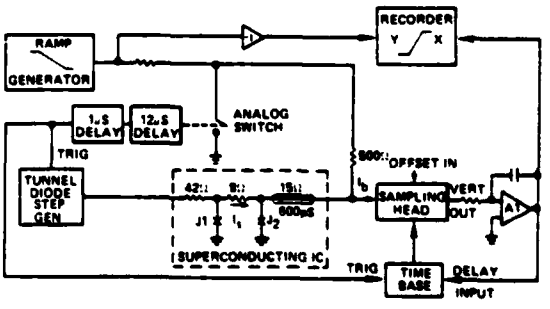

FIG. 1. Block diagram of the transition duration measurement system utilizing a Josephson junction as an amplitude discriminator.

 0003-6951/79/210718-02$00.50

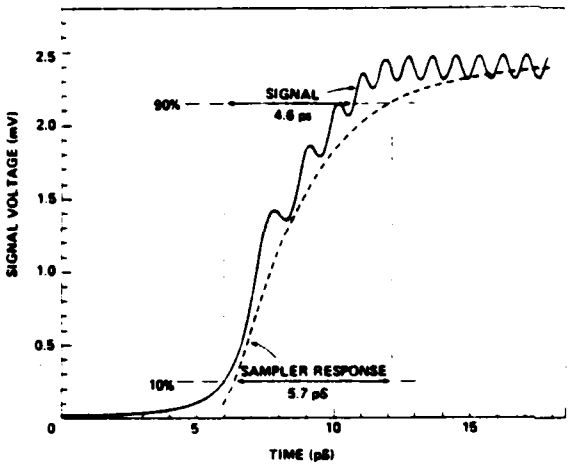

FIG. 2. Simulation of the signal voltage waveform (solid curve) and its reconstruction (dashed curve) based on the use of a second junction as a sampling device. The time scale of the reconstructed curve has been arbitrarily shifted to bring the two curves together. The simulation parameters are $I_{c1} = 2.9$ mA, $C_1 = 4.8$ pF, $I_{c2} = 1.45$ mA, $C_2 = 2.4$ pF. The input is a 1-mV/ps ramp.

tion duration is limited primarily by the jitter in the sampling system. The accuracy of the recorded waveform is also subject to the assumption that the detector junction waveform is constant and that its delay depends only on the instant at which its critical current is exceeded. These assumptions will break down at sufficiently high speeds. The most significant error results from the fact that the turn-on delay[3] of $J2$ is a function of overdrive. Thus for low bias values (signal near maximum), the $J2$ transition has some additional delay. This has the effect of making the recorded waveform slightly slower than the actual signal.

Figure 2 is the result of a simulation of our circuit. The solid curve is the computed signal voltage produced by $J1$. The dashed curve is the computed result which the above described method would produce in the absence of jitter. The error caused by variable turn-on delay is evident in the increased separation of the two curves near the signal maximum. The fine structure caused by Josephson oscillations is also washed out. The critical current density of both junctions is 4200 A/cm^2, giving them an estimated $R_N C$ time of

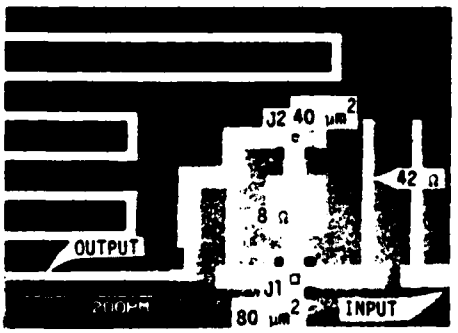

FIG. 3. Photograph of the superconducting integrated circuit.

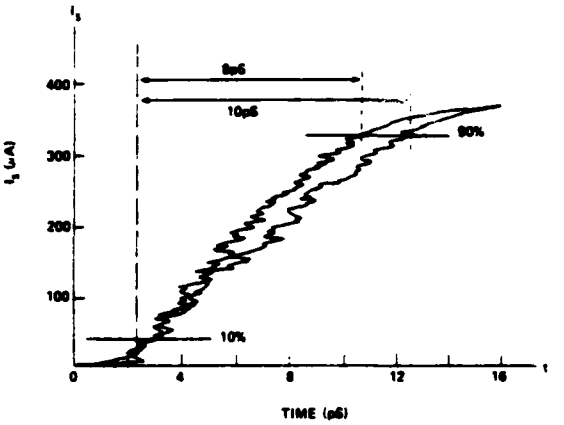

FIG. 4. Recorded transition duration of the signal current I_s for a junction with critical current density of 4200 A/cm^2.

2 ps (R_N is the junction normal state resistance).[4] The effect of jitter is roughly equivalent to passing the signal through a low-pass filter of rise time equal to the jitter width.

Figure 3 is a photograph of the integrated circuit used in this experiment. It is a seven-level circuit which uses a lead alloy process similar to that described in Ref. 5. The junction areas are approximately 40 and 80 μm^2 as indicated. The microstripline showing at the left is a small portion of the line used to obtain 600 ps of delay in the output signal. The parameters used in the simulation of Fig. 2 are taken from measurements on this circuit.

Figure 4 is the experimental transition duration data recorded for this circuit. The two traces, recorded about one minute apart, are for increasing and decreasing bias. They are different because the sampling time drift decreases the apparent transition duration in one case and increases it in the other. Assuming constant drift, the correct transition duration (10%–90%) will be the average, or about 9 ps. This result represents the combination of the signal transition duration estimated to be about 5 ps and the jitter limited system response of about 7 ps.

A second experiment was performed in which the switching transition of $J1$ was intentionally rolled off by an on-chip RC filter. In this case the recorded waveform was the expected exponential rise. The time constant (3.7 ns) matched the filter to the accuracy with which the filter components were known (30%).

It is important to note that the very fast switching speed reported here is only one part of the delay which occurs in logic circuits. Gheewala[6] has used a chain of gates to measure logic delays of as little as 13 ps.

This work is supported by the Office of Naval Research under Contract No. N00014-79-F-0020.

[1]Hans H. Zappe, IEEE J. Solid State Circuits, SC-10, 12–19 (1975).
[2]D.J. Herrell, IEEE Trans-Magn. MAG-10, 864–867 (1974).
[3]E.P. Harris, IEEE Trans-Magn. MAG-15, 562 (1979).
[4]This RC time is accurate to about a factor of 2 and was taken from R.E. Harris and C.A. Hamilton, AIP Conf. Proc. 44, 448–458 (1978).
[5]J. Greiner, S. Basavaiah, and I. Ames, J. Vac. Sci. Technol. 11, 81–84 (1974).
[6]T.R. Gheewala, Appl. Phys. Lett. 34, 670 (1979).

APPENDIX G

Quasiparticle heterodyne mixing in SIS tunnel junctions

P. L. Richards and T. M. Shen

Department of Physics, University of California, Berkeley, California 94720

R. E. Harris and F. L. Lloyd

National Bureau of Standards, Boulder, Colorado 80303

(Received 5 October 1978; accepted for publication 20 December 1978)

The rapid onset of quasiparitcle tunneling current in superconductor-insulator-superconductor (Josephson) junctions at voltages above $2\Delta/e$ is being used for millimeter-wave heterodyne mixing. Junctions with a 2-μm diameter and $R_N = 50\ \Omega$ have little capacitive shunting at the signal frequency of 36 GHz. Because there is no series resistance, residual capacitance can be tuned out. Double sideband conversion efficiencies of 0.32 and mixer noise temperatures as low as $T_M \leq 7$ K $= 4h\nu/k$ have been observed. The results are compared with shot-noise-limited mixer theory. Photon-assisted tunneling effects are seen which indicate the approach to photon-noise-limited operation.

PACS numbers: 07.62. + s, 74.50. + r

The ideal nonlinear element for a classical heterodyne mixer is a switch which can be driven between high- and low-resistance states by the local oscillator (LO). At microwave frequencies, Schottky diodes with I-V characteristics of the form $I = I_0[\exp(SV) - 1]$ are often used for this purpose. Conventional Schottky diodes have $S = e/kT = 40\ \text{V}^{-1}$ at 300 K and somewhat higher values at reduced temperatures. The nonlinearity in such diodes arises from thermally activated conduction and disappears at temperatures low enough that tunneling currents dominate. The super-Schottky diode[1] which operates by quasiparticle tunneling between a superconductor and a semiconductor has $S = 11\,600\ \text{V}^{-1}$ at $T = 1$ K. Such a sharp corner on the I-V curve is advantageous for small signal recievers at short millimeter and submillimeter wavelengths because of the difficulty in obtaining large amounts of LO power at high frequencies and because LO noise problems are reduced. Low-temperature operation also gives low mixer noise. The maximum operating frequency of these Schottky devices is set by the requirement that the junction capacitance discharges through the series (spreading) resistance of the semiconductor twice each cycle.

In principle, a superconductor-insulator-superconductor (SIS) tunnel junction approaches the ideal switch limit more closely than the super-Schottky or related devices because the singularities in the density of states on both sides of the junction cause an extremely sharp onset of qusiparticle current at the full gap voltage $2\Delta/e$. In practice, the S values thus far obtained from Pb-In-Au alloy junctions in the 1.5–4.2 K temperature range are comparable to an ideal Schottky at ~ 1.3 K. An important feature of this device is the absence of series (spreading) resistance. External microwave circuit elements can thus be used to resonate out the junction capacitance. Since there are always practical limitations to the amount of capacitance which can be resonated, it is useful to inquire to what extent capacitance can be made unimportant by adjusting junction parameters. As the junction oxide thickness is reduced, R_N decreases exponentially while C increases linearly. Consequently, the importance of junction capacitance remains nearly constant if the normal state conductance per unit area, or, equivalently, the critical Josephson current density J_c, is scaled in proportion to frequency. We have $\omega C R_N \simeq 1$ at 36 GHz for junctions with critical current density $J_c = 10^3\ \text{A/cm}^2$. In order to maintain

 0003-6951/79/050345-03$00.50

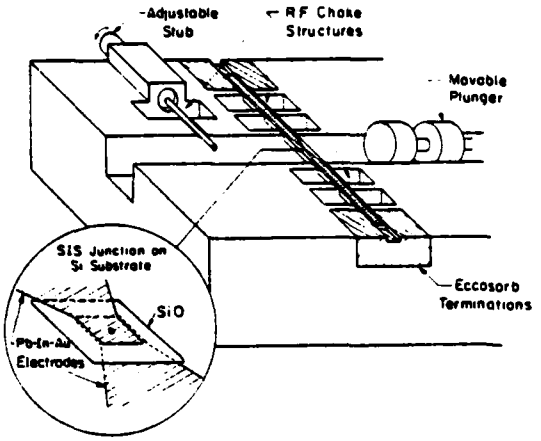

FIG. 1. Diagram showing the junction configuration and the arrangement of the junction in the 36-GHz mixer block.

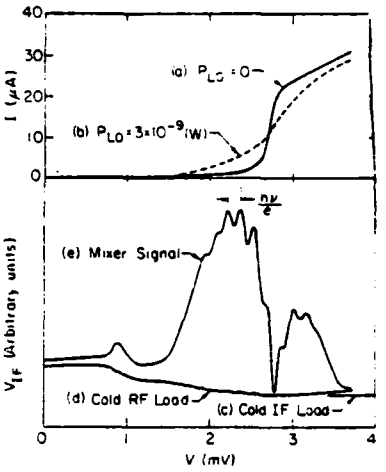

FIG. 2. Static I-V curves are shown above for a 1.5 K junction (a) without and (b) with P_{LO}. Plots of IF amplifier output voltage in the frequency range from 30 to 80 MHz are shown as a function of junction bias voltage. Curve (c) was obtained with a 50-Ω 1.5 K load in place of the mixer; curve (d) with a matched 1.5 K load in front of the mixer; curve (e) with a calibrated 36-GHz signal applied to the mixer from a Klystron oscillator. Values of mixer noise temperature were deduced from (c) and (d), and conversion efficiency from (e).

suitable impedances for input and output coupling, the junction area must be scaled inversely with frequency. The need for very small junctions at high frequencies could be avoided by using several junctions in series. This would also increase the saturation level of the device. Since SIS junctions are being actively developed for other applications, a wide variety of junction parameters have been obtained. Junctions have been reported with high enough current density[2,3] to give good performance up to 900 GHz, beyond which mixing action will be degraded by the breaking of superconducting pairs.

The Pb-In-Au alloy junctions used in these experiments were fabricated at NBS, Boulder, using the photoresist liftoff and rf sputter-oxidation techniques.[4] The junction geometry is shown in Fig. 1. The first electrode was evaporated to a thickness of 4100 Å on a Si substrate and subsequently covered with a 4500-Å-thick square of SiO. The SiO was then removed in the area of the desired junction and the junction oxide was grown by differential sputtering and oxidation. Finally, a 5000-Å-thick counterelectrode was added. A $0.28\times1.0\times19$-mm strip containing a single junction and its leads was separated by cleaving from the 40 junctions produced on each 5-cm-diam. Si wafer. The junction areas were varied from $\sim2\times2$ to $\sim4\times4$ μm to provide a range of impedances.

The junction assembly was placed across a full-height KA-band microwave waveguide in the E-field direction as shown in Fig. 1. The outer dimensions of the channel in which the substrate was placed were varied periodically to provide an rf choke. An adjustable stub $3\lambda/4$ in front of the junction and a plunger behind it completed the low-temperature microwave circuit. Signal and LO power from carefully calibrated 36-GHz Klystrons were combined in a 10-dB directional coupler and introduced into the cryostat through a section of stainless-steel waveguide. Three identical 50-Ω stainless-steel intermediate-frequency (IF) cables were installed in the cryostat. One was terminated with a short circuit to measure IF cable losses, one was terminated in a 50-Ω cold load to provide a noise source for calibrating the IF amplifier train, and one was connected to the mixer. A directional coupler was used to inject a signal into the mixer output to evaluate its coupling to the IF system. Measurements in the IF frequency band of 30–80 MHz were made using a string of transistor amplifiers with $T_{IF} = 50$ K followed by a spectrum analyzer.

The I-V curve of an SIS junction at 1.5 K is shown at the top of Fig. 2 with $P_{LO} = 0$ and also with P_{LO} adjusted for optimum conversion efficiency. The knee of the I-V curve corresponds to $S = 9800$ V^{-1}, compared with 7730 for an ideal super-Schottky at the same temperature. The conversion efficiency and the noise in an SIS mixer are plotted on

TABLE I. Properties of two SIS mixers operated at 1.5 K. The noise temperatures and conversion efficiencies are referred to a single sideband. The experimental errors are given as 50% confidence limits.

J_c (A/cm^2)	R_n (Ω)	ωCR_n	T_M (Exp.) (K)	T_M (Theory) (K)	L_c^{-1} (Exp.)	L_c^{-1} (Theory)	P_{LO} ($\times10^{-6}$) (W)
390	100	2	$\lesssim14$	3.1	0.16 ± 0.02	0.16	3
710	52	1.4	25 ± 9	6.1	0.15 ± 0.02	0.18	5

the same voltage scale at the bottom of Fig. 2. For $0 < V < 1.3$ mV, the response is dominated by hysteretic Josephson mixing which is very noisy.[3] In junctions with larger values of zero voltage current, this response (and noise) was as much as one order of magnitude larger than shown, but could be suppressed with a magnetic field.

Above 1.3 mV mixing occurs because of the two regions of curvature on the quasiparticle I-V curve. The noise in this voltage range is small and is independent of magnetic field. A periodic modulation of the quasiparticle mixing appears due to photon-assisted tunneling because the range of voltage occupied by the knee of the static I-V curve is comparable to $h\nu/e$. This is the quantum correction to mixing calculated by Tucker and Millea.[6] The properties of two SIS mixers are shown in Table I.[7] The mixer performance has been calculated from the static I-V curve in each case using classical mixer theory and assuming that the capacitance has been resonated out at the signal frequency, but that the capacitance short circuits all harmonics.[8] This is a reasonable representation of our experiments because $\omega C R_N \gtrsim 1$. The calculated values of conversion efficiency are in good agreement with the measurements. The calculated values of T_M, assuming only shot noise, are somewhat less than the measured values.

The present performance of the SIS mixer is sufficiently good to make practical applications very attractive. The stability and resistance to thermal cycling of the Pb-In-Au alloy junctions is a substantial advantage over the point-contact Josephson mixer which had higher noise ($T_M = 54$ K) and higher conversion efficiency $= 1.3$ at the same frequency.[9] The apparent ease with which operation can be extended to higher frequencies appears to be an advantage over the GaAs super-Schottky diode. The full benefit of this mixer will not be obtained unless an IF amplifier with $T_{IF} \sim 1$ K can be developed.

This work was supported in part by the U.S. Office of Naval Research.

[1]F.L. Vernon, Jr., M.F. Millea, M.F. Bottjer, A.H. Silver, R.J. Pedersen, and M. McColl, IEEE Trans. Magn. MAG-13, 221 (1977).
[2]R.F. Broom, W. Jutzi, and Th.O. Mohr, IEEE Trans. Magn. MAG-11, 755 (1975).
[3]J. Niemeyer and V. Kose, Appl. Phys. Lett. 29, 380 (1976).
[4]A. Description of the fabrication techniques and original references can be found in R.H. Havemann, C.A. Hamilton, and R.E. Harris, J. Vac. Sci. Technol. 15, 392 (1978).
[5]Y. Taur, J.H. Claassen, and P.L. Richards, Appl. Phys. Lett. 24, 101 (1974).
[6]J.R. Tucker (unpublished).
[7]The general concept of this mixer and a preliminary measurement of conversion efficiency were mentioned briefly in a previous publication, P.L. Richards, *Future Trends in Superconductive Electronics*, edited by B.S. Deaver, Jr., C.M. Falco, J.H. Harris, and S.A. Wolf (American Institue of Physics, New York, 1978), p. 223. The most important new result reported here is the demonstration that Josephson effects do not degrade T_M. The measured noise is comparable to that expected from shot noise in the quasiparticle current alone.
[8]D.H. Held and A.R. Kerr, IEEE Trans. Microwave Theory Tech. MTT-26, 49 (1978).
[9]J.H. Claassen, Y. Taur, and P.L. Richards, Appl. Phys. Lett. 25, 759 (1974).

DISTRIBUTION LIST

FOR

TECHNICAL REPORTS

CONTRACT NUMBER N00014-79-F-0005

	ADDRESSEE	NUMBER OF COPIES
1.	Office of Naval Research, Code 427 800 North Quincy Street Arlington, Virginia 22217	4
2.	Office of Naval Research Branch Office 1030 East Green Street Pasadena, California 91106	1
3.	The Aerospace Corporation Post Office Box 92957 Los Angeles, California 90009 Attn: A. Silver	1
4.	IBM Corporation 18100 Frederick Pike Gaithersburg, Maryland 20760 Attn: R. Troutman	1
5.	TRW Defense Space Systems Group One Space Park Redondo Beach, California 90278 Attn: D. Claxton	1
6.	University of California Electronics Research Laboratory Berkeley, California 94720 Attn: T. Van Duzer	1
7.	Naval Research Laboratory, Code 2026 4555 Overlook Avenue, S. W. Washington, D. C. 20375	1
8.	Naval Research Laboratory, Code 6854 4555 Overlook Avenue, S. W. Washington, D. C. 20375	1
9.	Data Acquisition Research Tektronix P. O. Box 500 Beaverton, Oregon 97077 Attn: Jon Birck	1

10. University of California — 1
Lawrence Livermore Laboratory
Livermore, California 94550
Attn: Joe Balch

11. Hewlett-Packard — 1
1501 Page Mill Road
Palo Alto, California 94304
Attn: Tom Hornak

12. Texas Instruments, Inc. — 1
P. O. Box 5936
Dallas, Texas 75222
Attn: William Wiseman

13. National Bureau of Standards — 4
Boulder, Colorado 80303
Attn: D. Sullivan

14. Defense Documentation Center — 12
Cameron Station Bldg. 5
Alexandria, Virginia 22314

15. A. G. E. D. — 1
9th Floor
201 Varick Street
New York, New York 10014


DATE
FILME
-8